Bioinspired Agile Robotic Jumping and Balancing

Jingcheng Sun

Submitted in accordance with the requirements for the degree of

Doctor of Philosophy

The University of Leeds

School of Mechanical Engineering

August 2025

Intellectual Property and Publication Statements

I confirm that the work submitted is my own, except where work which has formed part of jointly authored publications has been included. My contribution and the other authors to this work has been explicitly indicated below. I confirm that appropriate credit has been given within the thesis where reference has been made to the work of others.

Chapters based on jointly authored publications

- **Chapter 3** is based on: Sun, Jingcheng, and Chengxu Zhou. "AeroTail: a bio-inspired aerodynamic tail mechanism for robotic balancing." In *2023 28th International Conference on Automation and Computing (ICAC)*, pp. 1–6. IEEE, 2023.
- **Chapter 4** is based on: Sun, Jingcheng, and Chengxu Zhou. "Optimising aerodynamic drag for enhanced robotic balancing." *Engineering Applications of Computational Fluid Mechanics* 18, no. 1 (2024): 2430659.
- **Chapter 5** is based on: Sun, Jingcheng, and Chengxu Zhou. "Advancing Robotic Jumping with CVT Enhanced SEA." In *Annual Conference Towards Autonomous Robotic Systems*, pp. 73–84. Cham: Springer Nature Switzerland, 2024.

Work attributable to me

- Concept development, modelling and derivation, controller design, simulation studies, optimisation, data analysis, figure preparation, manuscript drafting.

Contributions of other authors

- Supervision, methodological guidance, critical review, editorial feedback.

Abstract

Agile locomotion in legged robots requires the coordinated generation, storage, and regulation of energy under highly nonlinear and hybrid dynamics. Inspired by biological systems that exploit compliant structures and aerodynamic appendages, this thesis presents the design, modelling, and control of a bioinspired monopedal robotic platform capable of agile jumping and balancing through the integration of two key mechanical innovations: a Continuously Variable Transmission–enhanced Series Elastic Actuator (C-SEA) for vertical propulsion, and an AeroTail drag-based balancing mechanism for attitude regulation in flight.

The C-SEA leg incorporates a non-circular gear-based continuously variable transmission within a series elastic architecture to modulate effective mechanical advantage throughout the jump cycle. This enables improved energy transfer, controllable stiffness characteristics, and enhanced jumping performance compared to conventional SEA configurations. The AeroTail introduces a bioinspired drag-inducing appendage that generates aerodynamic torque proportional to rotational velocity, providing passive and actively regulated stabilisation during flight without reliance on high-inertia reaction wheels.

A unified dynamic model of the hybrid flight–stance system is developed, capturing the coupling between aerodynamic torques, compliant leg actuation, and underactuated body dynamics. Control strategies are formulated to regulate attitude and forward velocity through coordinated stance impulse shaping and flight-phase drag modulation. Stability is analysed using both linearised subspace representations and jump-to-jump variability metrics.

Simulation studies demonstrate sustained forward hopping with stable attitude regulation and highlight the importance of coupling between drag magnitude and feedback gain selection. A Monte Carlo sensitivity analysis further reveals that the closed-loop system exhibits a finite yet substantial region of attraction under bounded parameter uncertainty, consistent with the behaviour of nonlinear hybrid systems.

The results establish that combining compliant energy storage with aerodynamic drag-based balancing provides an effective embodied intelligence strategy for agile robotic locomotion. The proposed framework offers a pathway toward energy-efficient, mechanically adaptive jumping robots and contributes to the broader understanding of bioinspired actuation and hybrid dynamic stability.

Contents

List of Figures

List of Tables

Notation and Acronyms

This section summarises the acronyms and mathematical symbols used throughout the thesis. Unless otherwise stated, symbols are defined locally when first introduced; this glossary serves as a global reference to avoid ambiguity.

Acronyms

Acronym	**Meaning**
SEA	Series Elastic Actuator
C-SEA	CVT-enhanced Series Elastic Actuator
CVT	Continuously Variable Transmission
DI	Drag Inducer
RW	Reaction Wheel
SLIP	Spring-Loaded Inverted Pendulum
IP	Inverted Pendulum
CFD	Computational Fluid Dynamics
LQR	Linear Quadratic Regulator
MPC	Model Predictive Control
GUI	Graphical User Interface

Symbols

Symbol	Description	Chapter(s)
θ	Vector of generalised coordinates	3
θ_1	Leg/body angle in inverted pendulum model	3
θ_2	Tail angle relative to leg in inverted pendulum model	3
ϕ	Body pitch angle in integrated jumping robot model	6
l_1	Half-length of the leg in inverted pendulum model	3
l_2	Half-length of the tail in inverted pendulum model	3
l_D	Effective lever arm of aerodynamic drag force	3, 4
m_1	Mass of the leg (IP model)	3
m_2	Mass of the tail (IP model)	3
m_3	Mass of the body (IP model)	3
m_r	Total mass of the robot	5, 6
M	Mass of the robot body in C-SEA model	5
M_2	Moving mass of the actuator in C-SEA model	5
k	Spring stiffness of the elastic element	5
K	Controller gains	3
G_r	Transmission ratio of CVT	5
G_0	Intercept constant in CVT model	5
R	Gradient constant in CVT model	5
C_d	Aerodynamic drag coefficient	3, 4, 6
ρ	Air density	3, 4
A	Effective frontal area of drag-inducing component	3, 4
v	Local flow velocity relative to drag-inducing component	3, 4
τ	Torque (generic)	3–6
F	Force (generic)	4–6
E	Energy per jump cycle	5, 6
h	Jump apex height	5, 6
σ	Standard deviation of horizontal velocity	6

Chapter 1

Introduction

1.1 Background and motivation

The recent decades saw an increasing trend of robot designs taking ideas from natural organisms in the form of bioinspiration and biomimetics. This is due to the fact that the morphological versatility of living creatures indeed provide us with many examples of and insights into effective and efficient locomotion methods. Take jumping as an example, invertebrates such as locusts, fleas, crickets and leafhoppers use the catapult mechanism that has a lock-and-release system while jumping [1]. Among the vertebrates, mountain goats jump with rapid pulling of forelegs and extension of hindlegs and spines, in which, they are able to store energy in tendons [2]. The presence of elastic elements in musculoskeletal systems is the inspiration behind the series- and parallel- elastic actuators which have been utilised extensively in robotics. At the same time, linkage systems can be found in the knee joints of mammals, which alter the mechanical advantage at squad-down position for better leverage [3]. Many animals also possess the ability to manipulate aerodynamics. This usually takes the form of aerial abilities like flying and gliding, whereas some animals can also utilise the aerodynamic properties of their bodies without having full aerial capabilites. For example, Cheetahs' tails can generate more torque from aerodynamic drag than its inertia during turning [4]. It is also common for animals to be able to use several different locomotion methods and they can switch back and forth from one to another. There are even aquatic animals that constantly use jumping as their locomotion methods including Hydrophorus [5] and archerfish [6]. Therefore, bioinspiration and biomimetics can greatly aid the advancement of robot locomotion and especially in terms of providing insights into actuation by power modulation and aerodynamic utilisation.

All aforementioned aspects of animal behaviour have been, in one way or another, incorporated into robotic locomotion thus giving inspirations to many past robot de-

signs. Jumping and hopping robots in the past were usually designed to locomote through even terrain with little to none obstacles (examples in paper [7] and [8]). This trend gradually shifted to finding mechanisms and methods that can enable the robot to jump higher (examples: TAUB [9], MultiMo-Bat [10] [11], JumpRoACH [12], Frogbot [13], Glumper [14]), and faster (examples: Jerboa [15], MIT Cheetah [16], StarlETH [17], Minitaur [18]). A new concept call jumping agility was introduced in the paper [19]. This value is the product of the jumping height and frequency and it describes the robot's jumping ability comparing to the ballistic limit which is best jumping performance that a robot can achieve in natural earthly environment. This metric is relevant because some of the natural organisms (examples: Galago senegalensis [20], Jumping Mouse [21], Bullfrog [22], Tree frog [23]) gets incredibly close to the ballistic limit even though being outclassed by the robot in terms of height or frequency alone. Few of the bionic robots managed to approach the ballistic limits when jumping compared to many natural organisms from whom they took inspirations. Usually, a single robot design is only able to succeed in either height or frequency, thus only one of the two metrics. Therefore, it is scientifically meaningful to design bionic robots whose jumping agility can catch up with their organic counterparts in terms of approaching the ballistic limit. Furthermore, there are robots that combine jumping and gliding abilities onto a single device [24] [25]. They inevitably also took inspiration from animals like insects, birds and even mammals that possess both jumping ability and gliding. Nevertheless, both the bioinspired robots and their organic counterparts only use the gliding abilities as soft-landing solutions, which are functionally limiting. Thus, a promising strategy for improvement is for the jump-gliders to have longer, more stable, and more controllable glides.

Potential applications for jumping robot with high agility usually involves travelling through tough terrains while doing inspections or sample collection. This nature opens up many opportunities for additional functions on the robots. The logical next step for a monopod jumper is naturally a bipedal runner. Jumping could be used as an obstacle-bypassing mechanism, but it cannot provide enough speed for fast locomotion. Thus, bipedal running should be a necessary function for any robot design to locomote in a practical situation. Densely forested areas are good examples of places that are not suitable for humans to work in and ideally need to be accessed by robots. Therefore, any aerial ability can be extremely helpful for robots to bypass obstacles that are too tall for jumping. Gliding ability, for example, gives the robot a method for fast locomotion as well as an aerial view of the terrain. Potential height booster could be a rocket-like combustion mechanism or power enough propellers capable of lifting the robot to mid-air.

To summarise, there are several research gaps in the current state of bioinspired

jumping robots. Firstly, even though the benefits of utilising series elastic actuation and power modulation in robotic jumping is known to the research community, insufficient studies have been done to incorporate the mechanism into functional jumping robots. Secondly, we see various examples of mechanical advantage manipulating component being widely present in both natural organisms and legged robots; however, few are combined with SEAs to explore the full benefits of both mechanisms. Thirdly, most past robot design that utilises aerodynamics are confined to having aerial abilities; but they are other forms of aerodynamic utilisation that can improve robotic locomotion such as balancing. Finally, robots that have full earthbound and aerial locomotion functions are still rear; being able to glide give raise to new requirements to the robot design including lightweightness. The detailed research gaps are illustrated along side literature review in **Chapter 2**.

1.2 Research questions

The main research question of this thesis can be described as **"How can the aerodynamic drag-inducing tails and mechanical advantage-varying knee joints of mammals inspire improvement in the agility and precision of jumping robots?"** It can be further broken down into smaller points:

1. What are the best straight-line mechanisms for robotic jumping and how to use series-elastic actuation (SEA) to help them approach the ballistic limit?

2. How can continuously variable transmission (CVT) mitigate the drawbacks of series-elastic actuators, and how can combining them improve robotic jumping?

3. Can aerodynamics aid robotic balancing; and can traditional reaction wheels be replaced by aerodynamic drag-based mechanisms for purpose of mass reduction?

4. If an aerodynamic drag-based balancing mechanism is feasible, how to design it to be as effective and efficient as possible and what are the constraints?

5. What are the best control strategies for jumping robots that locomote using CVT enhanced series-elastic actuators and balancing mechanisms based on aerodynamic effects and what advantages do they have compared to conventional robots?

1.3 Aims and objectives

The overall aims and objectives of this research can be summarized as follows:

1. Design and construct a jumping mechanism capable of high and continuous jumps with considerable frequencies enabled by a SEA that is based on a suitable straight-line mechanism.

2. Incorporate the CVT into the jumping mechanism for the purpose of structural integrity and jump height improvement.

3. Design and construct a light-weight aerodynamic drag-enabled balancing mechanism capable of precise flight-phase orientation control.

4. Conduct a thorough research on aerodynamic balancing and find the optimal drag-inducer (DI) design for the balancing mechanism.

5. Incorporate the jumping and the balancing modules to create a integrated monopedal jumping robot; and develop a suitable control strategy.

1.4 Contributions

As a result of this research, there are several contributions to the fields of legged, bioinspired, jumping robots. Some of these contributions are organised into papers, each one represents a definable stage of this research. I have four publications as the first author and several more as a co-author. This section will include a summary of all contributions made and work done for this PhD project, a list of published works as the first author with a brief introduction for each paper, and a list of papers that I contributed to as a co-author.

1.4.1 Summary of contributions and work done

- Extensive literature review is conducted on topics including bioinspired legged robots, jumpping robots, robotic balancing, and gliding robots; past studies regarding specific aspects such as straight-line mechanism, series-elastic actuation, continuously variable transmission, and aerodynamic drag are also reviewed. Through the literature review, crucial research gaps are found. They determine the objectives and focus of this research.

- A robotic tail (AeroTail) device design capable of self-righting and balancing on a point-in-plane aerodynamically is developed. The contributions regarding this study consists of a simplistic mathematical model based on the inverted pendulum (IP) and control methods suitable for balancing the proposed AeroTail, as well as computational simulations and comparison studies to quantify and

visualise the advantages of the AeroTail mechanism over traditional reaction-wheel-based (RW) tails under various circumstances. AeroTail is shown to achieve comparable balancing performance with a reduction of approximately 33.2% in peak required balancing torque compared to a conventional reaction-wheel-based approach.

- A comprehensive study on optimising the DI design for the AeroTail to maximise its aerodynamic torque for robotic balancing is conducted. The contributions regarding this study include a specialised Computational Fluid Dynamics (CFD) simulations on a selection of shapes to explore how specific geometrical features influence aerodynamic drag, with detailed explanations of the observed effects, an optimisation framework to identify the optimal frame design that maximises aerodynamic drag while adhering to predefined constraints such as weight and dimensional limits, and finally, the implementation of practical experiments using the AeroTail test platform (equipped with the optimised DI designs) to assess their real-world performance on a rotational tail mechanism with variable wind speeds along its length. The last part involves a comparative analysis of the experimental findings against the CFD simulation results and the establishment of an analytical approach for quantifying the performance variation among different DI models. Experimental results demonstrate that the proposed optimised DI configuration can increase the achievable aerodynamic torque by up to approximately 20.8% compared to baseline designs.

- A theoretical continuously variable transmission gearbox that can be incorporated into series-elastic actuators for robotic jumping is introduced. The contributions regarding this study consists of mathematical models for the hopping robot powertrain, including the CVT gearbox and a simplified model for an electric motor powered prismatic actuator suitable for iterative simulation, and a comparative simulation studies to examine the performances of both the C-SEA and regular SEA in various scenarios. The advantages and limitations of the mechanism are analysed.

- A jumping mechanism prototype is designed and constructed. This prototype transfers the theoretical C-SEA into a practical device. It utilises a rack-and-pinion based leg mechanism, a torsion spring enabled elastic element and a non-circular gear based CVT element. Experiments are conducted using the The jumper prototype; the results validate the findings from the simulations on the theoretical C-SEA and thus prove the advantage it has over conventional SEA.

- A simulation study of a monopedal jumping robot enabled by a C-SEA jumping mechanism and a AeroTail balancer is conducted. A SLIP based dynamics model is used to describe the jumping locomotion of such robot. An appropriate control strategy is implemented so the simulated robot can complete several locomotion tasks. The robot's performance is then compared to related works in the past. Results show that the integration of the AeroTail with the jumping robot can achieve stable jumping behaviour with an overall system energy consumption reduction of approximately 6.2%, while preserving comparable jump height and stability performance.

1.4.2 Publications as the first author

The publications as the first author are listed here. Some of the contributions mentioned in the previous section, namely, the mechanical design of the jumper prototype and the robot locomotion simulation study, are still in the process of being organised into paper. The publication of those papers will be a part of the future works.

1. **Sun, Jingcheng, and Chengxu Zhou. "Robust control for AeroTail and C-SEA enabled agile robotic jumping." (working title, paper in the writing process)** is the paper that we are currently working on regarding the control strategies of the integrated planar jumping robot. This work will include the optimal control methods for a jumping robot utilising a C-SEA leg mechanism and an AeroTail balancer. The groundworks for this paper have been laid in the form of simulation studies and the related contents can be found in **Chapter 6**.

2. **Sun, Jingcheng, and Chengxu Zhou. "Advancing Robotic Jumping with CVT Enhanced SEA." In Annual Conference Towards Autonomous Robotic Systems, pp. 73-84. Cham: Springer Nature Switzerland, 2024.** introduced a theoretical continuously variable transmission gearbox that can be incorporated into series-elastic actuators for robotic jumping [26]. The work in this paper serves as the theoretical introduction and the simulation study of the jumping mechanism. **Chapter 5** corresponds to the content of this paper.

3. **Sun, Jingcheng, and Chengxu Zhou. "Optimising aerodynamic drag for enhanced robotic balancing" Engineering Applications of Computational Fluid Mechanics 18, no. 1 (2024): 2430659.** presents a comprehensive study on optimising the DI design for the AeroTail to maximise its aerodynamic torque for robotic balancing [27]. The work in this paper finalises

the design of the most crucial component, the DI, on an AeroTail. The previous theoretical findings regarding the AeroTail are also validated as a result. More details can be found in **Chapter 4**

4. **Sun, Jingcheng, and Chengxu Zhou. "AeroTail: a bio-inspired aerodynamic tail mechanism for robotic balancing" In 2023 28th International Conference on Automation and Computing (ICAC), pp. 1-6. IEEE, 2023.** presents the development of a robotic tail (AeroTail) device design capable of self-righting and balancing on a point-in-plane aerodynamically [28]. The work included in this paper details the theoretical concept of an aerodynamically balanced tail mechanism, which lays the foundation to further researches on aerodynamic balancing. **Chapter 3** corresponds to the content of this paper.

1.4.3 Publications as a Co-author

I have also contributed in the research and writing of several other works during my PhD project. Although these works do not necessarily fit into the narrative of this thesis, they are all within the realm of legged, bioinspired robotics. They are listed here.

1. "Performance and usability evaluation scheme for mobile manipulator teleoperation" Wan, Yuhui, **Jingcheng Sun**, Christopher Peers, Joseph Humphreys, Dimitrios Kanoulas, and Chengxu Zhou. IEEE Transactions on Human-Machine Systems 53, no. 5 (2023): 844-854. [29]

2. "Teleoperating a legged manipulator through whole body control"
Humphreys, Joseph, Christopher Peers, Jun Li, Yuhui Wan, **Jingcheng Sun**, Robert Richardson, and Chengxu Zhou. In Annual Conference Towards Autonomous Robotic Systems, pp. 63-77. Cham: Springer International Publishing, 2022. [30]

3. "Vision-based Gesture Tracking for Teleoperating Mobile Manipulators" Wang, Tianyu, Yuhui Wan, Christopher Peers, **Jingcheng Sun**, and Chengxu Zhou. In UKRAS22 Conference "Robotics for Unconstrained Environments" Proceedings, pp. 52-53. EPSRC UK-Robotics and Autonomous Systems (UK-RAS) Network, 2022. [31]

4. "Trigger-Assisted Ambidextrous Control Framework for Teleoperation of Two Legged Manipulators" Peers, Christopher, Joseph Humphreys, Yuhui Wan, Jun

Li, **Jingcheng Sun**, Robert Richardson, and Chengxu Zhou. In Annual Conference Towards Autonomous Robotic Systems, pp. 50-62. Cham: Springer International Publishing, 2022. [32]

1.5 Scope of research

Even though the incorporation of a gliding mechanism onto a fully functional jumping robot is a major motivation of this research, the work regarding the gliding function will only be lightly touched upon in this thesis as an introduction and foundation to future works. Instead, the main focus of the thesis is the development of a lightweight jumping robot that can potentially be integrated with a gliding mechanism when there is such demand. The idea of using a aerodynamic drag enabled balancing mechanism lays the foundation to a potential gliding-jumping robot because weight reduction and increasing the utilisation of aerodynamics are critical necessities for a conventionally earthbound robot to gain aerial capability. Therefore, the minimalistic nature of the results on the gliding function in no way undermines the importance of a balancing mechanism enabled by the utilisation of aerodynamics.

1.6 Thesis outline

In the rest of this thesis, the following contents will be addressed. In **Chapter 2** is the literature review, which will cover and analyse notable past examples of robots that either inspired or influenced this research. **Chapter 3** is the summary of work done around the development of AeroTail, a robotic balancing mechanism that generates torque using aerodynamic drag. In **Chapter 4**, an optimisation study is conducted for the drag-inducing components on the AeroTail. **Chapter 5** includes the research on a series-elastically actuated jumping mechanism that utilises continuously variable transmission. Following the previous chapters, **Chapter 6** introduces a simulation study of the integrated jumping robot combining the jumping and balancing modules. Finally, **Chapter 7** is the conclusion of this thesis, in which the plans and initial progress for future works are also included. Other supporting contents are included in **Appendix A**. Summary of notations and acronyms can be found after the conclusion chapter.

Chapter 2

Literature Review

After the general direction and research questions are defined, the literature review ensues. The literature review initially focused on the past examples and methods of designing jumping robotic legs using linkage systems since my study was inspired by the Salto robot design which uses a Stephenson-II linkage [33]. The goal was to find or design a linkage system and a corresponding optimization method that allows a jumping robot to outperform Salto on the jumping agility metric. However, as the research progressed on, it was clear that there are many other straight-line mechanisms used on robotic jumpers and hopper. Therefore, the possible solutions that are way more simplistic than linkage were largely explored as well. Many designs for jumping robots includes elastic elements for the storage of energy either for timed release or for power modulation. Past examples of this feature being incorporated usually takes the form of serial or parallel elastic actuators for powering the jumpers. Then, the potential strategies for utilising aerodynamics in robotic balancing are included with past example of robots using reaction wheel or tail-like devices but combining them with aerodynamic drag inducing structures. Finally, gliding has been considered as a promising additional function for the robot. Existing wing designs for gliding robots were reviewed as well as potential height boosting mechanisms to enable gliding. Inspiration for optimal wing shape design was drawn from past and existing sailplanes since their wings were designed to perform long and stable glides. At the end of this section, the gaps in the current literature will be explored and they serve as justifications to the existence of this research.

2.1 Robotic Jumping

2.1.1 Bioinspiration

The Galago, for example, can jump to a $1.74m$ height in a single jump producing $191W$ of power in the process and maintain an average $1.5m$ height in continuous jumps [20]. It is able to do that due to its tissue composition having power modulation ability thus amplifying the power during jumping. It is said that 60% percent of the power comes from the bi-articular calf muscle which is behaving elastically, storing and releasing energy during jumps. The existence and structure of the tendon-muscle complex in Galago's leg effectively amplifies the power by 15-fold. Bullfrogs can jump to a distance of $1.3m$ with $31.5°$ of angle and with power of $193W$ on average [22]. Cuban tree frogs can reach a jumping distance of $0.95m$ with a body-mass-specific power of $91W/kg$ during the takeoff period [23]. The geckos can utilize the circular movements of its tail to control yaw and pitch as it descends when hopping between trees [34]. This is also an inspiration of the pitch controlling tail on the Salto robot design.

2.1.2 Straight line mechanisms

Prismatic actuators and rimless wheels

Maarten J. van den Broek [35] claims that bipedal running gaits may be self-stable if they rely on the intrinsic system dynamics to attenuate deviations. A virtual pendulum model can be applied in robotic design to achieve passive stabilization. Planar elliptical runner was compared with planar spring-loaded inverted pendulum model with a trunk (TSLIP). The HexRunner and the planar elliptical runner are two candidates for the experiment and unfortunately, the planar elliptical runner was chosen. Thus, the HexRunner has no detailed description and all information were gathered from a related video. Another example of bipedal running robots that utilize a straight-line system is the Cassie robot [36] [37].

In a video introducing the HexRunner robot claims that the dynamics and energetics of the runner does fit the criteria of a running robot rather a wheel because of the fact that it has a "flight phase" (in which no leg is touching the ground). However, the concept of having unactuated compliance legs around a rotating platform generally falls under the umbrella term "rimless wheels", and because of the unactuated legs, they cannot perform jumping. Sebastian Sanchez et al. [38] define the rimless wheel, or a wheel without a rim the simplest example of a legged robot. The device in this paper is torso-actuated, which is also the actuation method for HexRunner.

For a rimless wheel inspired robot with potential jumping ability, individual legs

must be actuated. J. Blake Jeans et al. [39] presented a walking robot (IMPASS) with spokes which expand and contract (thus actuated) as the methos of locomotion. A spoke can actuate by expanding and contracting and behave as a robotic leg is, in natural, a prismatic joint. Nicholas Paine et al. [40] introduced the most desirable design so far. Although the device was designed for high frequency motions, the structure of the prismatic series elastic actuator could be used in robotic legs for jumping. There are also some examples of engineers using the rimless wheel configuration as the basis for developing bipedal walking gaits [41] [42] [43].

Rack-and-pinion, ball screw and ServoBelt

An online article was found about a bipedal walking robot designed by SCHAFT. Although there was no published paper behind it, but an extremely similar design SLIDER [44] [45] was found. Slider is a walking robot, thus the most valuable feature to my research is its prismatic actuator called ServoBelt linear drive. ServoBelt is said to have a light-weight, low cost, high precision and high maximum load comparing to other more traditional prismatic joint transmissions like lead/ball screws or rack and pinion drives.

There were concerns about the speed of linear actuation that a ball screw can provide being not sufficient for jumping. After going through some websites of companies that manufactures "high speed" linear actuators, this conclusion is confirmed to some degree. In fact, most existing linear actuators in machinery or those I found online for sale use either ball/lead screw or pneumatics/hydraulics as their actuation method. Ball screws and pneumatic cylinders in general are used for slow speed actuation with high load (lifters and jacks) or high-frequency back and forth motion (jackhammers and example in [40]). Any actuator capable of extending a suitable distance for jumping does so in an insufficiently slow manner.

The actual problem with the lead/ball screw for jumping actuation is that the linear motion when landing should be easily transferred into the elastic element, but the ball screw gives the motor too much mechanical advantage, which cause the kinetic energy cannot be efficiently absorbed by the elastic component. Therefore, the elastic component should be placed between the ball screw and end-effector but not between the motor and the screw (rotational spring) if one is to be used.

In the papers [7] and [7], the hopper design does exactly that. The passive springs and the rack-and-pinion actuator are two separate components connected in series and the spring is right between the rack and end-effector. The robot also has another degree of freedom allowing it to hop forwards. The paper [8] demonstrates and discusses many monopod-hopper designs that have largely the same design philosophy. The monopods seem to be a trend in the 80s and 90s and there are sufficient previous

examples for me to explore [46] [47] [48]. The structure of their actuators is very similar to the one in previously mentioned paper but they actually utilize pneumatic cylinders and ball screws as their transmission. However, this is not evidence of the ball screw and pneumatic cylinder being absolutely suitable for my research because the hoppers are not mean to be jump high but just enough to locomote. Still, the examples presented by A. Sayyad et al. seem to contradict the conclusion I made through searching for in-service linear actuators online. This uncertainty and lack of details will lead to the formation of my future plans.

Linkage systems

The Stephenson-II six-bar structure is a popular choice for linkage-based straight-line mechanism. There are two papers detailing the design process for Salto's leg design. In the first paper [49], D. W. Haldane et al. presented the energetics and the test results of the Salto leg and the reasoning behind expanding the six-bar linkage into an eight-bar one. This paper focus on the fact that the serial elastic nature of the leg transmission enables the robot to use power modulation in order to generate impressive peak power for jumping. The Stephenson-II six-bar linkage was used on the prototype for Salto but it was replaced by eight-bar linkage with most other features unchanged to tackle the body rotation problem. A second paper [33] was found later but it predates the first one and explains the selection and design process for the original six-bar linkage used on the Salto prototype. Comparing to the first paper, this paper mainly focuses on the design and optimization of the linkage system. It is clear that the main reason that the six-bar linkage was chosen is its ability for the trajectory of the end-effector/ground reaction force to pass through the center of mass as a straight line with only one degree of freedom. The largest contribution of this paper is the extensive research the authors did on the various types of linkage system could be fit for related tasks and the huge number of referenced papers on the basic design ideas of jumping robots.

For the Stephenson linkage system specifically, the paper [33] provides a detailed design process of the Salto leg which utilizes said system. One of the steps involves using a function generator that produce an atlas of linkage designs that fulfills the same end effector trajectory. An optimal arrangement will then be chosen from the variations given. This generator is introduced and demonstrated in the paper [50]. This method is useful for exploring the possible designs of linkage arrangements given the task and design criteria. Further explanation of the same approach can be found in the papers [51] [52] [53]. The next step for the Stephenson linkage is to learn the optimization methods that are available and commonly used to improve the parameters of a linkage to fit specific tasks.

Another option is the Hoeken's four bar linkage. One typical example using this mechanism is the tactical hazardous operations robot (THOR) [54] [55]. The actuator for its knee joint utilizes an inverted Hoeken's four bar linkage [56] [57]. The Hoeken's linkage usually translates rotation into linear motion. By inverting it, linear motion generated by a ball screw motor can be turned into the rotations of the knee joint. This device is able to keep the mechanical advantage high and constant for the motor at any given angle of the knee joint. An interesting feature of the device is the use of cantilever beam as elastic element [58] (this design can also be found on a similar robot SAFFiR [59]). The bending of the cantilever beam provides some compliance and flexibility for the system. This design is a further look into the realm of linkage systems; it will be put aside for the moment since the main focus is prismatic actuation.

2.1.3 Incorporation of elastic elements on jumping robots

Series-elastic and parallel-elastic actuators

Since power modulation is an essential part of achieving required power for high jumping agility, its necessary condition of having a serial elastic actuator is also vital. Martin grimmer et al. [60] explained the trade-offs between series- and parallel-elastic actuators (SEAs and PEAs), and the conclusions are listed. PEA can reduce peak power better than SEA by pre-loading the spring in the flight phase. This loading needs additional energy so that the ER increase in comparison to the SEA. The SE+PEA concept can further decrease the PP and ER are less than PEA but higher than SEA. Mimicking human ankle joint behavior in running and walking at higher speeds is still challenging for single motor devices. Both SEAs and PEAs were used in the design of Eleg [61] [62], which is a three-degree-of-freedom compliantly actuated robotic leg that also uses a bio-inspired biarticulated tendon. Biarticulated muscles commonly found in biological systems saw increased adoption into robots, but the combination with elastic compliance was rare. The experiments in the paper proved that the energy consumption when jumping reduced by 68% by using a biarticulated energy-storage branch.

Robots with elastic elements

From the examples of jumping robots searched from mechanism types, it is found that huge amount of jumping robot designs involves a mechanical trigger-and-release system to use the energy pre-stored in springs for locomotion (examples: Grillo [63], Flea Catapult [64], ParkourBot [65]). A very innovative jumper design that uses a combination of rubber bands and carbon fibre "bows" as its elastic elements was

found [66]. This robot is designed to maximise the specific energy of jumping and it manages to reach a height of 30 meters, which is higher than any engineered jumper before. There is even a jumping mechanism design combining combustion and a spring element [67]. This is useful in terms of demonstration when combined with a miniature robot that usually has a simplistic structure. However, they are incapable of power modulation within a single jump and being fine-tuned in control. The most practical structure for a robotic leg capable of jumping is still the linkage system.

Power modulation

In the same paper [33], there two most important design criteria for the leg design that enables power modulation. The required behaviors of the leg include possessing low mechanical advantage at the top of the stroke and that its mechanical advantage defines a constant ground force for the remainder of stroke. These requirements reveal more insights of power modulation. Low mechanical advantage essentially multiplies the weight of the robot (even though the force acting on the linkage is high; it does not expand much) allowing the motor to operate near its stall torque and to transfer energy into the series elastic spring element. Once the leg extends past the low region of mechanical advantage, the increased one (in high region) triggers high-power energy transfer from the spring into the linkage and thus vertical motion of the jumper. At the same time, the linkage should transfer the unwinding spring torque into a constant force at the end-effector by its altering mechanical advantage during the expanding process.

2.1.4 Continuously variable transmission

Series-elastic actuation (SEA) is frequently used in robots designed for continuous hopping [68, 69] due to its ability to reduce energy consumption and peak torque requirements [70]. During continuous hopping, the elastic element can absorb and store the energy from the last jump as the robot lands and releases it into the next jump. However, previous studies on robots that use SEA often emphasize their agility rather than jump height. This preference stems from the common use of parallel-elastic actuators (PEA) to achieve high jumps for their ability to preload the spring during the flight phase [60]. Nonetheless, PEAs do not have the aforementioned benefits of energy conservation and torque reduction, making an SEA with enhanced jump capability the ideal actuator for hopping robots.

To optimise jump height while retaining the advantages of an SEA, the Salto robot provides a solution to improve the power modulation ratio (ratio between peak power output from a mechanism and that of its actuator) by having a linkage system with

variable mechanical advantage (MA) as its leg mechanism [33]. However, the design process of a linkage system requires complex kinematic tuning to produce a desired MA profile. In contrast, a continuously variable transmission (CVT) can produce the same MA profile with much simpler structures. Furthermore, while the Salto robot does manage to improve the peak power output of the jumping mechanism, this enhancement does not directly contribute to the jump height, which is determined by the upward velocity of the robot body at the moment of leaving the ground. Therefore, the exact manner in how having varying MA increases the jump height of SEA-actuated hoppers needs to be further researched.

Previous studies have also incorporated CVT in robotics [71, 72], but they often focus on wheeled robots instead of legged ones. Some studies utilise CVTs with compliance as the method of changing MA [73, 74] but hardly any combine them with a SEA. One study investigates a CVT-SEA combination [75], mainly focusing on the control strategy for such actuators instead of specific scenarios for jumping application. Hence, the concept of CVT-enhanced SEA is novel for robotic jumping and necessitates mathematical modeling and simulation to evaluate its performance.

2.1.5 Actuation Paradigms comparison

The actuation paradigm adopted by a legged robot strongly influences its ability to generate large transient forces, manage, and exchange energy efficiently. This is particularly critical for jumping robots, where energy is rapidly injected, stored, and released over short time scales. Broadly, three actuation strategies are commonly employed in legged robotics: conventional high-ratio geared drives, quasi-direct drive (QDD), and series elastic actuation (SEA).

Conventional high-ratio drives, typically realised using harmonic, planetary, or cycloidal gear trains, amplify motor torque through large reduction ratios [33, 35]. This approach enables high continuous joint torque with compact motors and has been widely used in early legged robots. However, the high reduction ratio increases reflected inertia and friction while reducing backdrivability and force bandwidth. As a result, impact loads and rapid force transients are transmitted directly through the drivetrain, making this paradigm less suitable for highly impulsive behaviours such as jumping, where robustness and efficient energy exchange are critical.

Quasi-direct drive actuation has emerged as a dominant paradigm in modern agile legged robots, particularly for locomotion involving continuous ground contact [36]. By combining high-torque-density motors with low transmission ratios, QDD systems achieve high force bandwidth, backdrivability, and accurate torque control. These properties are highly effective for dynamic interaction and locomotion tasks such

as running and trotting. However, for jumping behaviours, the low reduction ratio places stringent demands on the motor and structure during peak loads and impacts. Moreover, because QDD systems typically lack an explicit elastic element, their ability to mechanically store and reuse energy across jump cycles is limited, and energy must instead be supplied and dissipated primarily through the motor and controller.

Series elastic actuation introduces a compliant element between the motor and the load, enabling mechanical energy storage and release, impact mitigation, and force modulation through spring deflection [40]. These characteristics align naturally with the dynamics of jumping, where energy is accumulated during a charging phase and rapidly released to generate lift-off. By allowing a significant portion of the mechanical energy to be stored elastically, SEA can reduce peak motor power requirements and electrical energy consumption, particularly during repeated or continuous jumping motions.In this thesis, the continuously variable transmission enhanced SEA (C-SEA) is considered a special case of SEA in which an additional gearbox is introduced to modulate the effective transmission ratio. This extension preserves the fundamental energy storage and impact-mitigation benefits of SEA while enabling improved jumping agility. A qualitative comparison of these actuation paradigms is summarised in Table 2.1.

Table 2.1: Qualitative comparison of actuation paradigms for dynamic legged robots.

Paradigm	**Key advantages**	**Key limitations**	**Suitability for jumping**
High-ratio geared drive	High torque; Compact motor sizing; Mature technology	Low backdrivability; High friction; No compliance;	Poor
Quasi-direct drive (QDD)	High force bandwidth; Backdrivable; Accurate torque control	Loads borne by motor; Limited energy storage; High electrical demand	Poor
SEA / C-SEA	Energy modulation; Impact mitigation; Reduced motor effort	Mechanically complex; Lower bandwidth	Well suited

2.2 Aerodynamic Robotic balancing

Contemporary machines and devices, such as drones, satellites, legged robots, rockets, and underwater vehicles, necessitate active re-orientation and attitude error correction to maintain balance. These machines perform critical tasks, including telecommuni-

cations, inspection, cargo delivery, and access to non-human-friendly environments. To fulfil their intended functions, adherence to specific payload requirements and limitations is paramount. Thus, it is essential that additional, yet necessary payloads, such as balancing mechanisms, are minimised.

2.2.1 A novel strategy to balance

Various balancing methods exist for these devices and vehicles, with reaction wheels being the most widely used approach. Employing inertial forces to provide balancing torques, reaction wheels are particularly prevalent in satellite applications, where external forces are challenging to obtain in space [76, 77]. In fact, the use of reaction wheels on satellites is common enough that there is a report by W. Bialke and E. Hansell in 2017 [78] explaining a systemic reaction wheel failure in currently serving satellites. Even though most studies on said topic focus on the dynamic analysis and mechanical innovations, new ideas for controlling the reaction wheel are also being introduced. For example, a fault tolerant control for satellites is presented in this paper [79]. Fault tolerance means the system is able to maintain performance and stability even with unexpected faults in the system. By using the proposed dynamic model and time-delay control, the attitude error of the satellite can be reduced to 10% of the original value in around 110 seconds.

In robotics, reaction wheels have also been utilised for balancing and re-orientation purposes. Research in this area frequently employs dynamic models based on the inverted pendulum [80–82], with a primary focus on control. One such study [83] introduces a dynamic model for balancing robots on a point-in-plane and demonstrates an example robot that utilises a reaction wheel-style crossbar for balance. The Cubli [84], a cube-shaped robot with three reaction wheels controlling each axis, is capable of jumping up and balancing on a corner. Another popular method for robotic balancing is utilising propellers facing a perpendicular plane thus generating torque from their thrust. Notable examples include Salto [85], the slackliner robot [86], and LAWCDR [87]. Although these solutions offer some advantages, they suffer from the additional mass and structural complexity that could be otherwise reserved for their primary functions. Furthermore, unlike satellites, terrestrial robots have ample means to generate external forces for balance, and therefore, using inertial balancing as the default option may not be well justified.

Inspiration for alternative balancing mechanisms can be found in nature, where animals utilise their tails for balance during activities such as jumping and running due to evolutionary pressures [88]. Researchers have investigated the balancing role of tails and appendages in animal behaviours, including running, jumping, and self-

righting [89, 90]. Others have developed dynamic models and control systems to integrate biomimetic tail mechanisms into robots [91]. A study by [92] found that an increased tail-to-body length ratio in geckos results in a significant rise in turning rate, but the benefits of a longer tail rapidly diminish with a larger ratio. An increase of tail-to-body length ratio from 0.93 to 1.8 results in a 50% rise in turning rate. However, the benefits of longer tail diminishes rapidly when the length ratio is above 2.Thus, animal tails can be used effectively in a reaction-wheel manner, albeit with limitations.

Certain animal tails possess surface properties, typically due to fur or feathers, which enable them to induce aerodynamic drag when moving. The Cheetah's tail inspires a simplified tail device that swings in a conical motion during turns [4], achieving 70% more lateral acceleration with a tail than without one. Wind tunnel tests quantify the aerodynamic forces on the tail, revealing that the fur nearly doubles the effective frontal area [93]. The aerodynamic effects contribute to the angular impulse imparted by the tail onto the cheetah's body. In these experiments, aerodynamic torque surpasses inertial torque as the tail accelerates at around 0.05 s, albeit with diminishing increments thereafter. The results show that 26% of the pitch angular impulse is induced aerodynamically even though the tail only takes 2.5% of the body mass [94]. A study by [95] demonstrates that a squirrel's bushy tail, despite comprising just 3% of the body mass, has a projected area that can reach around 55% of the body size in a side view during jumping. The aerodynamic torque produced by the tail is smaller but comparable to the inertial torque.

These animal-related studies suggest that although animals can balance using their tails in a purely inertial manner, tails with aerodynamic properties significantly enhance the generated righting torque. In some cases, the aerodynamic torque induced by the tail even exceeds that produced by its inertia, suggesting that a tail's torque-generating capability could be derived entirely from its aerodynamic properties, rather than its mass. Consequently, it is theoretically possible to design a mass-less robot-balancing tail that relies solely on its aerodynamic nature to generate righting torques, thus addressing the problem of unjustified additional payload from reaction wheel mass.

2.2.2 Aerodynamic drag maximisation

Balancing and re-orientation are integral functions for a multitude of machines and devices currently in operation. Various approaches exist for these functions, with the reaction wheel being the most prevalent. This mechanism utilises inertial forces to generate balancing torques. Contemporary studies often showcase robots maintain-

ing equilibrium through reaction wheels; for instance, the Cubli [84]–a cube-shaped robot–can jump and balance on a corner, thanks to three reaction wheels that control each axis. Interestingly, this method is mirrored in nature. Animals, particularly those adept at jumping and running, often exploit the inertial properties of their tails for balance and re-orientation, a trait developed through evolutionary pressure [88]. A notable example is geckos, where a larger tail-to-body length ratio correlates with improved turning rates [92]. Consequently, biomimetic research endeavours to transplant these animalistic traits into robotic systems [91].

In certain animals, tails induce aerodynamic drag, attributed to features like feathers or fur. For instance, the fur on a cheetah's tail significantly increases its frontal area, enhancing aerodynamic drag [4, 93]. This drag force contributes to the angular impulse of the tail, thereby assisting in lateral acceleration during turns. Similarly, squirrels' bushy tails exhibit remarkable aerodynamic properties, with the drag-induced torque rivalling that generated by inertia [95]. These insights suggest the feasibility of a purely aerodynamic, mass-less tail device for robot balancing, circumventing the added payload issue inherent in reaction wheels. This notion inspired our preceding work, AeroTail, a simulated investigation into a tail device that achieves balance aerodynamically on a point-in-plane, employing a dynamic model akin to the inverted pendulum [28]. In this study, the drag-inducing elements of the AeroTail are termed "drag-inducers" (DIs). However, the specific design of these DIs was not finalised. This leads to the pivotal question: what constitutes the optimal design for a drag-inducing device in an aerodynamically balanced tail?

Traditionally, aerodynamic drag is calculated using the drag equation [96]:

$$D = \frac{1}{2}\rho C_d v^2 A \tag{2.1}$$

where D represents the drag force, ρ is the fluid density, C_d denotes the drag coefficient, v signifies the flow velocity and A is the object's effective area. Within this equation, the drag coefficient and the effective area are specific to the object, or in this context, the drag-inducing device. The DI's effective area is constrained by its surroundings or the overarching geometry of the device to which it is attached, while the drag coefficient is shaped by the DI's form and can vary considerably. Hoerner's seminal work on fluid dynamic drag includes wind tunnel experiments for numerous standard shapes [96]. These experiments provided data for both 3D shapes and 2D profiles sandwiched between wind tunnel walls. Remarkably, a hollow semi-sphere facing the wind yields an impressive drag coefficient, a design employed in parachutes and anemometers. The hollow semi-cylinder also exhibits a high C_d of 2.3, the highest among all tested shapes, and has been utilized in robotic self-righting devices [97],

demonstrating a more practical C_d of 2.0. A further study [98] corroborated these results and extended the range of shapes examined.

However, these solutions are not exhaustive. The aforementioned wind tunnel tests predominantly focused on common, intuitive shapes, lacking a numerical framework for quantifying and optimizing shape features in specific scenarios. Numerous studies have sought to address this by developing mathematical models for irregular shapes [99], aiming to determine their drag coefficients. While most research concentrates on minimizing drag [100] for applications like vehicles and aircraft, others have devised analytical solutions for irregular, sphere-like shapes [101]. However, these methods have limited applicability for cup-like shapes. Additionally, the wind tunnel results, typically from controlled environments, may not accurately represent real-world performance. For example, the 2D "prism" shapes in the sources [96, 98] (detailed comparison in Table 4.2) yielded unrealistic drag coefficients achievable only by infinitely long objects, a limitation absent in practical scenarios. Therefore, it's prudent to undertake computational fluid dynamic simulations on specific shapes to ascertain the most effective design for the DI. Moreover, optimizing both the highest C_d and the effective area of the DI are crucial and distinct aspects of this problem, each significantly affecting the DI's induced drag. Hence, a methodology to maximize the DI's frontal area within given constraints is also essential.

2.3 Control strategies for jumping robots

Among the aforementioned example of past robot designs, many have the ability to jump but they do not necessarily use jumping as their primary method of locomotion. This could be due to their inability to achieve continuous jumping, or simply, the fact that walking or running align more with their design criteria. However, even being visually different, there are intrinsic similarities between the dynamics of walking, running, and jumping so much so researcher and engineers often use the same model to describe them. The spring-loaded inverted pendulum model (SLIP) was first introduced in 1989 by R.Blickhan to model the dynamics of running and jumping behaviours in animals [102]. He observes that animals' centre of mass during running behaves like a point mass bouncing on a spring leg; the leg compliance leads to energy exchange between kinetic and potential forms. This provides a simple, predictive template for analysing gait mechanics for running and jumping. [103] confirms the similarities in the energy exchange patterns of running and walking and provides biomechanical justifications for SLIP-based robot designs.

Various past robot design have incorporated the SLIP model in their control strategies. [46] introduced a 3D hopper which is able to achieve controlled locomotion on

a surface plane without physical support. This robot also utilises a simple controller that enables it to achieve horizontal jumping velocity control [104]. Some designs also adds an extra torso joint between the leg and the body, creating a mismatch between the centre of mass of the body and root of the leg; and this helps the robot to balance in the flight phase. For example, in [105] and [106], the authors developed a two-level control method: the continuous level for torso stabilization and an event-based level for step-to-step locomotion. This method bridges the non-linear control theory framework with Raibert's empirical controller.

Other methods are also used for the balancing and orientation control for the robot's flight phase. For example, [107] introduced the Salto robot which utilises a reaction wheel directly acting on the centre of mass of the robot body to provide control torque; no torse joint is needed in this case. They developed a deadbeat foot placement controller for the robot and they concluded that the attitude error is the main limiting factor to the precision of high robotic jumping. Similarly, authors of [108] use two arm-like mechanism to maintain the balance of their robot's flight phase. The principle and dynamics of the arms are identical to reaction wheels and only difference is that they have smaller range of motion. This robot implemented a hybrid reinforcement Learning (DDPG) and PD control method which is more robust than traditional strategies.

Some works even include the torque element in the stance phase control, directly implementing a reaction wheel (flywheel) into the SLIP model itself. For example, [109] introduces the Flywheel-SLIP model which see the flywheel also actively generating torque on during the stance phase; thus, both the vertical and rotational momentum are taking to account in their stance dynamics. Similarly, authors of [110] propose the torque-enhanced active SLIP by adding a hip torque actuator. This work also develops a partial feedback linearization method that allows closed-form stance solutions and greatly expands the stability region of apex return map. However, this model is not without limitations. For one, the stance phase is relatively short compared to the flight when high jumps are achieved meaning the flywheel has a smaller window to take affect; also, the motion of the robot body is way more susceptible to gravity on the ground which could pose high requirement to the torque actuator's capacity. Therefore, working during the stance phase could greatly undermines the effectiveness of the flywheel when compare to its "natural habitat", the flight phase.

Past robot designs have expanded the reaction wheel method into 3D version and we often see robots that use 3 reaction wheels placed diagonally to each other to achieve 3D jumping locomotion. For example, the REx hopper [111] and the ARCHER robot [112] use exactly that configuration. The former design also implements model predictive control with a lumped-mass model and a hybrid floating-body

formulation. This is the most popular way of achieving 3D locomotion for monopedal jumping robots. However, the obvious drawback is the added weight from the reaction wheels. Since they require inertia to function, one can already significantly increase the overall mass of the robot, let alone three.

Many researcher also try to improve or optimise the SLIP model itself for either faster calculations or more versatile controlled task options. For instance, [113] and [114] both made attempts to simplify the SLIP model by introducing approximation methods that are faster than the regular numerical integration. The former one develops a piecewise-linear, time-invariant SLIP approximation that provides closed-form solutions for stance and stride maps; the latter one introduces a sine-wave approximation for horizontal ground reaction forces and is able to handle large, asymmetric steps, which is difficult for regular passive SLIP. Researches have also been done to expand the theoretical versatility and generality of SLIP-based control. [115] extends the originally planar SLIP model into a 3D version and proposed a 3D hybrid feedback control methods for quadrupeds. [116] defines generalised SLIP which is parametrised to cover many SLIP variants including rolling foot, two-segment, and torque-driven; it can be used as a robot leg morphology design guideline. [117] takes a step further and introduces the Wheeled-SLIP model which added wheel dynamics to the end of robot legs. It demonstrates a LQR-based task-space whole-body controller with disturbance observers.

2.4 Gaps in the current literature and conclusion

The many research results being covered above look promising in their own right, but there are much to discuss and explore and find the gaps for this research to fit in. Jumping agility is a new concept that brings the bioinspired robots and their organism counterparts closer. The common practice for any bionic engineering is to only consider a limited aspect of inspiration, which is the reason that most jumping robot only focus on one metric. With the concept of jumping agility combining both height and frequency, the robots are practically competing on the same level with natural organisms. In order to maximise this metric, energy storage branch using elastic elements in a jumping mechanism becomes the logical solution; even though having the storing and releasing processes to be present in a single stroke is still novel. This design needs to be enabled by the power modulation feature, which describes when a mechanism has a mechanical advantage (MA) profile that changes within a single stroke. This is the reason that linkage was chosen as the leg transmission for the Salto robot for its built-in MA profile. However, a changing but predictable mechanical advantage can be realised using other methods. The linkage system, at

the same time, is not without its faults. For instance, a linkage with a complex structure capable of straight-line motions for its end-effector is only approximating the trajectory; in other words, they are hardly true straight lines. This alone would put emphasis on excessive calculations and simulations that can be otherwise avoided.

For aerodynamic robotic balancing, we found that although animals can balance using their tails in a purely inertial manner, tails with aerodynamic properties significantly enhance the generated righting torque. In some cases, the aerodynamic torque induced by the tail even exceeds that produced by its inertia, suggesting that a tail's torque-generating capability could be derived entirely from its aerodynamic properties, rather than its mass. Past robot design that does incorporate aerodynamics usually use tail like structure that has one end (instead of its centre of mass) attached to the body to be balanced, which is structurally very different from the reaction wheel. We have yet to see a balancer that can replace the reaction wheel without significantly changing the robot structure or the dynamic model. Furthermore, alternative aerodynamic solutions like propellers also suffer from the limitations of weight and compactness. Additionally, we found the aerodynamic drag coefficient data from past studies are usually from unrealistic wind tunnel conditions or simulations in less than universal scenarios. They are not useful in terms of determining the best drag-maximising method in a robotic balancing scenario.

In terms of the jumping control strategy, most past jumping robot design utilise SLIP or SLIP-based variants for dynamic model and controller. Even though most of them works well for their intended purpose, there is still room for improvements especially for the leg mechanism structure. Dynamic models used in past robot designs do include a spring element for the leg but most of the them use motor driven joints at the end, only few actually incorporate SEAs in the leg mechanism. Moreover, none of the past designs have integrated gearbox specifically between the spring element and the end-effector meaning in order to control a robot with such leg structure, a new variant of the SLIP must be developed to suit the job. Furthermore, none of the balancer choice, whether it be torso joint, arms, or reaction wheels, utilise aerodynamics as the source of torque input; novel control strategies could be introduced for this application.

In this section, the literature regarding jumping robots, their natural organism counterparts and potential leg mechanisms were reviewed; research were also done to find the best strategies to utilise aerodynamic drag for robotic balancing and to maximise the drag on a single device. It is clear that there are many gaps in current literature where further improvements can be made. This research will try to improve upon the limitations of past designs and ideas; it will also serve as an organic and logical progression of them in order to achieve innovations.

Chapter 3

AeroTail: the Utilisation of Aerodynamic Drag in Robotic Balancing

This chapter presents the development of a robotic tail (AeroTail) device design capable of self-righting and balancing on a point-in-plane aerodynamically; it introduces simplistic mathematical models based on the inverted pendulum (IP) and control methods suitable for balancing the proposed AeroTail; and it includes computational simulations and comparison studies to quantify and visualise the advantages of the AeroTail mechanism over traditional reaction-wheel-based (RW) tails under various circumstances.

3.1 Mathematical Modelling

To design and simulate a robot-balancing tail device, a dynamic model of the device and a simplified robot must be established. This model should be general enough to represent most scenarios where the tail is expected to be used. As mentioned in Section 2.2.2, studies regarding reaction wheels often build their dynamic models based on the inverted pendulum (IP); its structure can be described as a massed object whose gravity does not align with its contact point with the surroundings. This means that most devices, especially legged robots, which require active balancing, can be well represented by the IP model. The example robot mentioned in [83] utilises a dynamic model for balancing on a point-in-plane, which simplifies the IP balancing problem to a degree that is suitable for simulation but still representative of wider scenarios. Therefore, the dynamic model for this work will primarily be based on the point-in-plane concept for IP, and further mechanisms will be developed on top of it.

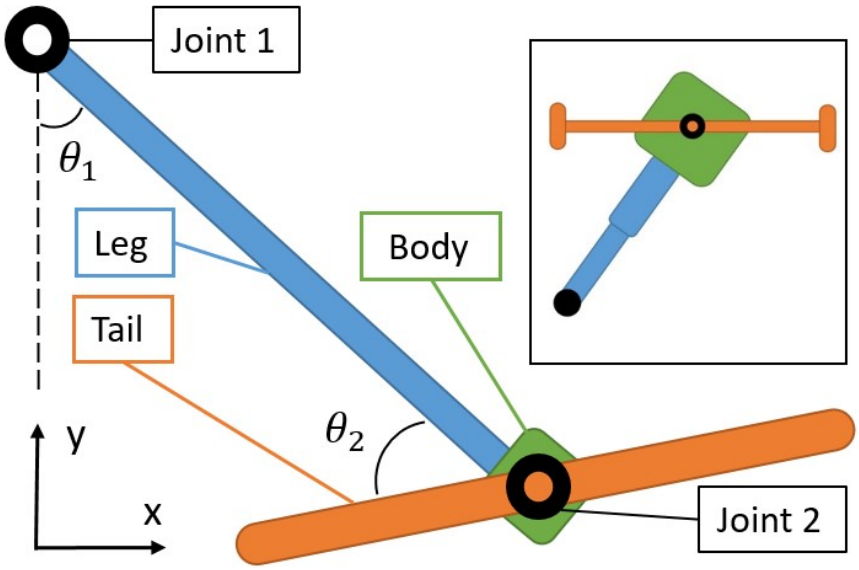

Figure 3.1: The double-rod pendulum system. θ_1 is the angle between the vertical hanging position and the leg, while θ_2 is that between the leg and the tail in the same direction. The small picture in the top-right corner is an example jumping robot with equivalent components marked in the same colour as in the model.

3.1.1 The inverted pendulum model

The structure and notation of the double-rod pendulum system are shown in Fig. 3.1. The model consists of three main components: the "leg" (blue), the "body" (green), and the "tail" (orange). The leg and the body are fixed together; they both rotate around Joint 1 which connects a fixed point in the world frame with the leg. Joint 2 connects the mid-point of the tail to the body. Both the leg and the tail are uniform and rigid rods, and the body is a point mass. The masses of the leg, tail and body are m_1, m_2 and m_3 respectively. The leg has a length of $2l_1$ while that of the tail is $2l_2$. In the top right corner of Fig. 3.1 is a simple illustration of a monopedal jumping robot. The equivalent components in the double-rod model and the example robot are marked with the same colour. Compared to a realistic robot, the body in the model is largely simplified; Joint 1 can be seen as the contact point between the robot and the ground.

The equation of motion for the system can be simply expressed using the robot dynamics equation:

$$\mathbf{M}(\boldsymbol{\theta})\ddot{\boldsymbol{\theta}} + \mathbf{C}(\boldsymbol{\theta}, \dot{\boldsymbol{\theta}})\dot{\boldsymbol{\theta}} = \boldsymbol{\tau_g}(\boldsymbol{\theta}) + \mathbf{u} + \mathbf{J}^{\mathbf{T}}(\boldsymbol{\theta})\boldsymbol{\lambda} \tag{3.1}$$

in which θ, $\dot{\theta}$, and $\ddot{\theta}$ represent the positions, velocities, and accelerations of the pendulums as shown in Fig.3.1, the $\mathbf{M}(\boldsymbol{\theta})$ is the mass matrix, $\mathbf{C}(\boldsymbol{\theta}, \dot{\boldsymbol{\theta}})\dot{\boldsymbol{\theta}}$ is the Coriolis forces, $\boldsymbol{\tau_g}(\boldsymbol{\theta})$ is the gravity vectors, $\mathbf{u}$ represents the control input and $\mathbf{J}^{\mathbf{T}}(\boldsymbol{\theta})\boldsymbol{\lambda}$ denotes the

sum of external forces. The first three components can be derived using Lagrangian mechanics:

$$\frac{d}{dt}\frac{\partial T(\dot{\boldsymbol{\theta}})}{\partial \dot{\boldsymbol{\theta}}_{\boldsymbol{i}}} - \frac{\partial U(\boldsymbol{\theta})}{\partial \boldsymbol{\theta}_{\boldsymbol{i}}} = \boldsymbol{\tau}_{\boldsymbol{i}}. \tag{3.2}$$

where $T(\dot{\boldsymbol{\theta}})$ and $U(\boldsymbol{\theta})$ are the kinetic and potential energy of the system, $\boldsymbol{\tau}_{\boldsymbol{i}}$ is the sum of external forces.

The total kinetic energy of the system is:

$$\begin{aligned} T(\dot{\boldsymbol{\theta}}) =& \frac{1}{2}I_1\dot{\theta}_1^2 + \frac{1}{2}I_2(\dot{\theta}_2+\dot{\theta}_1)^2 + \frac{1}{2}(m_2+m_3)v_2^2 \\ =& \frac{2}{3}m_1l_1^2\dot{\theta}_1^2 + \frac{1}{6}m_2l_2^2(\dot{\theta}_2+\dot{\theta}_1)^2 \\ &+ 2(m_2+m_3)l_1^2\dot{\theta}_1^2. \end{aligned} \tag{3.3}$$

where I_1, I_2, and I_3 are the moments of inertia for the leg, the tail, and the motor.

The total potential energy of the system is:

$$\begin{aligned} U(\boldsymbol{\theta}) =& m_1gy_1 + m_2gy_2 \\ =& -m_1gl_1\cos\theta_1 - 2(m_2+m_3)gl_1\cos\theta_1. \end{aligned} \tag{3.4}$$

where y_1 and y_2 are the displacements of the motor and the centre of mass of the leg from Joint 1 on the y-axis.

Substitute (3.3) and (3.4) into the Lagrangian model (3.2), and the external forces can be expressed as a function of the pendulum state. Consequently, the mass matrix in (3.1) can be derived as:

$$\mathbf{M}(\boldsymbol{\theta}) = \begin{bmatrix} \frac{4}{3}m_1l_2^2 + 4(m_2+m_3)l_1^2 & \frac{1}{3}m_2l_2^2 \\ \frac{1}{3}m_2l_2^2 & \frac{1}{3}m_2l_2^2 \end{bmatrix}. \tag{3.5}$$

Note that the mass matrix is independent to position (θ). There are no Coriolis forces involved in the model, thus:

$$\mathbf{C}(\boldsymbol{\theta}, \dot{\boldsymbol{\theta}}) = \begin{bmatrix} 0 & 0 \end{bmatrix}^T \tag{3.6}$$

and the gravity vectors can be expressed as:

$$\boldsymbol{\tau}_{\boldsymbol{g}}(\boldsymbol{\theta}) = \begin{bmatrix} gl_1\sin\theta_1(m_1+2m_2+2m_3) & 0 \end{bmatrix}^T \tag{3.7}$$

3.1.2 The RW tail version of the model

When the tail is acting as an RW tail, it has mass, and there are no external forces involved. Since only joint 2 will be actuated, the control input u in (3.1) can be

written as:

$$\mathbf{u} = \begin{bmatrix} 0 & \tau_{\text{motor}} \end{bmatrix}^T \tag{3.8}$$

and the sum of external forces is:

$$\mathbf{J^T}(\boldsymbol{\theta})\boldsymbol{\lambda} = \begin{bmatrix} 0 & 0 \end{bmatrix}^T \tag{3.9}$$

3.1.3 The AeroTail version of the model

When the tail is behaving as an AeroTail, there are several changes to the model compared to that of the RW tail scenario. First of all, the tail is assumed to be mass-less in order to eliminate the inertial torque from the mass of the tail; thus, the new expressions for the mass matrix and the gravity vectors are:

$$\begin{aligned} \mathbf{M}(\boldsymbol{\theta}) &= \begin{bmatrix} \frac{4}{3}m_1 l_2^2 + 4m_3 l_1^2 & 0 \\ 0 & 0 \end{bmatrix}, \\ \boldsymbol{\tau_g}(\boldsymbol{\theta}) &= \begin{bmatrix} g l_1 \sin\theta_1 (m_1 + 2m_3) & 0 \end{bmatrix}^T. \end{aligned} \tag{3.10}$$

The sum of aerodynamic forces generated by the tail can be seen as a concentrated external torque acting on its centre of mass. Since the tail is theoretically the "end effector" in the dynamic model, the matrix of the aerodynamic torque (τ_{aero})is expressed as such:

$$\mathbf{J^T}(\boldsymbol{\theta})\boldsymbol{\lambda} = \begin{bmatrix} -\tau_{\text{aero}} & -\tau_{\text{aero}} \end{bmatrix}^T. \tag{3.11}$$

In this scenario, the aerodynamic torque is always equal to the motor torque, and the tail is always rotating at a constant velocity with no acceleration process when the velocity changes from one to another.

Generally, the aerodynamic drag can be calculated using the equation:

$$D = \frac{1}{2}\rho C_D v^2 A$$

where D is the drag force, ρ is the air density, C_D is the drag coefficient, v is the air speed and A is the frontal area. If the aerodynamic drag acts as a torque on a single point, the torque can be calculated using the method provided in [97] with the equation:

$$\begin{aligned} |\tau_D| &= \int_A Dl \, dA \\ &= \int_{L_1}^{L_0} \frac{1}{2}\rho C_D a (\omega_t l_D)^2 l \, dl \end{aligned} \tag{3.12}$$

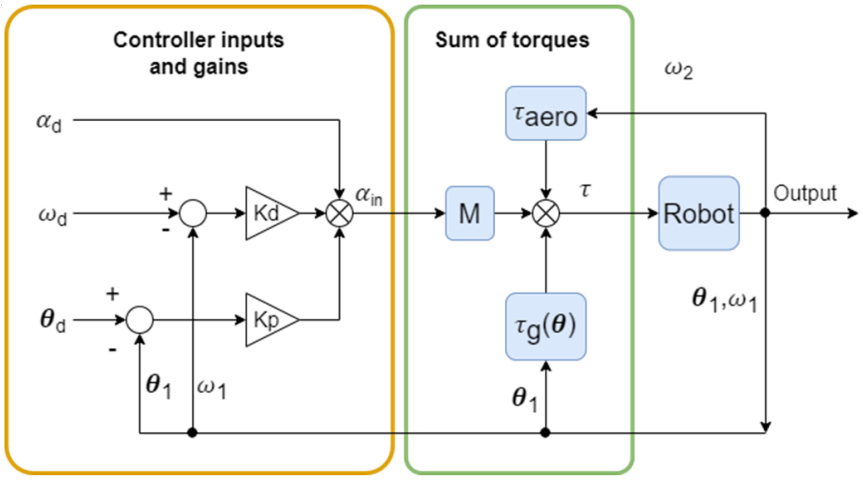

Figure 3.2: The control block diagram of the balancing model. In the diagram, α means acceleration, ω means velocity and θ represents angle position. Designation "1" is that of the body, "2" is for the tail and "d" means the desired target input.

where l_D is the length of the lever on which the drag force exerts, a is the width of the drag inducer, ω_t is the angular velocity of the tail, and $L_0 - L_1$ is the length of the lever that can generate drag assuming the drag-inducing device has a uniform cross-section along its entire length.

To adapt this equation to the double-rod system, it needs to be modified and simplified. The aerodynamic torques generated by the tail originate from the drag inducers on the tail's ends; thus, the drag generated by a single inducer is considered to act on the endpoint of the tail, regardless of its own geometry, in order to simplify the model. Consequently, Equation (3.12) can be rewritten as:

$$\tau_D = \frac{1}{2}\rho C_D \omega_t^2 l_D^3 A \tag{3.13}$$

where A is the area of one drag inducer. Since there are two of them on each end of the tail, the actual aerodynamic drag generated by the tail is $\tau_{\text{aero}} = 2\tau_D$.

3.1.4 Control method

The control method employed for the model is a classic Proportional-Derivative (PD) controller, commonly used for balancing inverted pendulums. Fig. 3.2 depicts the control block diagram of the model, in which the controller gains are represented by K_p (proportional gain) and K_d (derivative gain). his controller facilitates the balancing of the robot at a desired angle (θ_d) and target velocity (ω_d). Given that the proportional term contains the position angle error of the robot body, the derivative term error can be easily derived from the feedback velocity. Consequently, the expression for the

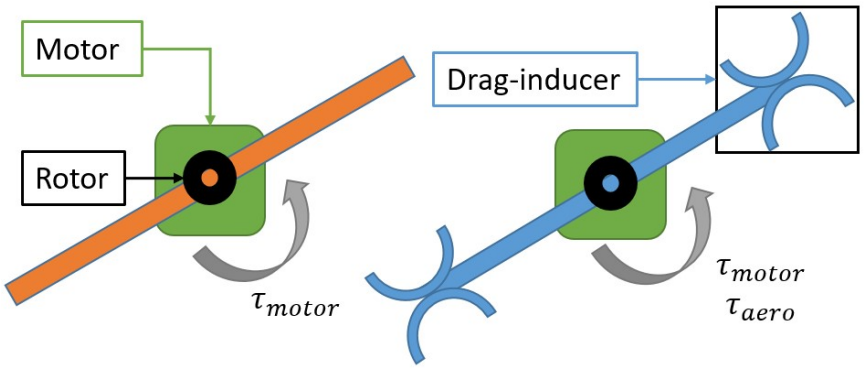

Figure 3.3: The tail models for the stand-alone tests. The motors are fixed to the world frame; the RW tail (orange) and the AeroTail (blue) have the same length. The grey arrows point out the torques acting on the tails. In the top-right box is one of the drag-inducers which generates aerodynamic torque when the tail is rotating; it can be seen as a semi-circle prism.

summed acceleration input can be formulated as:

$$\alpha_{in} = K_p(\theta_d - \theta_b) + K_d(\omega_d - \omega_b), \tag{3.14}$$

where θ_b and ω_b represent the real-time position angle and velocity of the body, respectively. The integral gain is not required, as there is no noise in the simulation environment. The controller also accounts for gravity and mass, allowing the input to be acceleration rather than torque. As a result, comparative studies in the simulation phase with fixed gains are possible, and altering the mass of components will not affect the robot's result trajectory, provided the gains remain constant.

3.2 Simulation studies

The simulation of the proposed theoretical model is performed using MATLAB. The simulation codes involve iterative calculations employing Euler's method.

3.2.1 Tails stand-alone tests

An RW tail will be compared to an AeroTail to examine their behaviours under the same conditions. The controlled variables are as follows:

- Identical motors must be used;
- The lengths of the tails must be the same.

The term "stand-alone" in this section refers to both mechanisms operating without the body. Fig. 3.3 presents the theoretical models for the tail stand-alone tests.

Table 3.1: Parameters of the tail stand-alone tests

Definition	Designation	Parameter
RW tail mass	m_I	10 g
AeroTail mass	m_D	varies
Half-tail lengths	l	5 cm
Rotor mass	m_R	5 g
Motor-torque	τ_{motor}	0.01 Nm
Aero-torque	τ_{aero}	varies
Drag coefficient	C_D	2.0

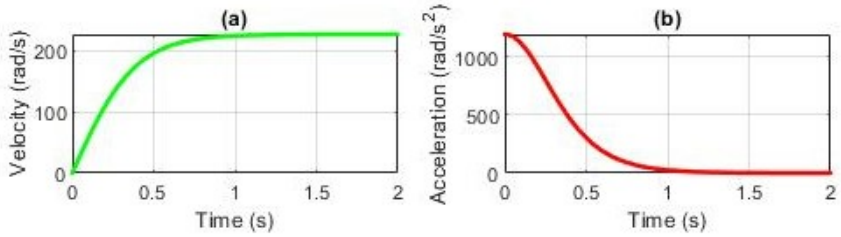

Figure 3.4: The behaviour of the aero-balanced tail with mass. (a) The velocity of the tail versus time. (b) The acceleration of the tail converges to zero.

The black circles in the middle of the rods symbolise the motor rotors (the rotor is assumed to be a uniform disc with a diameter of 2 cm). The effective area of a drag-inducer is equal to the width of the prism multiplied by the diameter of the semi-circle. Parameters for the simulations are detailed in Table 3.1.

The behaviour of an AeroTail with mass

The first simulation aims to demonstrate the behaviour of a reaction wheel capable of generating significant aerodynamic drag from its rotation when driven by a constant torque from the motor. In this case, m_D is 10 grams and torque input is τ_{motor}. The additional τ_{aero} is calculated using the aerodynamic model in Section 3.1.3, assuming the drag acts on the ends of the tail. The drag coefficient is 2.0, that of the semi-circle prism [97], and the contact area is set to be 5 cm^2 on each end. The simulation results are shown in Fig. 3.4. The acceleration of the tail eventually ceases when it reaches the maximum velocity because the torque provided by the motor equals the torque generated by drag. Unlike pure reaction wheels, which need to keep accelerating to generate torque by inertia, AeroTail can fulfil the same function with a constant velocity.

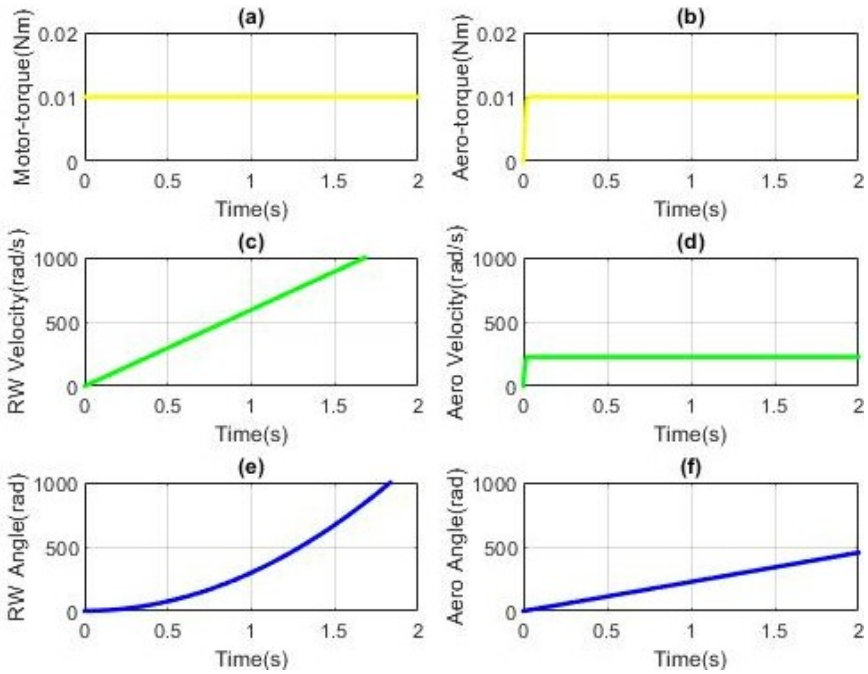

Figure 3.5: The comparison between aero-balanced and reaction-wheel tails. (a) The torque provided by the motor. (b) The aerodynamic torque generated by the AeroTail. (c) & (d) The velocities of the tails versus time. (e) & (f) The angles of the tails versus time.

Comparison between AeroTail and RW tail

To compare the mechanisms, the correcting torque generated by the AeroTail is assumed to be predominantly aerodynamic, thus m_D is zero and the tail provides no inertial torque; simultaneously, the RW tail has no aerodynamic property in this section. Fig. 3.5 illustrates the comparison between the AeroTail (right) and RW tail (left), with all other conditions remaining the same. Because the AeroTail is mass-less and the inertia of the rotor is negligible, its angular velocity nearly instantaneously reaches its maximum. The net energy consumption is also calculated as the total energy output from the motor. During the test, the AeroTail used 4.53 J, while the RW tail consumed 11.99 J.

3.2.2 Scenario tests

For scenario tests, the tails will be used to balance a robot body based on the model in Section 3.1. This implies that, unlike the stand-alone tests, the motor output during balancing will be controller-driven using the control method mentioned in the same section.

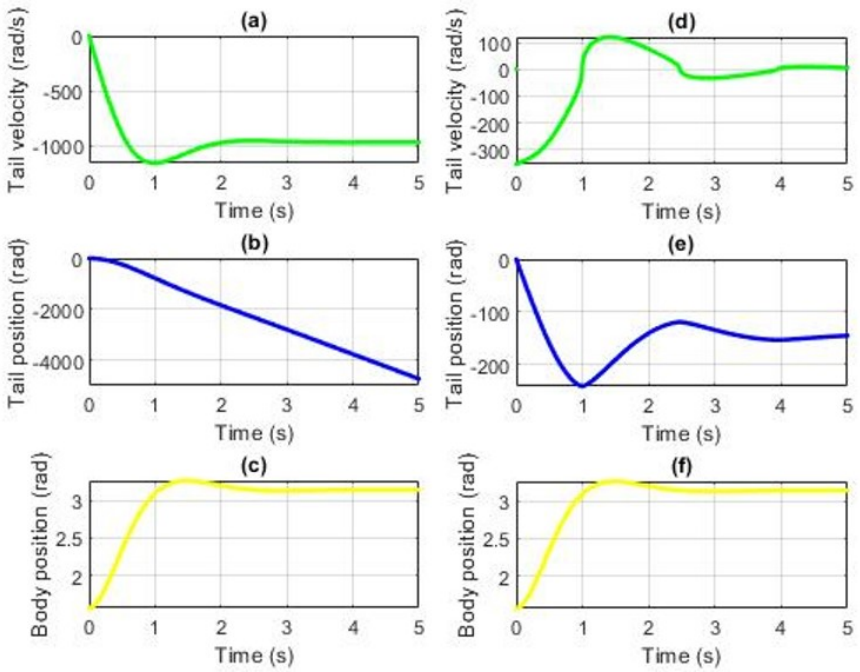

Figure 3.6: Results from the example tests (RW tail on the left and AeroTail on the right): (a) & (d) The velocity of the tail reaches a constant as the system converges. (b) & (e) The position of the tail versus time. (c) & (f) The body angle reaches the target up-right position (π).

Example test

An example test is conducted to demonstrate the characteristics of the tails' performances. The robot (using the previous dynamic model and control method in Section 3.1) needs to be balanced to an upright position from a 90° tilt within 3 seconds; the mass of the body is 20 grams, the RW tail is 10 grams, and the AeroTail is mass-less. The gains for the PD control are also determined in the example test. An additional requirement stipulates that there should only be one positive and one negative overshoot for the body position before convergence, with an error allowance of 1° plus or minus. The results of the example test are shown in Fig. 3.6. The tail's peak velocity is 355 rad/s with a net energy consumption of 4.05 J. The body positions of both tails follow identical trajectories as expected, and the RW tail experiences significantly more rotations than its counterpart. The tail velocity in (d) appears to be as smooth as other graphs because it is solely dependent on the motor torque and there is no acceleration process when the motor torque changes; it also converges to zero after the motor torque does with some delay.

Following the example tests, specific metric comparisons with controlled variables will be conducted. Four tests in total will be performed, and the controller gains will remain constant throughout all of them.

Test 1

The first test compares the peak motor output torque of both mechanisms with different robot body mass (m_3). Fig. 3.7 (a) displays the change in peak motor torques as the robot body mass increases from 20 g to 70 g. The peak torques of both the RW tail and AeroTail rise linearly, with the RW tail's graph generally higher and exhibiting a steeper slope than the AeroTail's. To maintain constant peak velocity, the RW mass must increase with the body mass; thus, as the body mass increases, the peak torque of the RW tail grows faster than that of the AeroTail. On average, AeroTail can achieve a 33.2% reduction of peak torque input. This test demonstrates that the AeroTail offers an advantage in terms of motor torque output requirements and the potential to reduce the robot's total mass.

Test 2

The second test compares the peak motor velocities of both tails with varying correction angles (angles required for righting from the initial to the target position). As shown in Fig. 3.7 (b), the AeroTail's peak velocity remains relatively stable within the 200 to 400 rad/s range as the correction angle increases, whereas the RW tail's peak velocity triples. The AeroTail's ability to reach an ultimate velocity when exerting torque causes its peak velocity to fluctuate less when the correction angles differ significantly. This test indicates that the AeroTail has a lower requirement for peak motor velocity, consistently lower than that of the RW tail; particularly at a correction angle of 120°, for which the AeroTail manage to achieve a peak velocity reduction of 72.8%.

Test 3

The third test compares the energy consumption of both mechanisms with varying tail masses (for the RW) as a percentage of the robot's body mass. The AeroTail's graph in Fig. 3.7 (c) is included for comparison purposes only, as it does not have mass. The AeroTail's energy consumption remains constant at 7.42 J under initial conditions (identical to the example tests), while the RW tail's energy consumption dramatically decreases as the tail mass increases from 20% to 80% of the body, intersecting the AeroTail's graph at 60%. This test reveals that the RW tail can outperform the AeroTail in some metrics even with the mass disadvantage. However, to match the AeroTail's performance, the RW tail mass must constitute 60% of the body, which is impractical if the robot needs to perform functions other than balancing.

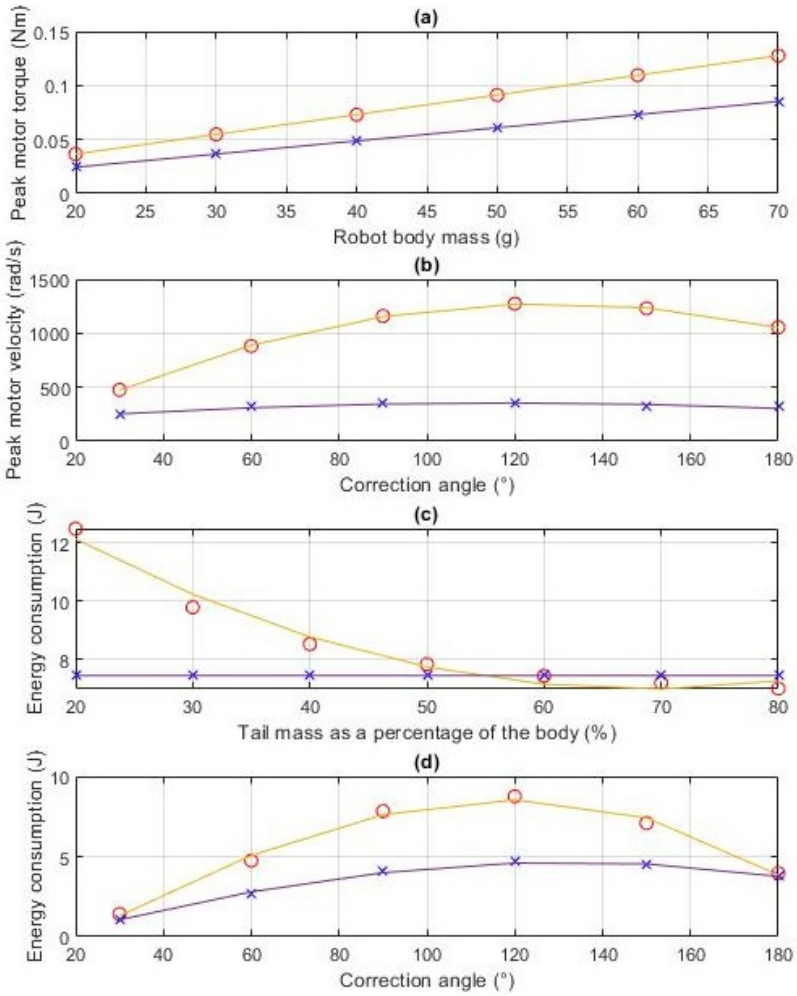

Figure 3.7: The results from the 4 simulation studies: (a) Peak motor output torque versus robot body mass of RW tail and AeroTail (purple); (b) Peak velocity versus correction angle of both tails. (c) Energy consumption versus tail masses of the tails as percentages of the robot. (d) Energy consumption versus correction angles of the tails.

Test 4

The fourth test compares the energy consumption of both tails with different correction angles. In Fig. 3.7 (d), the AeroTail's graph is closer to that of the RW tail, with a less pronounced curvature, resembling the results of Test 2. This indicates that the RW tail's energy consumption is more susceptible to changes in correction angles, leading to the shapes of the graphs: the outcomes for the tails are similar at very small and very large correction angles but increasingly divergent in the middle range. As with Test 2, the difference in energy consumption of the tails is greatest at a correction angle of 120°. For most angles, the AeroTail consumes less energy to balance, rendering it superior in this metric.

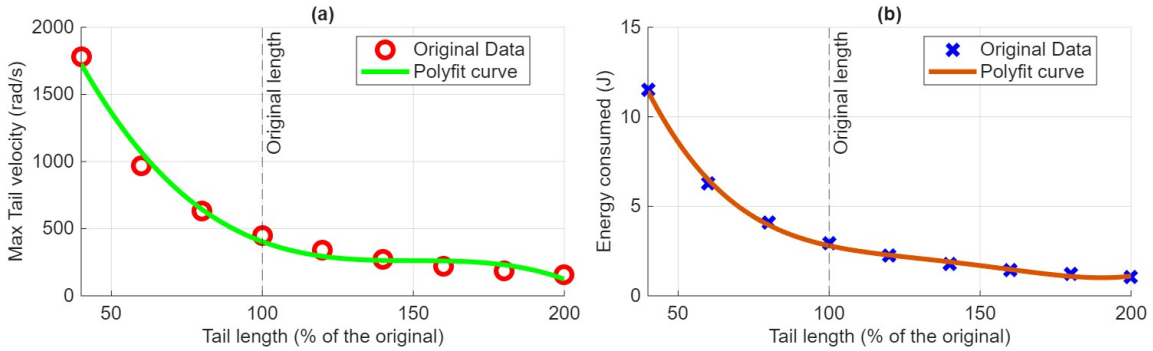

Figure 3.8: AeroTail length sensitivity study: (a) Peak motor velocity required, and (b) Energy consumption versus tail length scaling.

3.2.3 AeroTail length sensitivity study

We have established in previous sections (Equation (3.13)) that the aerodynamic drag generated is a cubic function of the half length of the AeroTail assuming the drag concentrates on its ends. This means the torque generating capability and balancing performance of AeroTail is highly sensitive to its length. This study examine the effects of scaling the AeroTail's length on the required peak motor velocity and energy consumption. The simulation setup copies that of the example test in the previous section, namely, balancing the inverted pendulum from a horizontal to a upright position. In this case, the controlled variables are initial body angle, mass, convergence criteria, and controller gains. Therefore, the torque pattern and convergence time scale are constant throughout the study and the performance is only judged according to required peak motor velocity and energy consumption. The tail half length (l_2) is scaled from 40% to 200% of the original (5cm) with an interval of 20%, and the results can be found in Fig. 3.8. As we can see, both peak velocity and energy consumed drop drastically as the tail length increases. To visualise the trends of result data points, best fitting curves (cubic) are added to the figures using the POLYFIT function in MATLAB. It can be deducted from the results that using longer AeroTails dramatically reduces both the peak required motor velocity and energy consumed to achieve the same task. Therefore, maximising the length of the AeroTail with constraints applied should be used as a general strategy for mechanical design in the next chapter.

3.3 Chapter summary

This chapter introduced the AeroTail, a robotic tail device design capable of self-righting and balancing on a point-in-plane aerodynamically. The tail mechanism's dynamic model is based on the classic IP with additional aerodynamic features, and

a suitable control method for such a device was chosen accordingly. Computational simulations using MATLAB visualised and quantified the behaviour of the tails with both aerodynamic and inertial effects under various conditions and scenarios. Comparative studies with controlled variables were conducted to evaluate their performances, illustrating their respective advantages and limitations. The most significant advantage of the AeroTail over the RW tail is its lack of mass, allowing it to maintain a low increase in peak motor torque output as the robot body mass increases. Conversely, the RW tail experiences dramatically high energy consumption with a low tail-to-body mass ratio, while the AeroTail does not require mass to function. In terms of both peak motor velocity and energy consumption, the AeroTail outperforms the RW tail when the correction angle is between the horizontal and 140°, with the differences in results peaking at 120°. However, the RW tail has a relative advantage at very small correction angles or near the vertically hanging position.

This chapter only introduced the theoretical concept and initial simulation of the AeroTail balancer; more details on the mechanical design of the AeroTail, especially of the drag-inducing devices on the ends of the tail body, are yet to be decided. Furthermore, experimental validation is needed to prove that this concept is indeed functional in a realistic scenario. Therefore, in the next chapter, a thorough optimisation study for the drag-inducers is introduced, and experiments are conducted to test the real-world performance of the AeroTail.

Chapter 4

Optimisation Study of the Drag-Inducers

This chapter presents a comprehensive study on optimising the DI design for the AeroTail to maximise its aerodynamic torque for robotic balancing; it demonstrates a specialised Computational Fluid Dynamics (CFD) simulations on a selection of shapes to explore how specific geometrical features influence aerodynamic drag, with detailed explanations of the observed effects; and it introduces an optimisation framework to identify the optimal frame design that maximises aerodynamic drag, while adhering to predefined constraints such as weight and dimensional limits. Finally, the chapter includes the implementation of practical experiments using the AeroTail test platform, equipped with the optimised DI designs, to assess their real-world performance on a rotational tail mechanism with variable wind speeds along its length. This involves a comparative analysis of the experimental findings against the CFD simulation results and the establishment of an analytical approach for quantifying the performance variation among different DI models.

4.1 Methodology for drag-inducer design

The primary objective in designing the DI is to achieve a balance between minimising weight and maximising the generated drag force. The first half of the objective can be simplified to finding the minimum material use for the application and then optimising the distribution; such that a fixed available weight for the material is maintained during the design process. In order to find the optimal DI design, two distinctive steps need to be taken; firstly, the theoretical best shape to generate aerodynamic drag is to be found through CFD simulation since there is insufficient related conclusions in previous studies; secondly, using this general shape, the optimal DI design for maximising torque generated aerodynamically can be calculated using

a optimisation problem.

For the first step, there are initial assumptions needed to be made for the simulation setup. From (2.1), it can be concluded that there are two strategies of maximising drag; one is to maximise the frontal area (A), and the other is doing that for the drag coefficient (C_d). However, these two methods cannot be examined separately because both A and C_d affect drag proportionally. An important finding from previous studies is that cup-like concave shapes yield better drag coefficients than their convex or flat counterparts [96, 98]. To make the geometry of the shapes in question easily describable, we define a concave shape to be that with an 2 dimensional "opening" surrounded by a rim and the rest of the body extending into the third dimension. If such shape is to be used to generate drag thus bearing load, it is usually structurally sound to only have rigid material in the rim to form a "frame" while the rest of the shape can be made from less strong or even soft film-like materials, forming the "film". In this setup, the effective area (A) is determined by the size of the frame's opening, while the specific shape of the film can significantly impact the drag coefficient (C_d). Additionally, the mass is primarily influenced by the frame material, as the film can be made from lightweight materials, thereby reducing the overall device mass. This 'frame-film' setup enables us to explore drag-maximising strategies without introducing too many uncontrolled variables.

Even though a formulated optimisation problem is not necessary, there are some constraints to act as the controlled variables in the simulation studies. As mentioned before, the available mass for the frame must be a given and fixed value according to the condition of the overall device. For the simplicity of the study, the frame is envisaged as an extruded, cage-like structure with a uniform cross-section. The available length for the frame l can be calculated using the following equation assuming the material has uniform and constant density:

$$l = \frac{m_0 N}{a_0 \rho}, \tag{4.1}$$

where m_0 is the total mass of the balancing mechanism, N is a design factor which determines the percentage of the mass that can be used on frame, a_0 is the area of the cross-section and ρ is the density of the material used.

When conducting a study about maximising drag with A and C_d being the subjects, it is only logical to set ρ and v as constants according to (2.1). In this case, because ρ is simply the density of air, is it assumed to be constant; flow speed v, however, must be a value calculated from the torque required (τ_r) for the device to complete a specific task. Assuming the drag acts on a single point, the aerodynamic torque can be simply calculated as $\tau_r = Dl_0$ where l_0 is the lever arm. Therefore, the

flow speed can be expressed using this equation:

$$v = \sqrt{\frac{2|\tau_r|}{\rho C_d A l_0}} \; for \; v > 0, \tag{4.2}$$

in which v is the flow speed needed to aerodynamically produce the required torque τ_r.

In Section 4.2, the CFD simulation study will be conducted according to the aforementioned methodology for undergoing the first step. In the simulation study, specific values from AeroTail-based scenarios are used in (4.1) and (4.2) to obtain the constant setup for the simulation environment. As for the second step, an optimisation problem shall be setup according to the observations from the simulation. The optimisation problem aims to directly or indirectly maximise the aerodynamic drag that could be generated by the DI in a given scenario. The results from the optimisation problem can be one or several DI shape with mathematically definable parameters and they will undergo further examination until the best option is chosen. The details of this step are presented in Section 4.3.

4.2 CFD Simulation Study

4.2.1 CFD Simulation Setup

Even though the main purpose of the simulation study is to find the general characteristics of a shape that enables it to produce larger aerodynamic drag, the initial conditions and assumptions do need to be based on the AeroTail design [28] in the previous work since it is easier to evaluate the outcome given a scenario with fitting application. The estimated mass of the AeroTail is approximately 5 g, and it is targeted that each DI's opening frame should not exceed 10% of this total mass. The frame is assumed to be made from Tough 2000 Resin, a widely used material for 3D printing (which is later on used for the DI prototype in the Section 4.4) with a density of 1.11 g/cm^3. The frame is set to have a cross-sectional diameter of 2 mm (and its area is 3.14 mm^2) which is the smallest value possible for the structure to stay integral during manufacturing and under load judging from past experience with the material. Substituting $m_0 = 5g$, $N = 0.1$, $a_0 = 3.14$ mm^2, and $\rho = 1.11$ g/cm^3 into (4.1), the maximum permissible frame length is calculated to be 14.3 cm. Consequently, a total usable frame length of 12 cm is selected for its mathematical convenience.

The initial stage of the simulation study focuses on shapes subjected to an opening circumference constraint of 12 cm, which is the available frame length, since it is

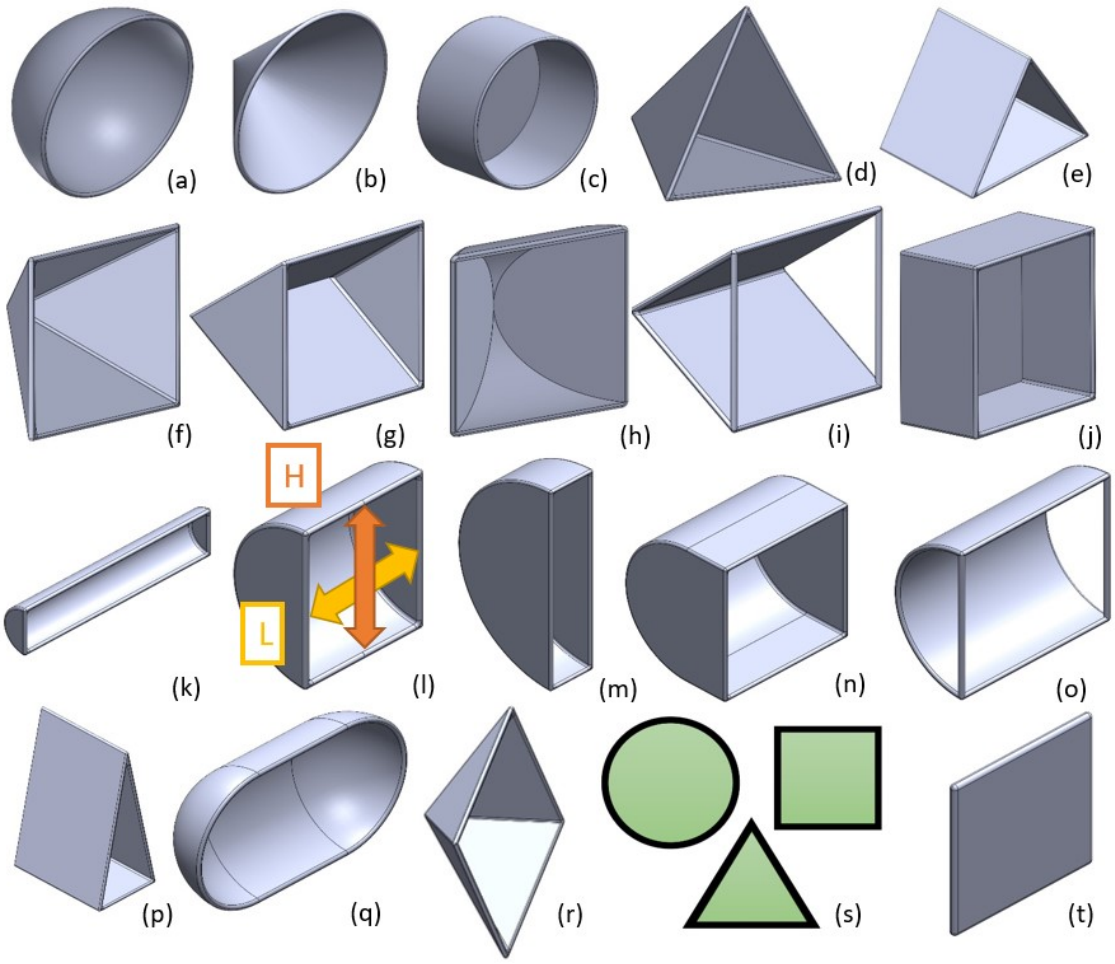

Figure 4.1: (a)-(r) depict all the shapes involved in the initial phase of the CFD study. (s) illustrates the frontal view of these shapes, with the effective area marked in green and the frame outlined in black. (t) is a flat rectangular shape that has accurate wind tunnel data which can be used for result validation. A specific comparison for the Semi-cylinders shown in (l) is conducted, focusing on the height-to-length ratio (H/L), which varies while maintaining the overall configuration, thereby altering the shape's slenderness or fullness.

Table 4.1: Simulation set-ups

Setups	Specification
Element type	Unstructured
Element size	10 mm
Maximum element size	20 mm
Boundary walls	150 mm × 150 mm
Inlet/Outlet	100 mm / 200 mm
Boundary wall condition	No-slip
Time step	Auto-generated
Turbulence model	k-ϵ
Convergence criteria	Specified iteration

postulated that the frame structure is continuous and confined to the rim of the opening. Regular shapes are categorised based on the number of edges, and the most logical and intuitive film shapes are conceptualised for each (as depicted in Fig. 4.1). These shapes are modelled as solid shells with a consistent thickness of 1 mm. The setup specifications can be found in Table 4.1. The mesh's automatic grain size is set to 10 mm (with a maximum of 20 mm). The mesh around the shape's walls was refined to capture complex geometric features accurately. The grain sizes are obtained through a convergence test as part of the mesh independence study. The boundary walls were placed 150 mm away from the shape, with the inlet positioned 100 mm in front and the outlet 200 mm behind the shape forming a typical rectangular cuboidal mesh. These distances were established through a sensitivity analysis. The boundary walls have a no-slip condition while the inlet has a set flow velocity. In order to choose an appropriate flow speed for the simulation, we assume the drag-induced torque of 0.0111 Nm, which is the torque sufficient to reorient a 23 g device from a 30° angle to a vertical position using a DI with a frontal area of 5 cm^2. A Semi-sphere shaped DI is selected as the benchmark, as its drag coefficient data is supported by plenty of existing wind tunnel tests. Substituting $\tau_r = 0.0111$ Nm, $A = 5$ cm^2, $C_d = 1.43$ (for semi-sphere) and $l_0 = 10$ cm (the lever arm for AeroTail) into (4.2), the flow speed required for the task is calculated to be 16 m/s. We utilised the k-ϵ turbulence model for its robustness and suitability and the simulation stops after a set number of iterations to ensure steady-state solution.

4.2.2 CFD Study Results

The outcomes of the CFD simulation study are collated in Table 4.2, with the shapes named according to their corresponding letter markings in Fig. 4.1. Given the opening circumference constraint, there is a significant variance in the effective areas of

Table 4.2: Overview and Results of Initial CFD Simulation for Various Shapes

Shapes	Area (cm^2)	Force (N)	C_d	C_d*	Sources
(a) Semi-sphere	11.46	0.257	1.43	1.42 1.40	[98] [118]
(b) Cone	11.46	0.244	1.36	2.10	[98], [119]
(c) Hollow cylinder	11.46	0.237	1.32	-	
(d) Tetrahedron	6.93	0.147	1.35	-	
(e) Triangle-prism	6.93	0.120	1.10	-	
(f) Pyramid	9.00	0.190	1.34	(i)	
(g) Angled hollow cube	9.00	0.191	1.36	(i)	
(h) The "hat"	9.00	0.198	1.40	-	
(i) The "book"	9.00	0.190	1.34	2.20	[96]
(j) Hollow cube	9.00	0.183	1.30	2.05	[98], [119]
(k) Semi-cylinder shallow	8.00	0.175	1.40	2.30	[96], [118]
(l) Semi-cylinder	9.00	0.195	1.39	(k)	
(m) Semi-cylinder deep	8.00	0.171	1.36	(k)	
(n) Elongated cylinder	9.00	0.193	1.34	(k)	
(o) Open Semi-cylinder	9.00	0.188	1.33	(k)	
(p) Long triangle	4.90	0.095	1.24	-	
(q) Capsule	10.2	0.230	1.44	(a)	
(r) Rhombus	7.79	0.164	1.34	-	
(t) Plank	4.00	0.076	1.23	1.17 1.20	[96] [120]

* This column presents experimental data from previous sources. If a single value with multiple sources is listed for a shape, the sources concur on this value. When the C_d refers to a different shape, it implies that the shapes are sufficiently similar, differing only in their dimensions.

Table 4.3: CFD results for the Semi-cylinders

H/L (cm)	Area (cm^2)	Force (N)	C_d
2.0/4.0	8.00	0.175	1.400
2.4/3.6	8.36	0.188	1.390
2.7/3.3	8.91	0.193	1.384
2.9/3.1	8.99	0.195	1.382
3.0/3.0	9.00	0.194	1.370

these shapes. Both the drag force and drag coefficient values are computed by the simulation software. Analysis of these results reveals several insights. Predominantly, shapes with a larger effective area tend to generate greater drag, as the drag force is directly proportional to this area. However, the drag coefficients of these shapes exhibit relative unpredictability, fluctuating between 1.1 and 1.5, while effective areas may differ markedly. Therefore, optimising the effective area is crucial in identifying the shape capable of producing the highest drag. When comparing shapes (a) and (q), (e) and (p), or (k) and (l), it is evident that shapes with a slimmer frontal profile generally yield higher C_d values. Moreover, shapes with closed ends typically exhibit larger C_d than their open-ended counterparts, as seen in comparisons between (l) and (o), or (g) and (i). Additionally, an analysis of (a) versus (c) and (h) versus (j) indicates that arch-shaped profiles usually generate the highest C_d for a given frontal shape.

The final column of Table 4.2 presents wind tunnel test data from previous studies. The simulation conditions for the semi-sphere (a) and plank (t) closely match those of the wind tunnel tests, leading to comparable C_d outcomes, thereby affirming the simulated results' reliability. However, the remaining shapes display considerably different C_d values. This discrepancy arises because the simulation setup, which more accurately reflects practical scenarios with shapes not in contact with boundary walls, differs from the wind tunnel setup (as outlined in Section 2.2.2). This difference confirms that the shapes under consideration vary significantly from the 2D "prism" shapes in previous studies, whose C_d values are not directly applicable for practical calculations.

Examining the Semi-cylinders with varying width-to-length ratios allows for a more distinct understanding of the impact of both area and drag coefficient on drag force. Fig. 4.1 (l) and Table 4.3 provide a comparative analysis of five Semi-cylinders, each sharing the same opening circumference but differing in width-to-length ratios, and consequently, in effective areas. The data indicates that as the shapes become more slender, their frontal area diminishes, yet there is a consistent trend of increasing drag coefficients. A H/L ratio of 2.9/3.1 yields the highest drag force, as the benefits

of a higher C_d outweigh the drawbacks of a smaller area. However, as the shape becomes increasingly slender, the diminishing frontal area begins to adversely affect the drag force, leading to a reduction in overall drag.

To summarise the previous paragraphs, the findings can be organised into these main points:

- Shapes with a larger effective area tend to generate greater drag while the drag coefficients of these shapes exhibit relative unpredictability.
- Shapes with slimmer frontal profiles, closed ends, and arch-shaped side profiles generally yield higher C_d values.
- The C_d values of 2D "prism" shapes in previous studies are not directly applicable for practical calculations.

The variation in drag coefficients among different shapes can be attributed to the phenomena of flow separation and vortex formation. For instance, comparing shapes (a) and (e), their streamline images from the simulation, depicted in Fig. 4.2, reveal notable differences. The extended blue (low velocity) area behind shape (a) compared to (e) suggests longer flow separation, which in turn leads to the formation of vortices, observable as circular vectors around and behind the shapes. Larger and more intense vortices are generally indicative of higher drag [121, 122], corroborating the higher drag coefficient observed for shape (a). Additionally, the shape's wind-capturing capability plays a vital role, as these vortices originate from air pressure disparities at the shape's edges [123]. This elucidates why arch-shaped profiles and shapes with closed ends exhibit higher C_d: they effectively create higher air pressure in the pocket regions, resulting in a larger pressure differential with the surrounding airflow.

4.3 Optimal Frame Design

4.3.1 Methodology of Frame Design

In previous designs discussed in Section 2.2.2, the DI frame was limited to 'closed' structures. However, if the primary constraint is the total frame length and the goal is to maximise effective area, a closed design can be inefficient. Our approach considers these limitations to develop a more material-efficient frame design. An alternative approach involves using segmented frames on the rim, each segment connected to the frame's centre by a "rib", as illustrated in Fig. 4.3. This design is feasible as the film material does not require support along its entire edge; supporting it in sections is sufficient for structural stability. In this configuration, n represents the number of

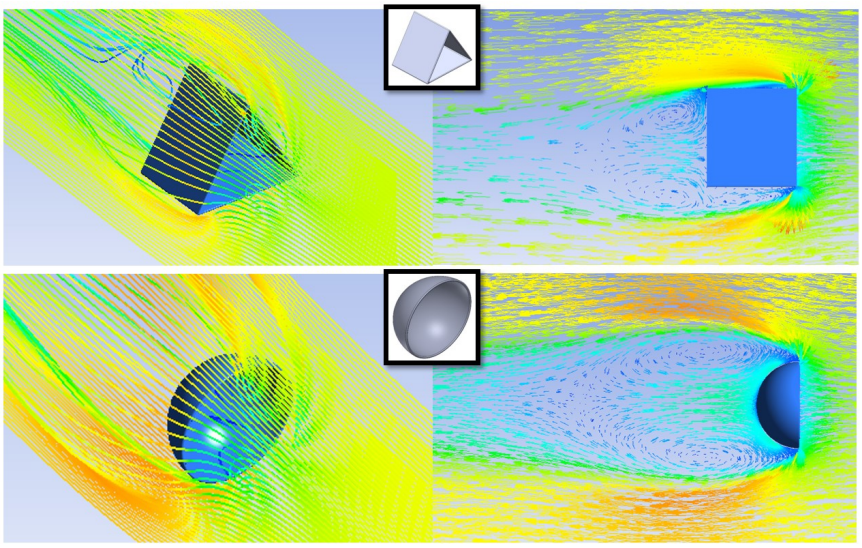

Figure 4.2: The CFD simulation's streamline (left) and vector (right) images. The colour represents flow velocity with red denoting high and blue low velocities, indicated by the colour bar on the right. At the top is the Triangle-prism (e), and at the bottom, the Semi-sphere (a).

ribs in a polygonal frame, a is the length of a rib, and b is the length of a rim segment to which the film is attached. As the "T" shapes are evenly spaced, the effective area typically forms regular polygons.

The area of such a polygon is given by the equation:

$$\begin{aligned} A =& n(A_1 + 2A_2 - 2A_3) \\ =& n(\cos(\frac{\pi}{n})a \cdot \sin(\frac{\pi}{n})a + 2\sin(\frac{\pi}{n})a \cdot \sin(\frac{\pi}{n})(\frac{b}{2}) \\ & - \cos(\frac{\pi}{n})(\frac{b}{2}) \cdot \sin(\frac{\pi}{n})(\frac{b}{2})) \\ =& n(\frac{1}{2}\sin(\frac{2\pi}{n})(a^2 - \frac{b^2}{4}) + 2\sin^2(\frac{\pi}{n})(a \cdot \frac{b}{2})), \end{aligned} \tag{4.3}$$

where A is the effective area. The variables n, a and b are interconnected as follows:

$$a = \frac{l}{n} - b, \tag{4.4}$$

where l is the total available length of the frame (12 cm in this study). Consequently, Equation (4.3) can be reformulated as a function of n and b, with l as a constant:

$$\begin{aligned} A(n,b) =& n(\frac{1}{2}\sin(\frac{2\pi}{n})(\frac{3}{4}b^2 - \frac{2l}{n}b + \frac{l^2}{n^2}) \\ & + \sin^2(\frac{\pi}{n})(\frac{l}{n}b - b^2)). \end{aligned} \tag{4.5}$$

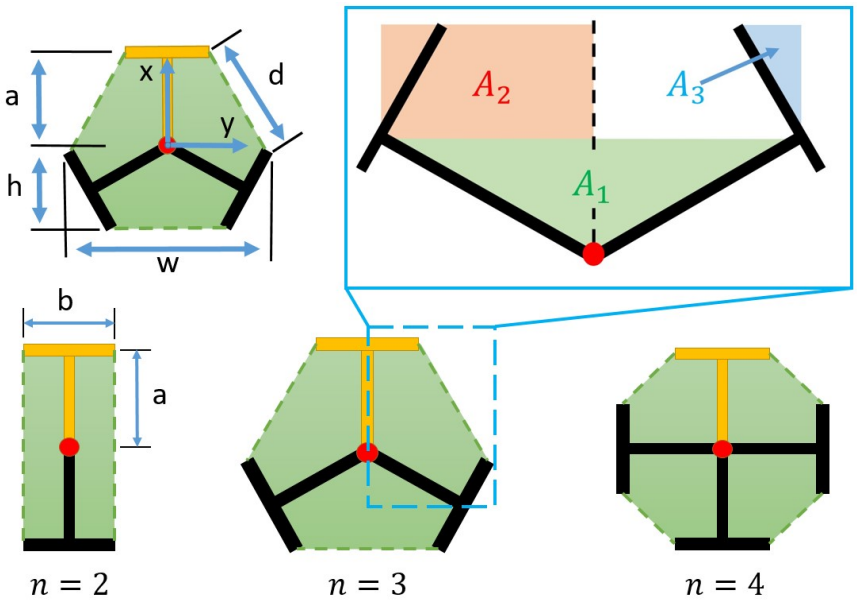

Figure 4.3: The structures of segmented frames with varying numbers of ribs. Each "T" shape, comprising a rim segment and a rib, extends outward from the centre (indicated by a red dot) to form a carousel configuration. The unsupported film edges are represented by dotted lines, and the effective area is highlighted in green.

In the top-left corner of Fig. 4.3, three additional parameters, w, h, and d, are defined. These will serve as constraints in the optimisation problem. A coordinate system is placed at the frame's centre (red dot), with the x-axis aligned with one of the "T" shapes (in yellow) and the y-axis perpendicular to it. h is defined as the length of the frame in the x-direction from its centre to the opposite end of the yellow "T". w is the frame's width in the y-direction, and d is the distance between the ends of two adjacent rim segments. These parameters can be calculated using the following equations:

$$\begin{aligned} w =& 2\sin(\pi - \frac{2\pi}{n})a + \cos(\pi - \frac{2\pi}{n})b \\ h =& \cos(\pi - \frac{2\pi}{n})a + \frac{1}{2}\sin(\pi - \frac{2\pi}{n})b \\ d =& 2\sin(\frac{\pi}{n})a - \cos(\frac{\pi}{n})b. \end{aligned} \tag{4.6}$$

4.3.2 Optimisation

For simplistic structures, the design optimisation can be approached by a step-based qualitative method [124]; however, since the properties of the frame have being quantified, a classic constrained optimisation problem (inspired by [125]) is setup for the frame design. The aim of the optimisation problem is to identify the optimal values

for n and b that maximise A, the effective area:

$$\begin{aligned} \max_{n,b} \quad & A(n,b) \\ \text{s.t.} \quad & 2 \leq n, n \subset \mathbb{Z} \\ & 0.2 \leq b \\ & w \leq 5, d > 0 \\ & \frac{l}{n} - b + h \leq 5 \end{aligned} \tag{4.7}$$

where $A(n,b)$ is defined in Equation (4.5). Both n and b are subject to specific constraints, and additional constraints are imposed by the parameters w, h, and d. The minimum value for n is set at 2, as having fewer than two ribs does not provide a structurally stable support for the film. Furthermore, n must always be an integer. The lower bound for b is established at 0.2 cm, to ensure that the length of a single rim segment exceeds the frame's cross-sectional thickness. The frame's width w is constrained by the prototype platform, limited to a maximum of 5 cm. Similarly, the sum of a and h cannot exceed 5 cm due to the physical limitations of the prototype (as indicated in the last line of (4.7)). Lastly, to avoid the rim segments intersecting or overlapping, the distance d between their tips must always be greater than zero.

The optimisation problem is solved using the "fmincon" function in MATLAB. The results indicate that the optimal value for n is 2, with a corresponding b of 3.50 cm, yielding a maximum area of 17.5 cm^2. Although this result is definitive, outcomes for n values of 3, 4, and 5 are also documented in Table 4.4 for additional analysis. Notably, when the frame has five ribs, b reaches its lower bound, rendering any further increase in n impractical. It is important to recognise that while the effective area is a primary factor influencing aerodynamic drag, the drag coefficient also plays a significant role. In the case of the two-rib "I" shape frame, different configurations of the resultant film shape can lead to substantially different drag coefficients. Therefore, further CFD simulations are essential to validate the superiority of the optimised frame designs over those proposed in Section 4.2.1 and to facilitate a comparative analysis of the CFD results from Section 4.2.2 with those of the optimised shapes.

4.3.3 Further CFD Simulation Study

The CFD study encompasses five configurations, as shown in Fig. 4.4, each corresponding to the optimisation results listed in Table 4.4, with two scenarios for $n = 2$. The film shapes for these frames are designed in line with the principle of maximising drag given the specific frame structure. Therefore, they are fashioned with arch-shaped profiles and closed ends, aligning with the findings from Section 4.2.2.

Table 4.4: The parameter optimisation results. The drag force and drag coefficient of each shape are obtained from further CFD simulations.

Shapes	n	b (cm)	A (cm^2)	Drag (N)	C_d
(a)	2	3.50	17.50	0.403	1.47
(b)	2	3.50	17.50	0.394	1.44
(c)	3	1.55	15.57	0.323	1.32
(d)	4	0.50	14.88	0.327	1.40
(e)	5	0.20	12.24	0.267	1.39

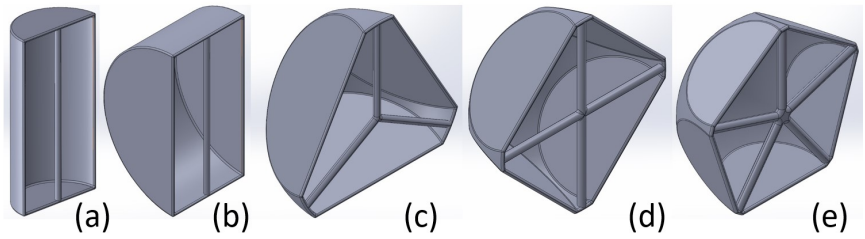

Figure 4.4: The shapes utilised in the CFD studies, inclusive of both the frames and the film behind them. The sizes are not to scale but are presented to illustrate the structural configurations. (a) Configuration 1 for $n = 2$, with arches on the shorter edges; (b) Configuration 2 for $n = 2$, with arches on the longer edges; (c) for $n = 3$; (d) for $n = 4$; and (e) for $n = 5$.

The conditions applied to these CFD simulations are consistent with the first stage outlined in Section 4.2.1.

The results indicate that configuration (a) produces a drag force of 0.403 N, marginally surpassing the 0.394 N of configuration (b), despite both having identical effective areas. This difference stems from the higher drag coefficient observed when arches are positioned on the shorter edges. As n increases, there is a noticeable trend of diminishing drag force, with variations in drag coefficients. An exception is observed with shape (d), which, despite a smaller frontal area than (c), generates a higher drag force due to its substantially greater drag coefficient. Consequently, the most effective design for maximising aerodynamic drag is configuration (a), the "I" frame closed semi-cylinder with the rim segment forming the arch diameter. An additional advantage of (a) is its longer rim segment compared to other configurations, which facilitates easier and more secure attachment of the film.

4.4 Experiments

The simulation studies in Section 4.3.3 offered insights into the aerodynamic drag of various DI designs under uniform wind conditions. Building on these findings, we conducted experiments to validate the theoretical predictions in a practical setting.

4.4.1 Experiment Setup

The experiments are carried out using an existing AeroTail testing platform, designed to simulate a legged robot with an actuated inverted pendulum. The setup includes two adjustable restrictors on the sides, positioned on a T-slot frame segment that also serves as a rail for all components. The actuator is a 3-phase Brushless DC (BLDC) motor, managed by a standard Electronic Speed Controller (ESC). A magnetic encoder attached to the motor allows for accurate measurement of rotation speed.

The AeroTails tested are 3D-printed single units, featuring DI frames at their ends. The central mount of each tail is compatible with the motor on the testing platform. The films for the DIs are crafted from heat shrink polyvinyl chloride bags, shaped using 3D printed moulds, as illustrated in Fig. 4.5. The various DI versions, as shown in Fig. 4.6, are named according to their corresponding shapes in Fig. 4.4. The numbering after the dot in each name indicates the connection style, with "1" denoting the tail body situated between the "T" shapes and "2" indicating the tail body positioned directly atop them.

The following assumptions are adopted for the aerodynamic modelling and testing conditions used in this study:

- The drag coefficient C_d of each drag-inducing (DI) configuration is treated as constant during each test condition, based on CFD and experimental calibration.
- The target tail rotational speed during testing is approximately 150 rad/s, representing the nominal operating condition used for performance comparison.
- The Reynolds number setting for CFD study in previous sections are automatically calculated by ANSYS using air density and viscosity (at sea level), characteristic length, and local relative airspeed. These parameters will stay consistent for any calculations done in this section.
- Due to rotational motion of the tail, the local airspeed along the DI span is non-uniform, increasing approximately linearly with radial distance from the rotation axis.

Experiment 1

In the first experiment, the objective is to measure the torques generated by different versions of the DI while the device body remains stationary. As you can see in Fig. 4.7, a weight is suspended from the end of the pendulum (aligned with the tail's centre) and placed on a scale. The spring is tensioned, and its linear behaviour implies

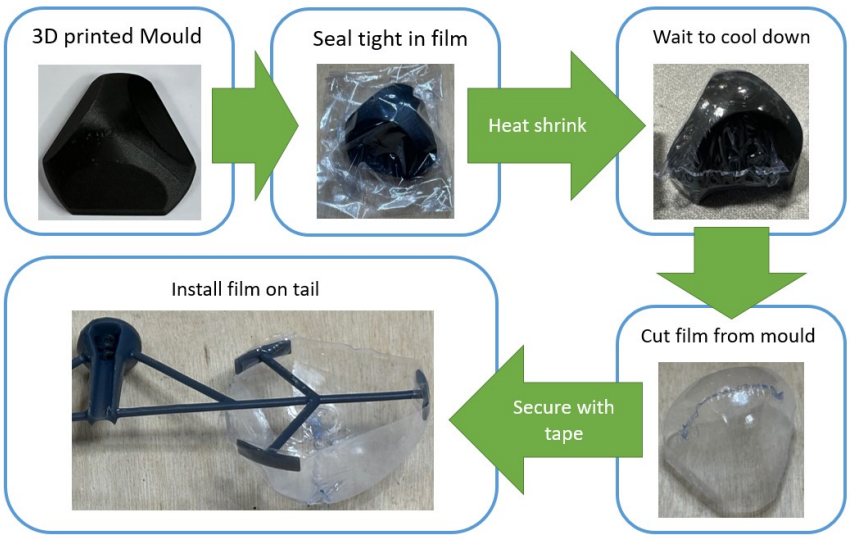

Figure 4.5: The manufacturing process involves several stages: enclosing the 3D printed mould within the film bag, applying heat using a heat gun; once cooled, the shaped film is cut from the mould; and finally, the film is secured onto the tail frame with adhesive tape.

that an upward force, or torque generated by the tail, will reduce the reading on the scale. The pendulum is fixed at a 30° angle, achieved by adjusting the restrictors' height and spacing. For each DI, a specific throttle input is determined to achieve an angular velocity of 150 rad/s for the tail. The torques generated by each DI version at this constant speed are then measured using the previously mentioned method.

Experiment 2

The second experiment aims to assess the balancing capability of the pendulum equipped with various DIs, starting from a predefined angle to an upright position. As illustrated in Fig. 4.8, the pendulum begins at an angle θ and is halted in the upright position by the restrictor. Throughout this process, the tail's angular velocity is maintained at a constant 150 rad/s, identical to Experiment 1. The angle θ is varied incrementally from lower to higher values to determine the maximum angle from which each DI can successfully balance the pendulum.

4.4.2 Experiment Results

Experiment 1

The experimental results for torques align with the trends observed in the simulation study (see Video 1). There is a consistent decrease in drag torque from DI (a) to (e), with (d) being the only exception, as seen in the simulations. DIs (a) and (b) share

Figure 4.6: The top of the figure shows an AeroTail prototype, detailing all its components. Below are the various DI versions. Red tape is applied to the sides of each DI for enhanced visibility during experiments.

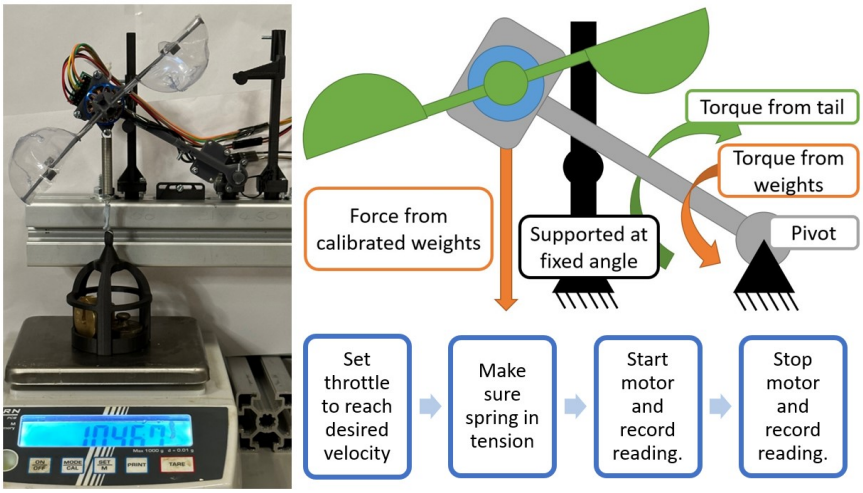

Figure 4.7: The figure on the left illustrates the overall setup for Experiment 1. At the top, a simplified diagram explains the experiment's internal logic, and the procedure is depicted below it.

the same frame structure but differ in the orientation of the arch on the film. The simulation concluded that (b) has a lower drag coefficient than (a), thus generating less drag with the same effective area. This is corroborated by the experimental results, with a more pronounced difference than in the simulation. Additionally, the way the DI is connected to the tail (connection style) significantly impacts torque performance. Across all DI versions, style 2 consistently produces better torque results than style 1, with DI a.2 outperforming a.1 by 20.8%, solely due to the difference in connection style. The drag coefficients for each DI version, derived from the experimental data, vary significantly from the simulated results. This discrepancy can be attributed to the non-uniformity of drag coefficients along the length of the DIs, and the assumption that drag force acts at the tail's ends when calculating C_{dE}.

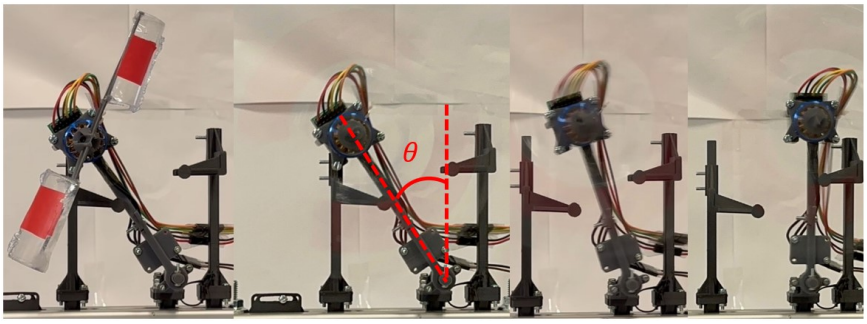

Figure 4.8: The sequence of the balancing process in Experiment 2, depicted from left to right. The pendulum is balanced from an angle θ to the upright position.

Table 4.5: Experiment Results

Version	τ_e (mNm)	C_{dE}	θ	θ_t
a.1	24.98	4.14	32°	31°
a.2	29.82	4.95	38°	38°
b.1	20.56	3.41	27°	25°
b.2	23.02	3.82	30°	28°
c.1	14.78	2.76	16°	18°
c.2	15.46	2.88	17°	19°
d.1	17.25	3.36	18°	21°
d.2	17.93	3.50	20°	22°
e.1	11.72	2.78	14°	14°
e.2	12.49	2.96	15°	15°

Experiment 2

The findings from Experiment 2 largely corroborate those from Experiment 1. As can be seen in Table 4.5 (and Video 1), the experimental results (θ) fit the theoretical value (θ_t) calculated from τ_e with a error of 6% on average. A higher torque generated in a stationary position corresponds to better performance in terms of the maximum angle from which the pendulum can be balanced. Notably, the quantitative differences in DI performance are more pronounced at higher angles and less so near the upright position. This variation is primarily due to the trigonometric nature of the gravitational torques resulting from the device's mass. The purpose of Experiment 2 is to validate the conclusions and insights regarding the torque-generating capabilities of the DIs from a stationary setup in a dynamic pendulum-balancing scenario.

4.5 Comparative analysis

From the results of the experiments came new observations: the numerical difference between the simulation and experimental results cannot be ignored. Torques (τ_s) calculated from simulation results, assuming drag force acts at the tail's ends, are shown in Table 4.6. They differ largely from the experimental results (τ_e in Table 4.5) and the reason behind that was previously assumed in Section 4.4 to be the rotational nature of the tail causing the wind speed to vary along its length. However, this difference was never quantified and thus mathematically proven. If a method could be devised to predict the experimental results given setup conditions, it would serve as the proof that the differences between τ_s and τ_e are indeed caused by the rotational nature of the tail like previously speculated. In this section, such method will be demonstrated and new findings will be explained accordingly.

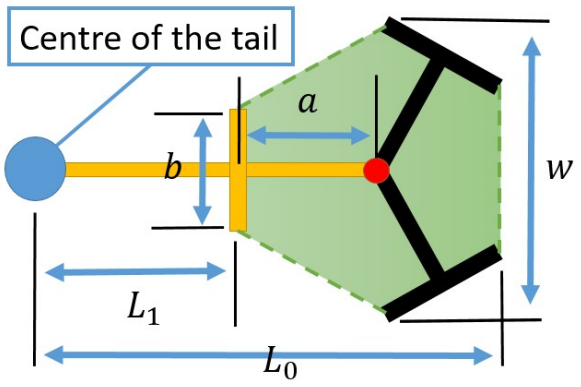

Figure 4.9: Using DI c.2 as an example, an analytical method for calculating torque is derived.

4.5.1 The analytical method

To reconcile the discrepancies between the CFD simulation results and experimental outcomes, an analytical method has been devised. This method calculates the theoretical torque each DI shape can produce, considering the distribution of aerodynamic drag along the DI's surface. This approach accounts for the fact that areas further from the tail's centre contribute more significantly to drag generation, due to both higher wind speeds (as drag force is proportional to the square of wind speed) and longer lever arms for torque production.

For DI c.2, the equation to calculate aerodynamic torque for the AeroTail is given by [97]:

$$\begin{aligned} |\tau_D| &= \int_A Dl\, dA \\ &= \int_{L_1}^{L_0} \frac{1}{2}\rho C_d w(\omega l)^2 l\, dl \end{aligned} \tag{4.8}$$

where D is the drag force, l represents the distance from a point on the DI to the tail's centre, and A is the frontal area. Variables include ρ (air density), C_d (drag coefficient), w (DI width), and ω (tail's angular velocity). L_0 and L_1 are the distances from the tail's centre to the farther and nearer edges of the DI, respectively (as shown in Fig. 4.9). The width of the DI, w, is not constant but varies along the tail's length. Therefore, the equation can be restructured as:

$$|\tau_D| = \frac{1}{2}\rho C_{dE}\omega^2 \int_{L_1}^{L_0} l^3 w(l)\, dl. \tag{4.9}$$

In this experiment, ω is a constant at 150 rad/s. The drag coefficient (C_{dE}) used in the calculations is taken from measured data in Table 4.5. The width function $w(l)$

Table 4.6: Theoretical Torque Results

Version	τ_a (mNm)	τ_s
a.1	28.02	17.71
a.2	37.30	17.71
b.1	23.08	17.31
b.2	28.79	17.31
c.1	17.14	14.19
c.2	17.78	14.19
d.1	19.75	14.37
d.2	20.57	14.37
e.1	12.60	11.73
e.2	12.27	11.73

is expressed using the following equations:

$$w(l) = \begin{cases} 2(l - B_1)\sin(\frac{\pi}{2n}) + b, \ \ for\ B_1 \leq l \leq B_2 \\ 2a\sin(\frac{\pi}{n}) - b\sin(\frac{\pi}{2n}) - 2(l - B_2)\sin(\frac{\pi}{2n}), \\ \qquad\qquad\qquad\qquad\qquad for\ B_2 < l \leq B_3 \end{cases} \tag{4.10}$$

where n is the number of "T" shapes, with $n = 3$ in this case. $B1$, $B2$, and $B3$ define the ranges of l where the width expressions vary. They are determined by:

$$\begin{aligned} B_1 &= 5 - a \\ B_2 &= 5 + a\cos(\frac{\pi}{n}) - \frac{b}{2}\cos(\frac{\pi}{2n}) \\ B_3 &= 5 + a\cos(\frac{\pi}{n}) + \frac{b}{2}\cos(\frac{\pi}{2n}). \end{aligned} \tag{4.11}$$

By integrating (4.10) and (4.11), the width equation for the DI is simplified as:

$$w(l) = \begin{cases} 1.155l - 1.395, & 2.550 \leq l \leq 5.554 \\ 11.43 - 1.155l, & 5.554 < l \leq 6.896 \end{cases}, \tag{4.12}$$

in which the units are cm. Substituting (4.12) into (4.9), the theoretical torque produced by DI c.2 is calculated as 17.78 mNm. Each DI version has a unique expression for $w(l)$, but for brevity, only the full equations for c.2 are shown here. Using the respective width expressions in (4.9), the theoretical torques (τ_a) for each DI version can be computed and are summarised in Table 4.6.

4.5.2 Discussion for analytical results

A visualised comparison of experimental results, analytical answers, and values derived from simulated results is shown in Fig. 4.10, with the numerical results shown in Table 4.6. It is observed that τ_a and τ_s differ significantly in their magnitudes and τ_e is somewhere between them; compared to results in τ_a, those in τ_s do not differentiate between connection styles since there are only five sets of simulated results (one for each DI shape). Since the experimental results (τ_e) represent the actual performance, the differences observed in the simulated (τ_s) and analytical (τ_a) results stem from oversimplified assumptions:

- Simulated torques (τ_s) are smaller because the simulation assumes a uniform velocity across the DI, neglecting the linear velocity distribution along the tail's length and the impact of DI orientation. This simplification leads to an underestimation of the aerodynamic torque.

- Analytical torques (τ_a) are larger because the model uses a constant drag coefficient across the DI, not accounting for the variation in C_{dE} along the length of the DI. This assumption causes an overestimation of the torque compared to the experimental results.

The analytical results, while not matching the experimental magnitudes precisely, accurately predict the relative differences between the DI versions, a feature the simulated results do not possess. This confirms that the differences between experimental and simulated results, as well as those between the two connection styles, are indeed due to the rotational nature of the AeroTail and the resulting variable wind speeds. A discrepancy is noted in e.1 and e.2, likely due to manufacturing imperfections, as the frontal shape of the DI becomes more circular with increasing n, reducing the differences between connection styles.

4.5.3 An improved analytical method

A major problem with the results calculated from simulation in using the previous analytical method is that the "average" wind speed is simply taken as the speed at the centre of the DI (end of tail body). This does not reflect reality well since the flow speed is overwhelmingly concentrated on the outside of the DI due to the rotational nature of the tail. Moreover, the drag force is assumed to be acting on the DI centre which produced unrealistic torque because the lever arm is of unrealistic length. Furthermore, since the drag coefficient used for the analytical methods is calculated from simulation results as well, this inaccurate representation of average

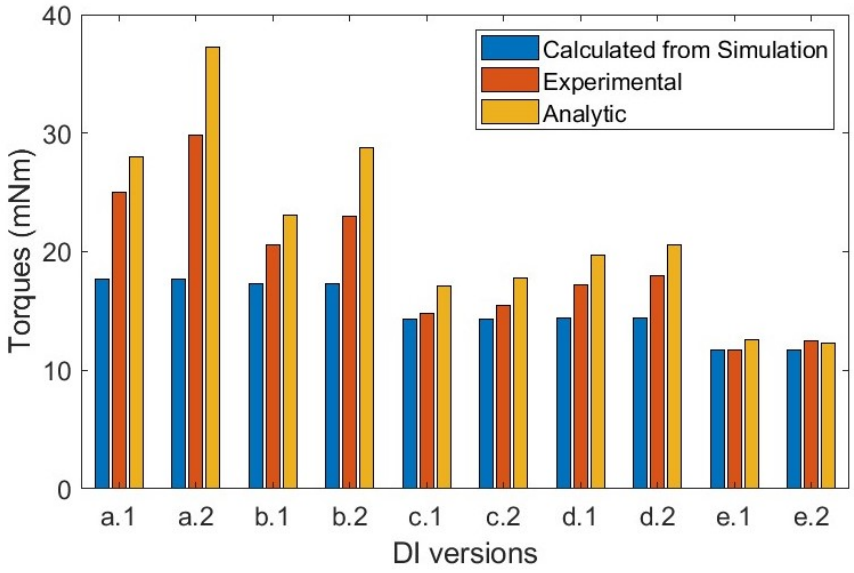

Figure 4.10: Comparison of experimental results (τ_e, orange), analytical answers (τ_a, yellow), and values from simulated results (τ_s, blue).

wind speed undermines the accuracy of the analytic results as well. Therefore, we need a more realistic representation of the average flow velocity.

The average flow velocity in a wind tunnel with varying values can be obtained as the "mass-averaged velocity" (AMV), which takes flow mass into consideration:

$$\begin{aligned} U_{avg} &= \frac{\int_A \rho U d\dot{m}}{\int_A d\dot{m}} \\ &= \frac{\int_A U^2 dA}{\int_A U dA} \end{aligned} \tag{4.13}$$

where U_{avg} is the mass-averaged velocity, U is the steady-state flow velocity in the wind tunnel, A is the area of the inlet/plane the flow is coming through, and $\dot{m}$ is mass flow rate. Thus, the velocity is weighted in this case. Usually, the U_{avg} is measured by built-in functions of the CFD; however, if the flow velocity varies linearly in only one axis, it is easy to derive an analytical expression for the mass-averaged velocity. If the gradient k of the varying velocity is known, then the AMV can expressed as:

$$U_{avg} = \frac{U_0^2 H + U_0 k H^2 + \frac{1}{3} k^2 H^3}{U_0 H + \frac{1}{2} k H^2} \tag{4.14}$$

where U_0 is the velocity at the bottom of the DI, H is the height of the DI and K here corresponds to the angular velocity of the tail. The variables are visualised in

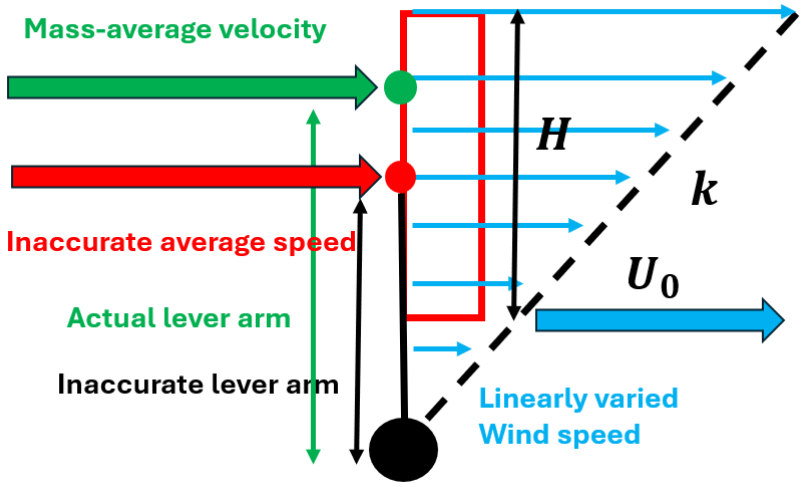

Figure 4.11: Mass-averaged velocity explained. The realistic average wind speed and the lever arm are not at the DI centre like previously assumed.

Fig. 4.11. Now the accurate lever arm length R_{la} can be found at:

$$R_{la} = \frac{U_{avg} - U_0}{k} \tag{4.15}$$

from the tail centre.

Using the newly obtained average velocity and lever arm length, the results are shown in Fig. 4.12 while the original results are in Fig. 4.10. We can see the direct calculation results are much closer to the true value for most DI versions. Unlike the old method, the results now differentiate the orientations 1 and 2. However, there are some outliers: DI c.1 and e.1. This is because the direct calculation still ignore the width thus the effective area of the DI, therefore, the analytical methods is still important. Since the drag coefficient C_d used in the analytic method is also calculated from the simulation results, more accurate average velocity yields more realistic estimated C_d as well. With AMV applied, the average error of the analytical method drops from 14.4% to 6.6% and the large gaps in previous studies cease to exist.

4.6 Chapter summary

This chapter presents a comprehensive study on the optimisation of drag-inducing device designs for the AeroTail, incorporating CFD simulations and experimental validation. The primary goal is to maximise aerodynamically induced torque for robotic balancing, adhering to specific dimensional and weight constraints. Given the scarcity of analytic and experimental research on optimal shapes for DIs, CFD

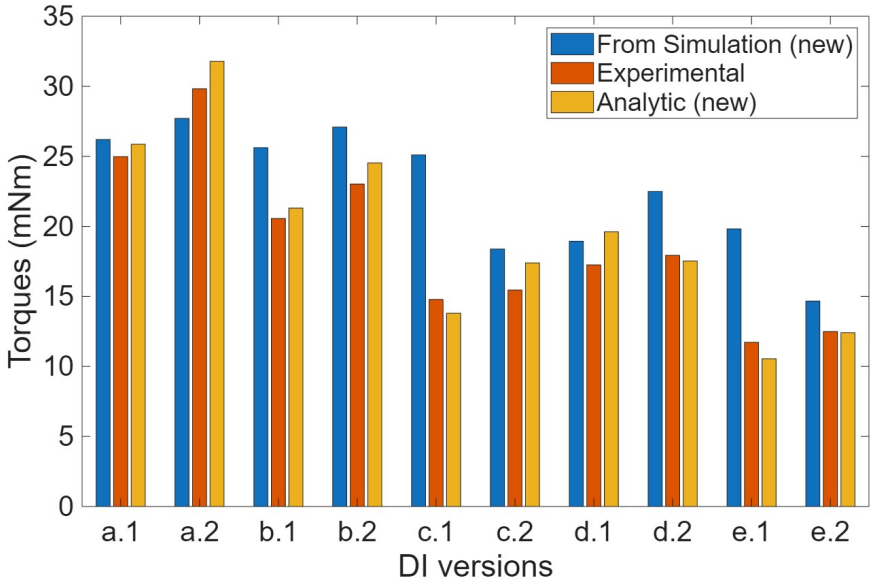

Figure 4.12: The new estimated results compared to experimental results. Here, the mass-averaged velocity is applied to both the direct calculation and analytical method. The results are way closer to the true (experimental) results.

simulations emerge as a foundational step for this investigation. The simulations reveal that among the evaluated shapes, the semi-sphere demonstrates superior performance. It is also noted that DIs with slender frontal surfaces, arch-like profiles, and closed ends generally yield higher drag coefficients. However, it's established that a complete frame design results in material wastage, leading to the introduction of the more efficient "T" shaped frame. Subsequently, the DI frame design is optimised to maximise frontal area, which is a more reliable attribute to enhance within the current frame structure. While a strong theoretical foundation is provided by the simulation studies, these insights cannot be validated without experimental trials. In the following experiments, the results confirmed that the most torque is generated by DI with a semi-cylindrical film of configuration (a) and connection style 2, outperforming style 1 by 20.8%. This indicates that connection style plays a huge role in the difference of torque-generating performances. Subsequently, an analytical method developed for torque calculation is used to elucidate the disparities in quantitative experimental outcomes.

This chapter sees the end of the balancer side of the research. In the next chapter, the C-SEA jumping mechanism are explained. Both theoretical simulation and experimental validations on the findings and performance will be included.

Chapter 5

CVT enhanced series-elastic jumping

This chapter introduced a theoretical continuously variable transmission gearbox that can be incorporated into series-elastic actuators for robotic jumping, a mathematical models for the hopping robot powertrain, including the CVT gearbox and a simplified model for an electric motor powered prismatic actuator suitable for iterative simulation, and a comparative simulation studies to examine the performances of both the C-SEA and regular SEA in various scenarios. The advantages and limitations of the mechanism are analysed. Following that is the mechanical design section for jumper prototypes utilising this novel actuator.

The structure of the chapter is as follows. In Section. 5.1, how to approach the analysis of a CVT-enhanced SEA is discussed; the structure of the hopping robot's powertrain is defined and the design criteria are specified. Section 5.2 introduces the mathematical models of the powertrain, the CVT gearbox, and the electric motor powered prismatic actuator; the constants that are later used in the simulation are also calculated from the design criteria. In Section. 4.2, two simulations are done: simulation 1 examines the general behaviours of the mechanisms when being powered by an ideal actuator; simulation 2 uses the full motor model to evaluate the effects on the height performance by specific variables. And finally, in Section 5.6 are the mechanical design for CVT and jumper prototypes.

5.1 Methodology for designing the C-SEA

To simulate a CVT-enhanced SEA robotic jumping, the advantages of having a mechanism between the elastic element and the end-effector with variable MA need to be analysed and understood. First of all, by aligning the MA profile and the spring's linear behaviour, the end-effector can produce almost constant force output, which

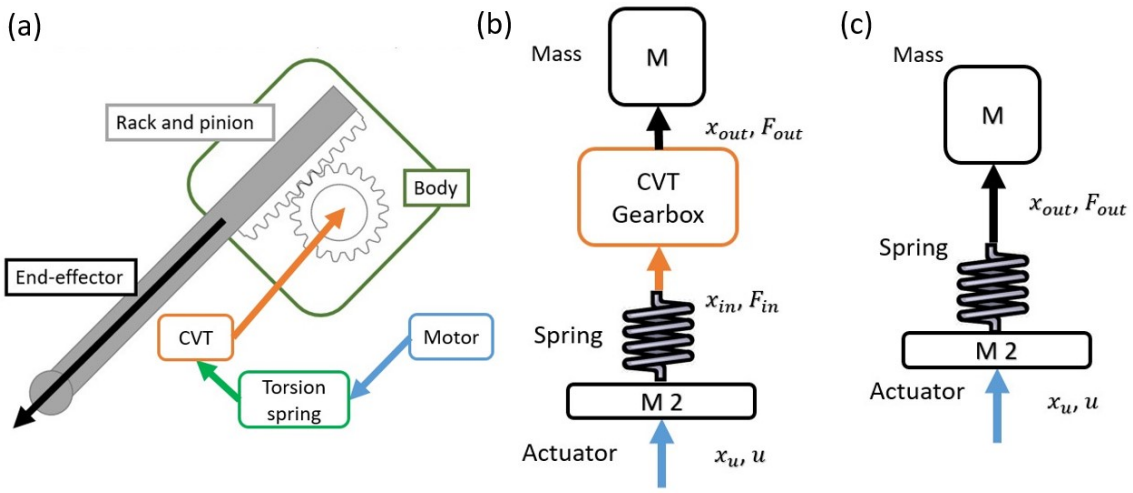

Figure 5.1: A simplified structure of a hopping robot with C-SEA (a) and the isolated powertrains. Scenario (b) is the powertrain with a CVT and (c) is for a conventional SEA.

reduces the peak ground reaction force. At the same time, having a high MA at the beginning of a stroke allows the spring to be fully compressed, thus it stores maximum energy to be released during the remainder of the stroke [33]. The first advantage improves structural integrity and reduces the material requirements for the leg mechanism, and the second one enables the robot to achieve higher jumps. This varying MA "gearbox" can be in the form of a CVT gearbox that can produce a precise MA profile that exactly matches the behaviour of the spring.

Generally in simulation, the structure of the device needs to be simplified enough so it can be mathematically defined. As shown in Fig. 5.1 (a), the hopper consists of a body and a leg mechanism for locomotion, with the powertrain contained inside the body. In a realistic scenario, the powertrain only provides angular motion; then, it is converted into linear motion by a rack-and-pinion mechanism. However, to avoid any complex dynamic model, the powertrain of the jumper is isolated and linearised. In Fig. 5.1 (b) and (c), the mass M represents the robot body and M_2 is the mass of moving components in a motor; the corresponding behaviours of each section of the powertrain are denoted by the letters on the side. In the linearised model, the motion of the robot body relative to the ground is simply represented by that of the mass M with respect to the surroundings. Since the primary objective of utilising the C-SEA is to maximise jump height, there should be a target height for the robot to reach, a fixed body mass and a maximum stroke length for the end-effector. In this case, the design criteria for the robot with a body mass of 100 g is to jump to 1 m with a stroke length (x_{max}) of 0.2 m. The parameters are averages from past lightweight jumping robots like Salto [33], EPFL jumper [25] and MSU jumper [126]; the

numbers are adjusted to be mathematically convenient. The variable v_{max} is defined as the velocity of the robot body at the lift-off (the end of a stroke where the end-effector is no longer touching the ground) which directly determines the height the jump can reach. In this model, only the one dimensional vertical motion of the robot is concerned. However, balancing mechanisms such as AeroTail [28] can be easily added to allow locomotion due to its structural simplicity.

5.2 Mathematical modelling

Following the assumptions made in Section.5.1, mathematical models for the powertrain and the CVT gearbox can be derived. Some initial conditions that will be useful in the simulation are also provided by the models. Additionally, a model for a realistic electric motor is provided in this section.

5.2.1 Powertrain and CVT models

The characteristics of CVTs compared to regular gearboxes with variable gear ratios is that a CVT can adjust gear ratio in a smooth range instead of fixed steps. Therefore, how the gear ratio changes is very flexible and open to imagination. For the simplicity of modelling, the CVT gearbox has linear inputs and outputs in the forms of displacement and force instead of angles and torques. Still using the powertrain structure in Fig.5.1 (b) and assuming the spring used has perfectly linear behaviour, the input force (F_{in}) can be calculated using:

$$F_{in} = k(x_u - x_{in}) \tag{5.1}$$

where k is the spring constant, x_u is the displacement of the actuator and x_{in} is the input displacement into the gearbox. The gear ratio ($Gr(x_{in})$) of the CVT is set to be a linear function of the input displacement:

$$Gr(x_{in}) = G_0 - R \cdot x_{in} \tag{5.2}$$

where G_0 and R are constants according to the properties of the CVT gearbox. In this case, the mechanical advantage (M_A) of the gearbox is simply the inverse of the gear ratio:

$$M_A = \frac{1}{Gr(x_{in})} = \frac{1}{G_0 - R \cdot x_{in}}. \tag{5.3}$$

Therefore, the output displacement (x_{out}) and the output force (F_{out}) from the gearbox can also be calculated:

$$\begin{aligned} x_{out} &= \int Gr(x_{in})\, dx_{in} = G_0 x_{in} - \frac{1}{2} R x_{in}^2 \\ F_{out} &= F_{in} \cdot M_A = \frac{k(x_u - x_{in})}{G_0 - R \cdot x_{in}} \end{aligned} \tag{5.4}$$

and the dynamic behaviour of the powertrain can be simulated using Euler method in later sections.

5.2.2 Constants calculation

Using the design criteria and assumptions made in Section.5.1, constants from equations (5.1) to (5.4) can be calculated and used as known values later on in the simulations. Given the stroke length x_{max}, target height h_t and mass of the robot body m_r, the ideal spring constant k, and target v_{max} can be calculated using the conservation of mechanical energy:

$$\begin{aligned} U_1 &= U_2 = U_3 \\ mgh_t &= \frac{1}{2} k (x_{max})^2 = \frac{1}{2} m_r (v_{max})^2 \end{aligned} \tag{5.5}$$

where U_1 is the potential energy from height, U_2 is that from the compressed spring and U_3 is the kinetic energy of the mass at the end of the stroke. In this model, drag and damping are assumed to be negligible. Thus, the ideal spring constant can be calculated as 49.05 N/m; the target v_{max} is 4.43 m/s; and the fully compressed spring produces a force of 9.81 N (denoted by F_0). To generate a constant output force, this condition has to be true:

$$\frac{dF_{out}}{dx_{in}} = 0, \tag{5.6}$$

and thus we get relations:

$$\frac{F_0}{G_0} = \frac{k}{R} \tag{5.7}$$

where F_0 and k are known. If we assume the total output stroke length is the same as the input one, the remaining two constants can be calculated: $G_0 = 2$ and $R = 10$. When the CVT consists of conical rollers, R directly reflects the slope of the cones; when it does allow the gearbox to have a mechanical advantage profile that produces constant output force, it is named the "critical gear ratio constant". For clarity and realism, the R used in the simulation is 9.9, slightly smaller than the critical gear ratio constant.

5.2.3 Motor model

Various previous works have used a standard model for electric motors [70, 127]. The linearised version of the equations is illustrated below:

$$\begin{aligned} V =& L\frac{dI}{dt} + RI + kv \\ I =& \frac{F + k_m v}{k} \end{aligned} \tag{5.8}$$

where L is the terminal inductance, R is the winding resistance and k is the motor's back EMF constant with a unit of $N \cdot A^{-1}$ (newton over ampere); V, I, F are the voltage input, current and the motor force output respectively. Compared to their original counterpart, several modifications have been made. Motor constant k no longer has a unit of Nm/A since it is linearised and describes the relation between the input voltage and the v (unit m/s) instead of the angular velocity ω (unit s^{-1}). At the same time, the motor torque output T_m is changed to simply force F. From (5.8), the expression of the motor's force output as a function of its velocity can be derived:

$$F = (\frac{k_m}{k})V - k_m v \tag{5.9}$$

where v is the motor velocity and k_m is a constant known as the viscous damping coefficient. It can be calculated using:

$$k_m = \frac{kI_0}{v_0} \tag{5.10}$$

where v_0 and I_0 are the no load velocity and current. Since the input voltage is assumed to be constant, (5.9) can be further simplified to:

$$F = F_0 - k_m v \tag{5.11}$$

where F_0 is the "stall force" of the motor (same as the maximum spring force).

5.3 Simulation

Two simulation studies are done in this section. Simulation 1 is to showcase the general behaviour of the C-SEA with a single end-effector stroke intending to propel the robot body to the target height. The output accelerations and velocities are compared with their SEA counterparts in specific scenarios. Simulation 2 studies the factors that can affect the v_{max} achieved by the actuators in question and the results from various input combinations are compared and analysed. The simulations in this

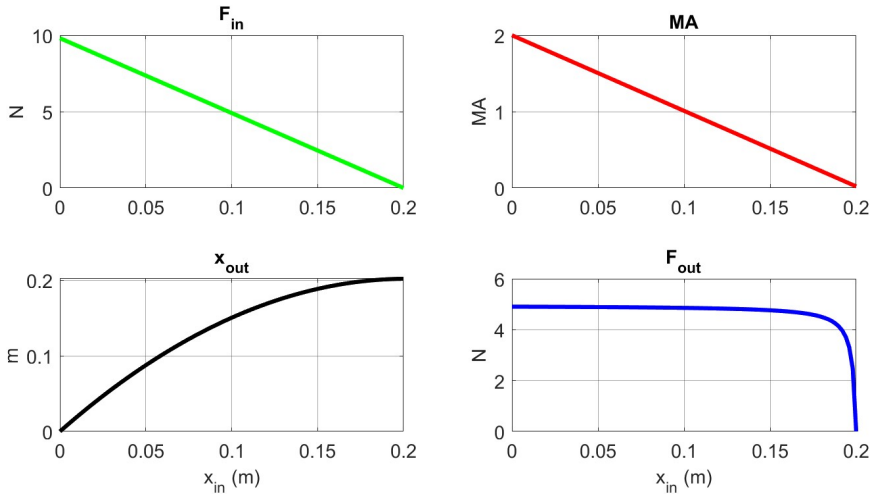

Figure 5.2: The results from the kinematic simulation. The input force (F_{in}), mechanical advantage (MA), end-effector position (x_{out}) and output force (F_{out}) are plotted against the input displacement (x_{in}).

study are exclusively done in MATLAB using the Euler method with a time step of 0.1 millisecond.

5.3.1 Simulation 1

An important characteristic of the C-SEA is producing reduced and almost constant output force, and this is enabled by the gear ratio being a linear function of the input displacement. To showcase this feature, a kinematic simulation of the CVT gearbox is done. The governing equation of the behaviour is based on (5.4) with some modifications. We assume the system is not actuated but simply powered by a compressed spring and only the analytic outputs of the gearbox are being examined (masses are ignored); thus in this case, x_u is a fixed value of x_{max}. If we plug in the constants from Section. 5.2.2, the behaviour of the system in a single stroke is plotted with respect to input displacement x_{in} in Fig. 5.2. The output force is kept nearly constant and only drops at the end of the stroke with a peak value of 4.91N, half of the peak input force of 9.81N.

The next step is to simulate the full dynamic behaviour of both the C-SEA and the regular SEA according to the powertrain structure in Fig 5.1 and the mathematical model in Section 5.2. The powertrain is placed along the vertical direction with the full effect of gravity. m_2 is set to be 10g and the actuator is assumed to generate constant force with no limit on velocity. The maximum extent of x_u is constrained to x_{max} and the lift-off happens when the output displacement reaches x_{max}. The results are demonstrated in Fig. 5.3 where the x-axis is now time. The C-SEA experiences almost constant output acceleration thus linear velocity and ground reaction force

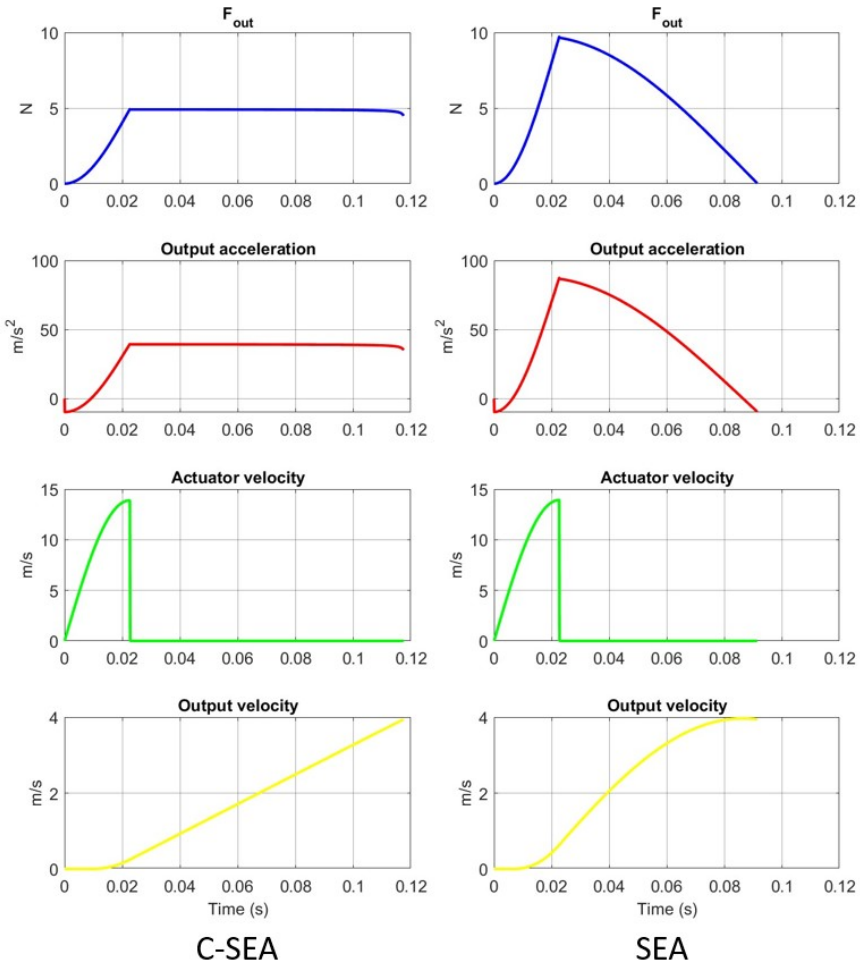

Figure 5.3: The results from the dynamic simulation. The output force (F_{out}), acceleration and velocity along with the actuator velocity are plotted against time. Since the mass remains unchanged, F_{out} and the acceleration have the same shape.

throughout the stroke with a peak value around half of its SEA counterpart. The results also show that the stroke have two stages, the charging and the releasing, in a continuous manner which sees end-effector starting to displace as the spring is being compressed.

The summarised results can be found in Table 5.1. The system with C-SEA takes 0.117 s to reach a velocity of 3.93 m/s while the one without CVT takes 0.091 s to achieve a velocity of 3.97 m/s. C-SEA takes longer to reach the end velocity but v_{max} and thus jump height is only slightly affected (0.787 m for C-SEA and 0.803 m for SEA). Therefore, without the CVT, a regular SEA would have produced 99.8% more peak ground reaction force while reducing the time duration by 22.1%. However, this simulation result still cannot reflect a realistic scenario since the actuator, if being powered by an electric motor, simply cannot generate perfectly constant force output while having no velocity limitation. The maximum velocity reached by the actuator,

Table 5.1: Summary of Simulation 1 results

Scenarios	v_{max}(m/s)	Time(s)	Height(m)	Peak force(N)
Ideal scenario	4.43	–	1.000	9.81
C-SEA actuated	3.93	0.117	0.787	4.91
SEA actuated	3.97	0.091	0.803	9.81

as shown in Fig. 5.3, is a whopping 13.87 m/s which is an unrealistically big number. To make the simulation more realistic, the mathematical model for the electric motor introduced in Section. 5.2.3 should be included in the overall model.

5.3.2 Simulation 2

As discussed in Section. 5.1, the second advantage arises from the initial high MA at the beginning of the stroke and a lower MA at the end, which allows for more thorough compression of the spring, thereby storing greater energy for achieving higher jumps. The rationale behind it is that prolonged charging stages can lead to premature expansion of the spring, resulting in incomplete compression when energy is released. However, the results from Section. 5.3.1 show that the conventional SEA still outperforms in terms of jump height. This largely attributes to the assumption that the ideal actuator produces constant force with unlimited velocity, which is unrealistic and causes the charging stage to be shorter than if an electric motor is powering the actuator.

When considering an actuator powered by a linear electric motor, the time required to compress the spring is influenced by two factors: m_2 and k_m. The first factor is self-explanatory, as larger masses are harder to accelerate according to Newton's second law. The second factor determines how much the force output from the motor decreases as it speeds up. If the actuator has a linear behaviour, the charging will take longer; this consequently causes the spring to prematurely expand. When using the C-SEA, this premature expansion would be mitigated by the high MA at the beginning of the stroke, thus allowing the robot to reach a better height.

To prove the addition of the motor model in Section. 5.2.3 does affect the performance in the manner described above, the general behaviour of the system with the new model is simulated. The k_m is set to be 2 so that when the stall force is F_0, the no-load velocity of the actuator is 4.9 m/s slightly larger than the required v_{max}; everything else remains unchanged from the setup of the dynamic Simulation 1. The results can be found in Fig. 5.4. As expected, the peak force output from C-SEA is still way less than the input even though the constant section is shorter compared to Simulation 1; SEA still takes less overall time to complete the stroke. A major differ-

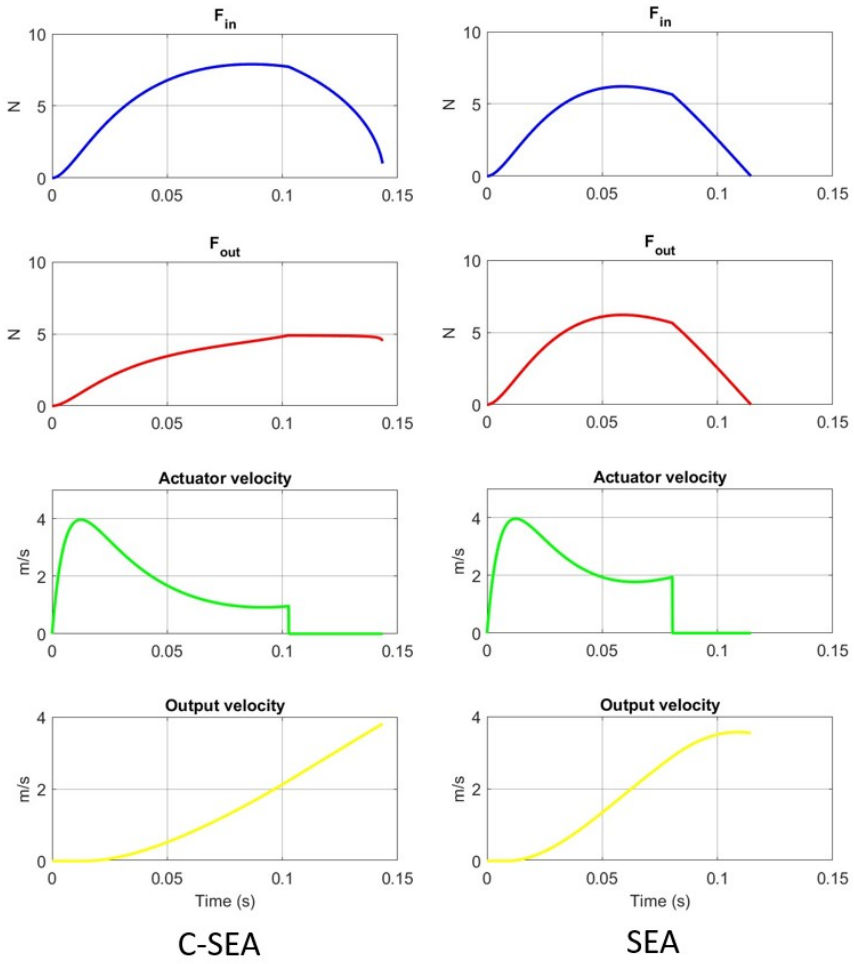

Figure 5.4: The results of simulation 2. The input force from spring (F_{in}), output force (F_{out}), actuator velocity and the end-effector velocity are plotted against time. Since there is no gearbox in SEA, its (F_{in}) and (F_{out}) are identical here.

ence from the previous simulation is that the peak force output now is only slightly higher than its C-SEA counterpart which is precisely caused by the spring in SEA not being fully compressed during the charging stage. Consequently, the v_{max} achieved by C-SEA this time is 3.81 m/s, exceeding the 3.57 m/s of the SEA. This proves the notion mentioned previously: when using a realistically modelled actuator with linear behaviour, the C-SEA still manages to compress the spring fairly well during the charging stage which is now longer, while the conventional performs poorly.

To further study the effects of m_2 and k_m on v_{max} for both C-SEA and SEA, combinations of the variables from wide ranges are used to produce a 3D plot of the results (in Fig. 5.5). M_2 has a range from 1 g to 100 g; the lower bound is a number small enough to represent the lowest possible value for the mass of the moving component in the actuator but still easy enough to simulate, while the upper bound is the mass of the robot body which is impossible to exceed. At the same

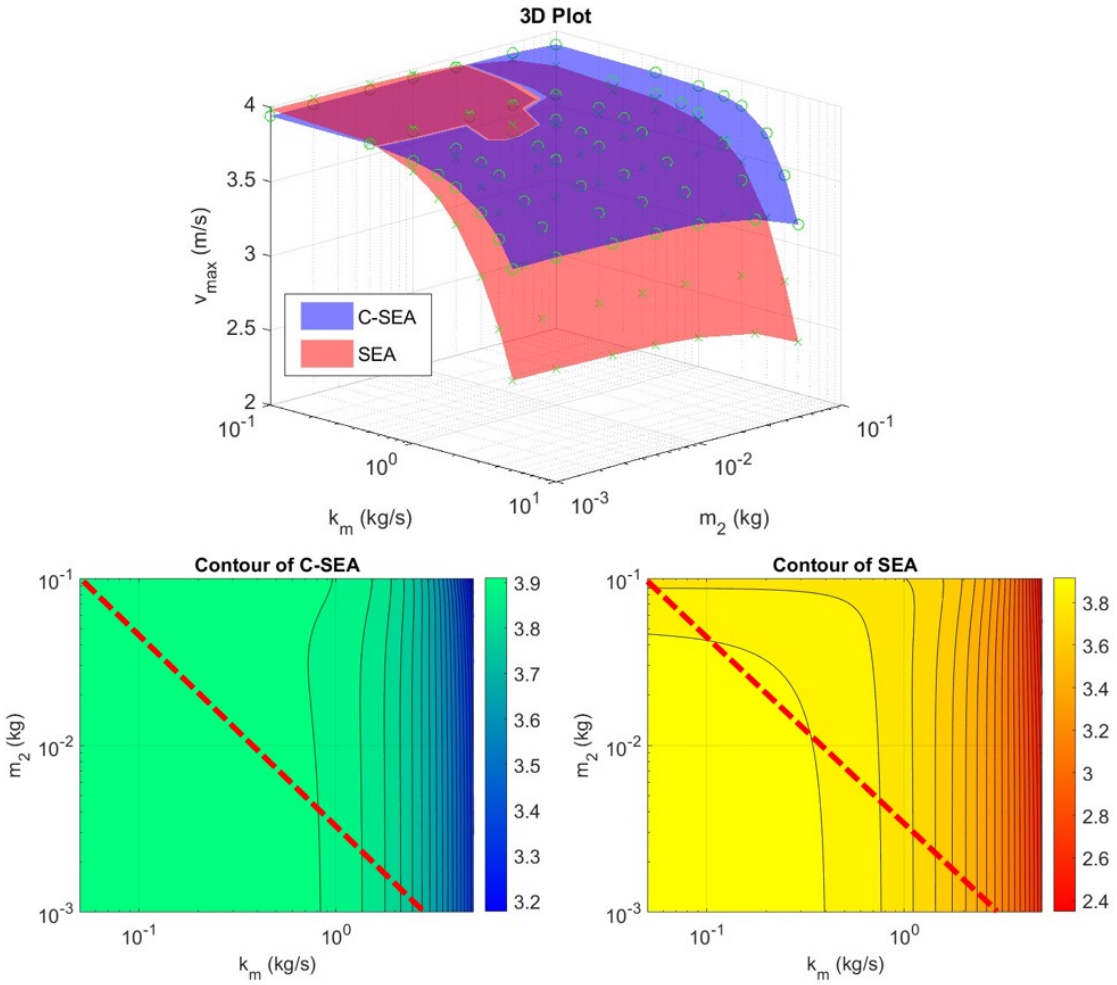

Figure 5.5: The 3D plots for the results from simulation 2 are on the top and their corresponding contours are also shown on the bottom. The endpoints of the red dotted line have Cartesian coordinates $[0, 0.1]$ and $[3, 0.001]$ in the contour plots. The dotted line divides the regions according to whether C-SEA or SEA has the better performance.

time, k_m ranges from 0 to 5. When $k_m = 0$, $F = F_0$; this represents the scenario in simulation 1 where the actuator produces constant force. Lastly, the end-effector fails to complete a full stroke when k_m exceeds 5, thus the upper bound. The values for the variables are distributed in an exponential manner throughout the ranges, and the results are plotted in 3D. Two best-fit surfaces are generated for both the C-SEA and the SEA using the "polyfit23" function. The contours of the surfaces are also shown in Fig. 5.5. The red dotted line divides the contours in two regions, most m_2 and k_m combinations to the top-right of the red line, see higher v_{max} for C-SEA. This indicates that for motors with both larger m_2 and k_m, the C-SEA usually have a clear advantage over the regular SEA.

5.4 CVT sensitivity study

In the previous simulations, the mass and friction of the CVT mechanism are assumed to be negligible, which is not realistic in practice. The loss brought by the extra weight and additional friction of CVT can inevitably compromise the performance of the jumper; this study aims to examine to what extend they do. The typical NG gear style CVT has a mass of 10g and an efficiency of 98% (according to spur gear data).This study manipulate these parameters to see their effects on peak ground reaction force and jump height reached. All other parameters are identical to the previous simulations.

Peak GRF vs. CVT mass

The CVT mass factor is introduced as a parameter representing how many folds the CVT mass is increased (2 means the current CVT mass is twice as the original). The CVT mass is treated as extra load to the body (originally 100g). The results in Fig. 5.6 (a) show that when the factor is increased from 1 to 10, the peak GRF of C-SEA increases 0.29% from 4.881N to 4.895N, which is almost negligible (even though jumper height does suffer from the weight gain). When the same additional mass is added to the SEA jumper, the peak ground reaction force rises 21.02% to 6.405N. Notice that when a CVT of typical mass is included, the peak GRF of SEA is still 4.95% higher than that of C-SEA. It is safe to concluded that the mass of CVT have little effect on the peak GRF produced.

Jump height vs. CVT mass

The increment of CVT mass factor influences the jump height performances differently. Since the SEA does not include a CVT component, the performance is constant at 0.543m and is only used for comparison with that of C-SEA. The results in Fig. 5.6 (b) show that the height reached by the C-SEA decreases with CVT mass and the overtake happens when factor equals 2.7. At typical CVT mass, the C-SEA jumps 16.98% higher than SEA reaching 0.625m.

Jump height vs. efficiency

Due to the asymmetric geometry of the NC gears, modelling the exact Coulombic and viscous friction of them would be difficult. Instead, we simply represent CVT loss using an general efficiency η, so that $CVT_{Out} = \eta \cdot CVT_{In}$ where "Out" and "In" refer to the output and input powers of the CVT. The height performance is then calculated from the CVT work output. Fig. 5.6 (c) shows that as η varies from 100%

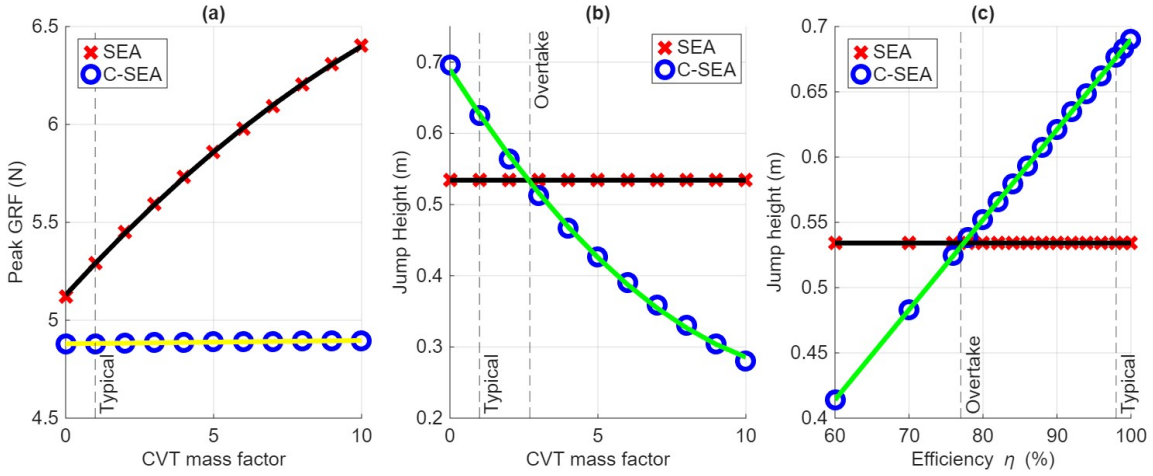

Figure 5.6: The CVT sensitivity study: (a) Peak GRF vs. CVT mass factor, (b) Jump height vs. CVT mass, and (c) Jump height vs. efficiency. Best fit curves are added on top of the data points using POLYFIT. The typical values and overtake points are indicated using dotted vertical lines.

to 60%, the jump height performance for C-SEA drops linearly while that of SEA stays constant (due to the absence of CVT). The overtake happens at 77% efficiency, meaning any value above that would result in C-SEA having a stronger performance. At typical efficiency, the C-SEA jumps 26.60% higher than the SEA jumper.

5.5 Summary for the simulation study

In conclusion, the C-SEA manages to generate nearly constant and lower ground reaction force than the regular SEA sacrificing the time taken to accelerate with minimal loss on jump height. The reduced ground force is beneficial to the structural integrity and means less material requirements for the end-effector. At the same time, when actuated by a realistic motor, C-SEA has a clear advantage in most cases with higher m_2 and k_m outperforming the SEA in terms of achieving high jumps because of the C-SEA's ability to compress the spring more thoroughly even when the charging stage is extended.

In the following sections, the findings in the paper will facilitate the development of a physical CVT gearbox that can be integrated with an SEA for robotic jumping and a prototype of such C-SEA enabled hopping robot will be constructed. Next steps for this research include: choosing a CVT type, parameter optimization for the CVT, designing and fabricating the hopping robot as a testing platform, developing a control strategy for such a robot and conducting comparative experiments. Promising CVT options include Evan's variable speed counter-shaft and the ratcheting CVT; the former boasts a simple and reliable structure, while the latter excels in transmitting

impressive torque with minimal loss [128].

5.6 The jumping mechanism prototype

The simulation studies have demonstrated the advantages of the C-SEA over conventional SEA. The next step of the research to design and construct a C-SEA jumping mechanism prototype to test the real-world performance and to validate the findings from the simulation studies. There are several design criteria and challenges facing the prototype design task. Compromises will be have to be made to bypass the problems in the prototyping process.

- The parameters of the jumper prototype will be based on the values used in simulation. However, it is difficult to make them exact matches. Thus, the experiment conditions with alter accordingly to fit the real parameters while the C-SEA and the SEA can still be compared fairly.
- The CVT gearbox is only conceptual in the simulations. In order to make it practical, a specific mechanism with required functionality needs to be chosen and parametrically tuned to be incorporated into overall powertrain of the jumper.
- The jumper is to be actuated by an electric motor. The motor choice and control method should be suitable so that the tasks in the simulation can be best replicated in practical scenarios.
- Since the jumper is very simplistic with a single degree of freedom leg mechanism, there needs to be an experiment platform supporting the jumper. At the same time, the platform also host sensors to collect data from the experiments.

This section will include the mechanical design process of jumper, the CVT gearbox, the motor control electronics and methods.

5.6.1 CVT gearbox design

The section details the process of choosing a CVT type that fits the criteria in the simulation section and the construction of the jumping robot prototype. There are several requirements of the CVT design that are uncommon among the more conventional types.

- The gear ratio of the CVT should be a linear function of the displacement of the end-effector.

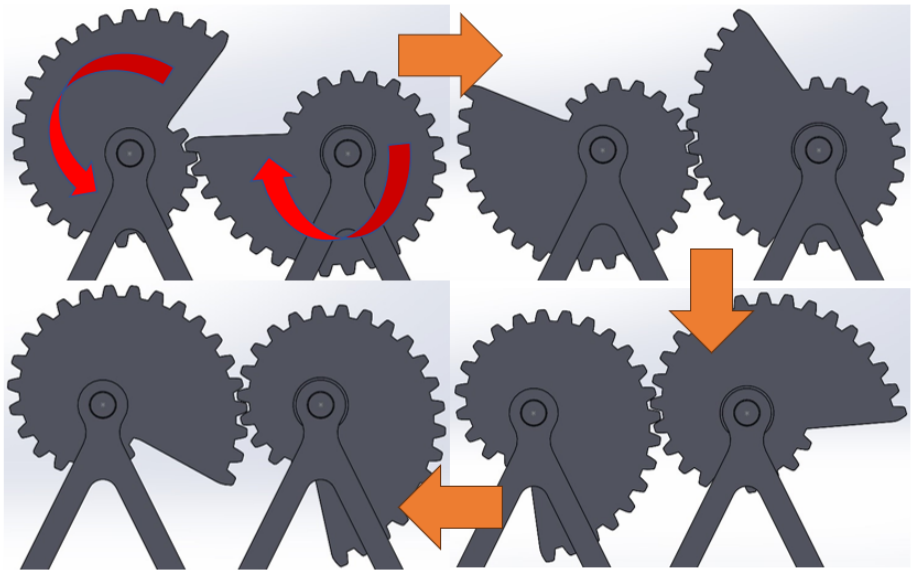

Figure 5.7: The SW assembly that shows the rotation of the gear pair with correctly meshed teeth.

- The gear ratio should vary being lead by the internal mechanical properties of the gearbox so that the general structure of the device is kept simple.
- The gearbox should have positive engagement so large torque can be transmitted.

The non-circular (NC) gears are chosen to be the basis of this new CVT for its simplicity, compatibility. Even though NC gears and conventional CVT are usually separately fields of study, some researches over the years do consider them as a type of CVT that have fixed gear ratio profiles. Generally speaking, NC gears when being used in a transmission scenario, do fulfill the definition of CVT (although they cannot be consider IVTs) and they do fit every criteria of the ideal CVT design. Moreover, the simple structure of the NC gears poses a huge advantage over other CVT types, making it the ideal choice for this application. Furthermore, NC gears have been used in robotic jumping but never in combination with a SEA. Therefore, developing a NC gear-based C-SEA does have scientific significance and novelty.

There are two steps in the NC gear design, namely, determining the pitch curve and then generating the teeth profile. For the first step, the pitch curve ($r(\theta)$) is usually expressed by the radius (the distance from the center of rotation to the pitch line of the gear) as a function of the rotation angle θ in the polar coordinate. The pitch curve is determined by the required gear ratio profile. Knowing the pitch curve, there are online tools to generate the suitable teeth profile so the gears can be modeled and manufactured.

The online tool is on a website called OTVINTA which generate the teeth profile

providing the pitch curve in the form of a script. Then, the script can be exported to Blender to draw a sketch of the gear profiles. Finally, the sketch can be converted into solid bodies in Solidworks so that further modelling can be done. For example, if we assume the expression of the pitch curve is:

$$r = 1 + \frac{1}{\pi}\theta, \tag{5.12}$$

the sketch for the gear profile is then generated in blender. The sketch then was exported to Solidworks to create this assembly of the gear pair shown in Fig. 5.7.

Pitch curve generation

Generally, the pitch curve of the driving gear in a NC gear pair is $r_1(\theta)$ and that of the driven gear can be expressed as:

$$r_2(\theta) = A - r_1(\theta) \tag{5.13}$$

where A is the distance between the two CoRs of the gear pair. Then the gear ratio of such gear pair can be calculated as:

$$Gr(\theta) = \frac{r_1(\theta)}{r_2(\theta)} = \frac{r_1}{A - r_1}. \tag{5.14}$$

The required gear ratio profile is known from Section 5.2, equation (5.2) and its polar expression is:

$$Gr(\theta) = G_0 - R\theta \tag{5.15}$$

where G_0 and R are constants. Equations (5.14) and (5.15) can be combined and re-arranged into:

$$r_1(\theta) = \frac{A(G_0 - R\theta)}{1 + (G_0 - R\theta)}. \tag{5.16}$$

In Section 5.2, in order to calculate the values for G_0 and R, other assumptions have to be made, namely, the full extension of motor and leg are both 0.2m. However, the rotational nature of the new model here means the range of motion for both NC gears are simply a full rotation (from 0 to 2π). In this case, G_0 and R are calculated to be 2 and $\frac{1}{\pi}$ respectively. Now equation (5.16) becomes:

$$r_1(\theta) = \frac{A(2 - \frac{1}{\pi}\theta)}{(3 - R\theta)}. \tag{5.17}$$

If we than plug in $A = 3cm$, we get the polar expression for the pitch curve of the driving gear. The resultant NC gear set will be used for the CVT component for all

jumper prototype versions.

Now we have derived the theoretical pitch curve for the NC gear set, one more step needs to be taken before implementation. The values of G_0 and R cannot be 2 and $\frac{1}{\pi}$ exactly in practice because this would cause the gear ratio to reach 0 at full leg extension, which is mathematically invalid. The physical representation of a 0 gear ratio would be the gears being stuck and we will try to avoid that. During the theoretical calculation of G_0 and R, a relation between them is met:

$$G_0 = 2\pi \cdot R \tag{5.18}$$

which is not actually a hard requirement. This relation ensures the resultant ground reaction force to be completely constant throughout the leg stroke. However, this does not need to be rigidly true for the advantages of having a CVT gearbox to mostly embody. In this case, we can rewrite (5.18) into:

$$G_0 = (2\pi + \rho_\kappa) \cdot R \tag{5.19}$$

where ρ_κ is the the value that curves this relation. When ρ_κ is a positive real number, the gear ratio would never be 0 thus solving the mathematical invalidity in the theoretical model. Fig. 5.8 shows the output torque from the CVT gearbox with respect to the input rotation under three different ρ_κ values. We have established that a complete constant output would be impossible, a very large ρ_κ value is also problematic. When $\rho_\kappa = 5$, the peak output torque is 0.225Nm, only achieving a reduction of 40.9%; there is also significant work loss (work done can be obtained from the areas under the curves). Through trail and error, we found a reasonable value of 0.13 for $\rho_\kappa = 5$, and we manage to produce a output curve that is largely constant and only dropping at the end. In this case, the G_0 and R values use are 1.96 and 0.306 respectively.

Teeth profile design

When trying to implement the NC gear pairs into a gearbox configuration, we realised the gears often loose grip when the leg is at full extend. After carefully examining the gear models and contact testing, we concluded that the models are topologically sound, but rather, the problem is with gear meshing. When under load, the gears cause the surrounding structures to deform, which causes the teeth to slip and loose contact. This deformation is small enough to be handled by circular gears but is problematic to NC gears due to their acute positioning. To solve this, there are two ways to improve gear meshing: pitch angle and gear size. As the pitch curve and the

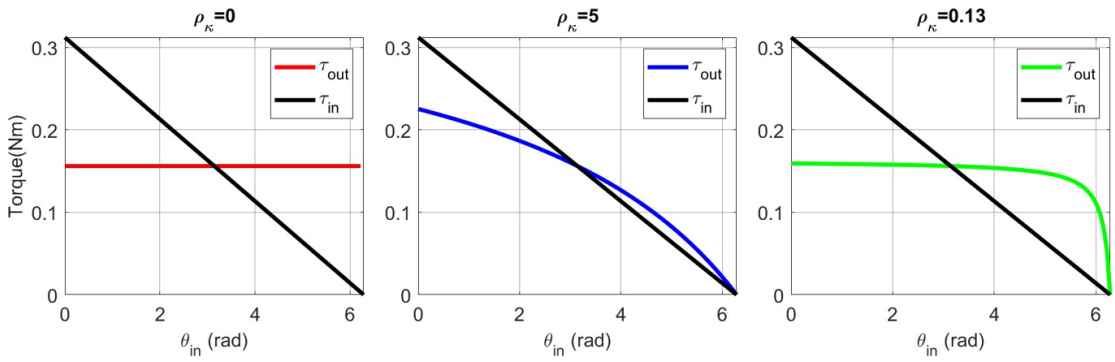

Figure 5.8: The plots of output torque from the CVT gearbox against the rotation angle of the driving gear.

overall gear size is know, increasing the gear size means decreasing the teeth number. Based on this idea, we conducted a qualitative gear meshing comparison test.

The NC gear sets in question are shown in Fig. 5.9 and they have various pitch angles (PA) and numbers of teeth (TN). In the online tool for NC gears, there are two options for the pitch angle 20° and 14.5° but the number of teeth can be freely customised. The set originally used was a PA20TN30 (a pitch angle of 20° and 30 teeth), thus for TN of 30, only the PA 14.5° is made. Another 6 sets are made with both PA options and TN ranging from 15 to 25. They are tested on regular jumper frames with an applied torque of 0.318 Nm with is the highest torque the gear set need to endure. The results shows that 14.5° PA generally have a better grip then 20° and increasing the size of teeth do improve contact. However, have too few teeth also have drawbacks, namely, the accuracy starts to drop and unwanted vibration begins to appear when TN is reduced to 15. Sets PA14.5TN30, PA14.5TN25, and PA20TN25 all failed (loose contact during) the test. Therefore, PA14.5TN20 are chosen to the optimal NC gear set for the jumper.

5.6.2 Jumper prototypes

Jumper prototype Version 0

The general structure of the jumper powertrain have already been mention in the previous sections (Fig. 5.1 (a)). To summaries, the system is powered by an electric motor which is usually of rotational nature; the CVT gearbox, which consists of a NC gear pair, also transmits rotation and torque. This means the most sensable option for the elastic element, which is between the motor and the CVT, is a torsion spring. Then, the angular output from the CVT gearbox is converted to linear motion by a rack-and-pinion mechanism. Fig. 5.10 shows the overall structure of the jumper prototype. The positions of the main components (motor, spring, CVT gearset, and

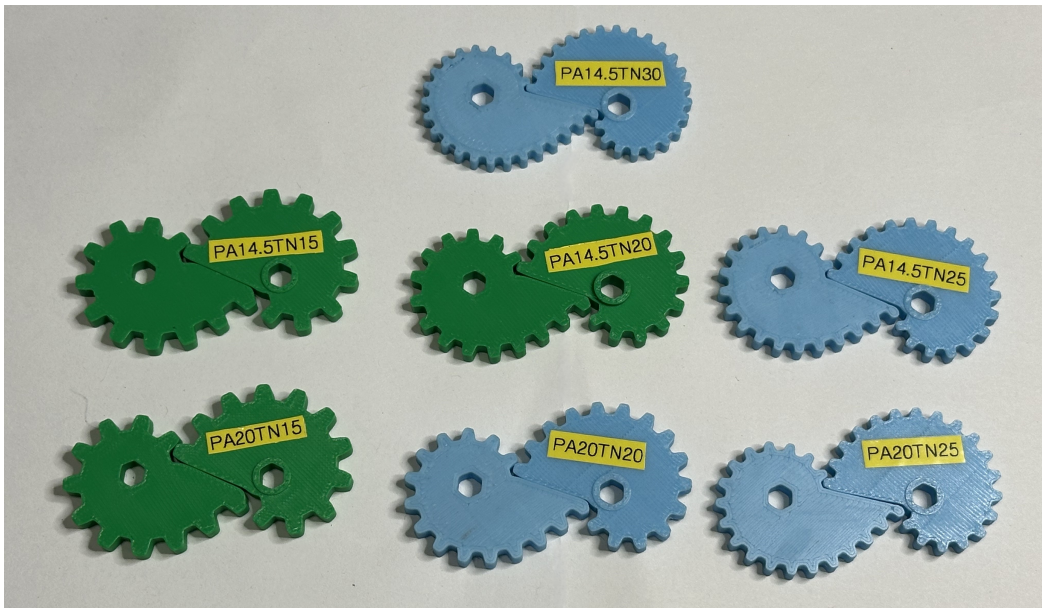

Figure 5.9: All the NC gear teeth configurations in the meshing test. "PA" stands for pitch angle and "TN" stands for teeth number. Material colours are irrelevant.

the rack-and-pinion mechanism) in the jumper powertrain are shown in the figure. The rack is fixed on the leg which is confined by two leg supports with rollers to a 1 degree-of-freedom linear motion. The jumper also contains mounting position for encoders in order to sense the rotation angle and speed of both the motor and the pinion. All the components are sandwiched between two main frames. See Appendix A for more details of Jumper Ver.0 (figures with zoomed in views). Ver.0 is the conceptual design of the jumper prototype in which the mechanical details reflecting real-life components are not illustrated. They will be introduced in Ver.1.

Jumper prototype Version 1

The Ver.1 jumper (in Fig. 5.11) includes realistic mechanical details making it manufacturable in practice. This version does not have either motor or encoders and only the mechanical components are included (the spring casing is fixed on the frame). It can only perform single jump by a push-and-release action. The main purpose is to test the compatibility of the the gear sets in the powertrain. The leg support system are now functional with grooved rollers and track added to guide and restrict the leg motion. Ball bearings are used at the connection between shafts and frames. A gearbox support frame is added to side of the main frame for extra strength and compactness. All components are 3D printed except screws, washers, nuts, and bearings. See Appendix A for the constructed Ver.1 jumper.

The testing results show that the leg reaction force at any given spring compression is smaller than the theoretic value while the general trend of the measured values

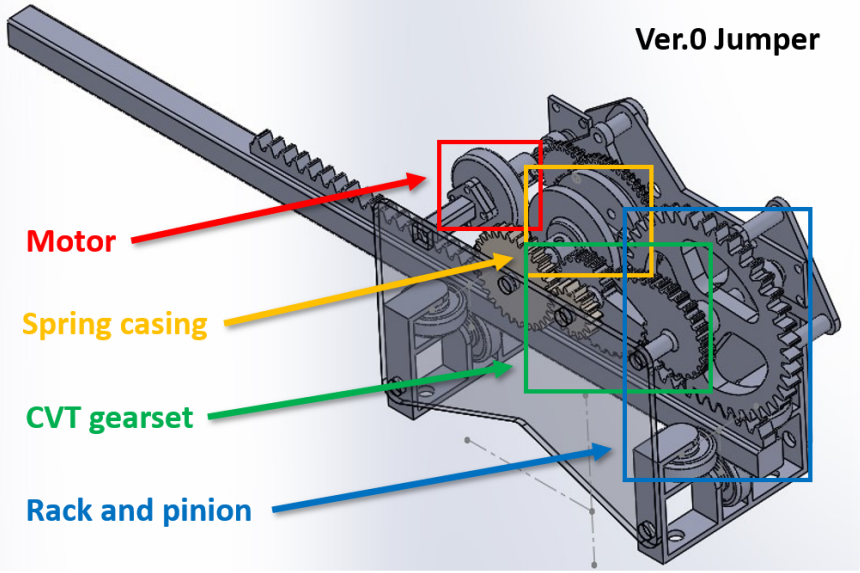

Figure 5.10: The conceptual mechanical design of a C-SEA jumping device. The main components in the powertrain are pointed out in the figure. More detailed illustrations are included in the Appendix.

matches the theoretic value (Fig. 5.15). This is caused by a mismatch of the converter gearset resulting the spring not being compressed fully. At the same time, the leg motion is way slower than expected meaning the friction in the roller-track leg support system is too high.

Jumper prototype Version 2

In order to solve the aforementioned issues and to overall improve the jumper design, several modifications have been made since.

- The converted gears are tuned to the correct sizes which enable the spring to be fully compressed.
- The roller-track leg support system is replaced by a guide rod. Instead if having 3 rollers on each side of a leg with rectangular cross-section, the leg now consists of a steel guide rod and the rack parallel to each other; and there are linear ball bearings acting as the connection between the guide rod and the support frames.
- The elastic element have been updated from a joint two-spring mechanism to a single spring with desired constant. The casings are modified to fit the new design.
- The material used for the 3D printed gears used to be Tough 2000 resin which is sticky and thus can induced unwanted friction. The material has been changed

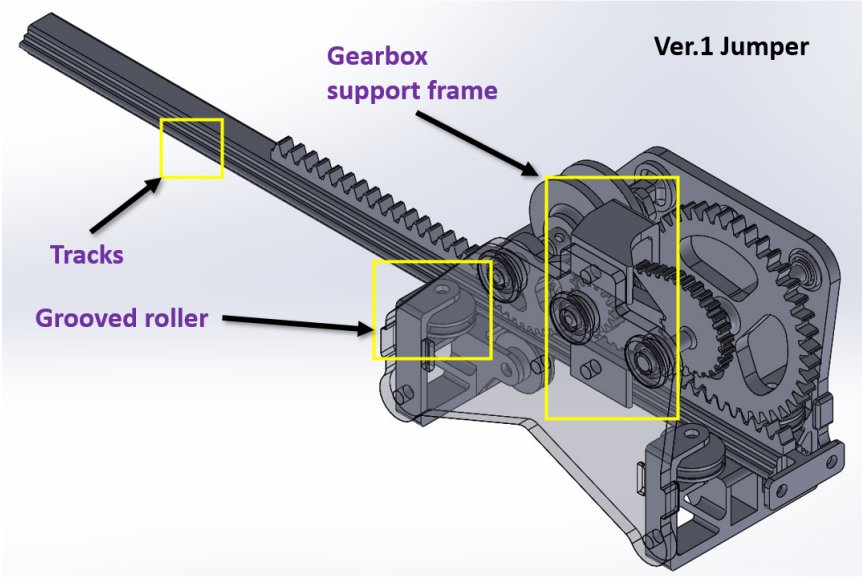

Figure 5.11: The Ver.1 of the jumper, which includes realistic mechanical details. This figure highlights the main changes made to the design compared to the conceptual Ver.0 design.

to PLA, which have a smoother surface; this alternation has improve the gear efficiency.

- The gears and shafts used to be single parts since they used the same material. Since the gears now use a different material which is not suitable for shafts, a new connection method is implemented. Hexagon connector nuts are used between shafts and gears to transmit torque and rotation and they secured using superglue.

See Appendix A for the constructed Ver.2 jumper. The next step is to install the motor and encoder to complete the jumper design.

Jumper prototype Version 3

The Ver.3 of the jumper is a motor-actuated device unlike the previous versions which can only perform push-and-release actions. The motor and the gearbox are installed onto the jumper frame together as an integrated module. The gearbox has a 2 step speed reduction; the rotation is transmitted from the motor at the bottom to the output gear at the top. The gear ratio of the gearbox is 10 : 1 which is realised by the first 3 gears and the last output gear is added as a connector for distance management. The output from the gearbox is connected to the spring casing which is no longer fixed on the frame. Magnetic encoders are installed as well; one is on the back of the motor and the other is behind the pinion, measuring their respective

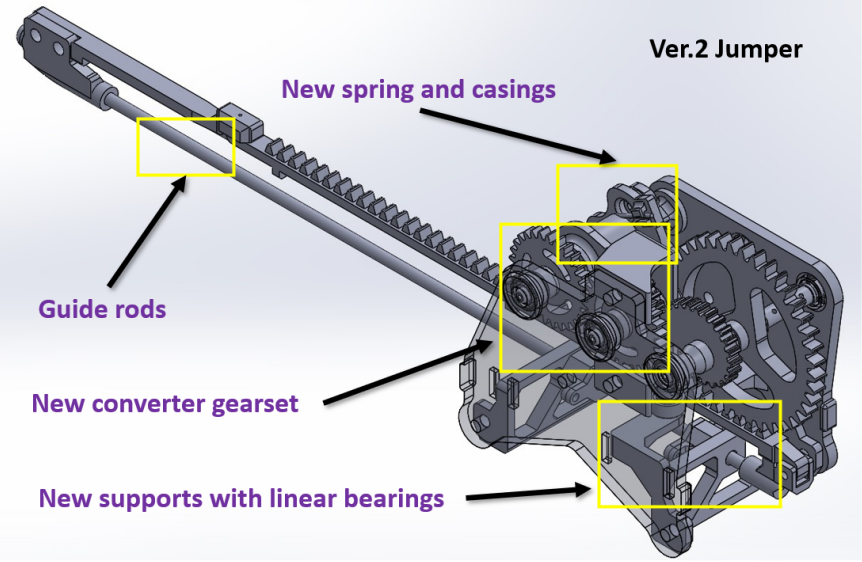

Figure 5.12: The Ver.2 of the jumper. This version includes new features that solves the previous issues and made improvements overall. The modifications are highlighted.

positions and velocities. More closed in view of the encoder boards and the gearbox-motor module are included in Appendix A. Additionally, mounting frames are added to the back of the jumper. The mount include casings for linear bearings that are compatible with the experiment platform.

Measured GRF vs. Theoretical values

This section includes the plots of measured GRF values with respect to leg extension compared with the theoretical values. Results for both Ver.1 and Ver.3 are included in Fig. 5.15. The results for Ver.1 reveals a converter sizing problem that has been discussed in the Ver.1 section; Ver.3 has solved the issue by modifying the converters to the correct sizes. The results for Ver.3 indicates the measured data roughly coincide with the theoretical values confirming the successful modification. Notice that the theoretical data corresponds to these shown by Fig. 5.2 in 5.3.1. Since the smooth action cannot be guaranteed by Ver.3, the dynamics results like in Fig. 5.3 cannot be obtained in the current version. These tests will be done as a part of future work.

Actuation

The system is actuated by a three-phase brushless direct-current (BLDC) motor with a KV constant of 1800. The motor is controlled by a DengFOC motor drive and a ESP32 microcontroller board. The motor control code used is Arduino based field-oriented control (FOC) algorithm. The pictures of these devices can be found in Fig.

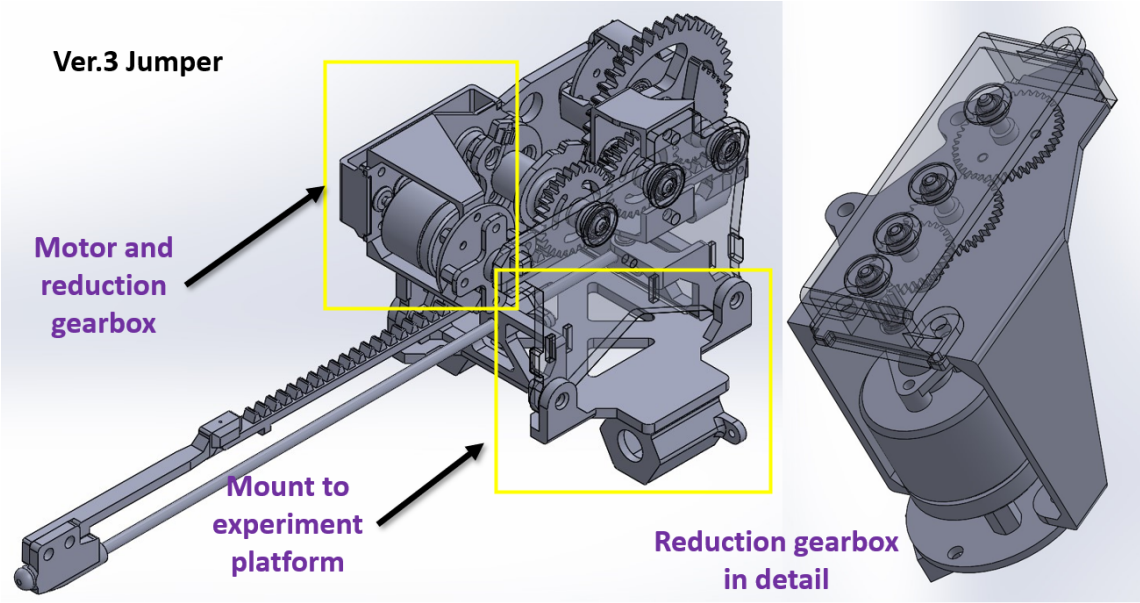

Figure 5.13: The Ver.3 of the jumper prototype. The motor with reduction gearbox has been added to the jumper. On the right side of the figure is a close up view of the integrated motor-gearbox module. Mounting frames are also added to the back on the jumper to be mounted onto the experiment platform.

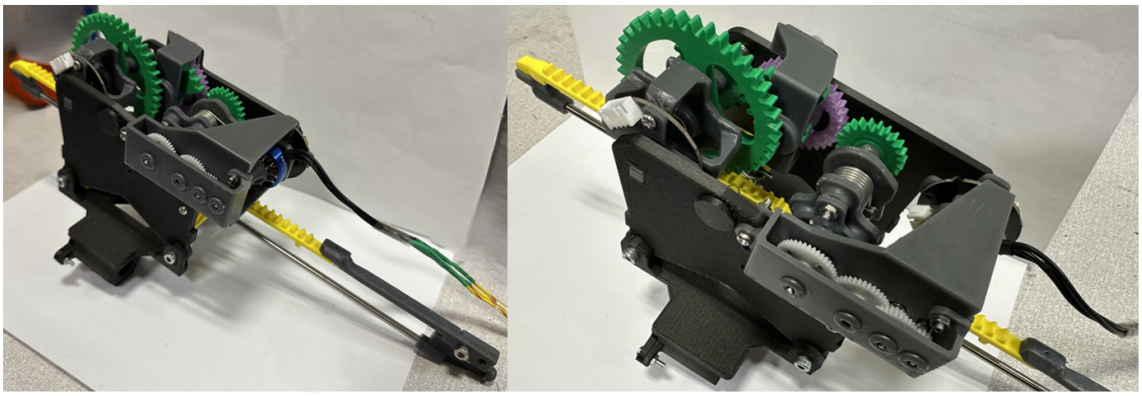

Figure 5.14: The manufactured Ver.3 of the jumper prototype. The picture on the left is an overview and the right one is a more zoomed in view of the jumper from the top.

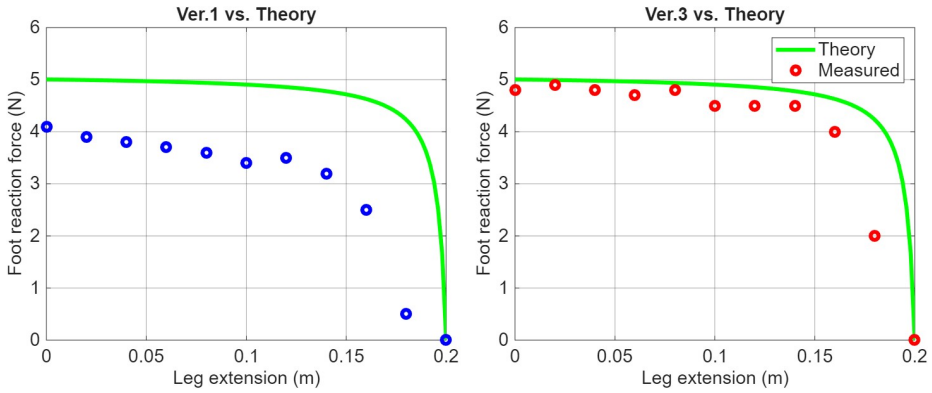

Figure 5.15: Caption

A.8 in Appendix A.

5.6.3 Experiment platform

The experiment platform is shown in Fig. A.9 in Appendix A, which consists of the supporting frame, the guide rods and the sensors. The jumper is constrained by two aluminium guide rods that only allows it to move vertically up and down. There is a load cell underneath the robot leg to measure the ground reaction force during a jump, and the ultrasonic distance sensor on the top measures the height of the jump.

5.7 Chapter summary

This chapter introduced a CVT enhanced SEA jumping mechanism. The simulation results shows that the C-SEA manages to produce nearly constant ground reaction force than the regular SEA and almost halves the peak ground reaction force sacrificing the time taken to accelerate. The reduced ground force is beneficial to the structural integrity and means less material requirements for the end-effector; it could also be useful when the robot needs to locomote on soft surfaces that might be unstable under high pressure. At the same time, when actuated by a realistic motor, C-SEA has a clear advantage. It outperforms the SEA in terms of achieving high jumps because of the C-SEA's ability to compress the spring more thoroughly even when the charging stage is extended. The mechanical design for the CVT gearbox also yielded great results with NC gear set being chosen for the task. The NC gear set have varying gear ratio lead by its own internal mechanical properties and positive engagement for better torque transmission. The jumper prototyping process took three iterations with the final results fit the design criteria.

Following the jumper mechanism design, we will dive into the full robot integration in the next chapter. The compatibility, functionality and agility of the jumping robot

incorporating the C-SEA leg and AeroTail balancer will be demonstrated in the form of simulation studies. New dynamic model and control strategy will be introduced to fit the planar jumping robot. Its advantages over other conventional counterparts will also be showcased.

Chapter 6

AeroTail Enhanced C-SEA Jumping Robot

Following the development of the balancing and jumping mechanisms in the previous chapters, a planar monopedal jumping robot, able to perform high and continuous jumps, is introduced in this chapter by combining the jumper and the balancer. This chapter covers the theoretic basis for robotic jumping locomotion as well as simulation studies to analyse the performance of such robot.

6.1 Theoretic basis for robotic jumping

The standard dynamic model used for jumping and hopping robots is usually the SLIP (Spring-loaded Inverted Pendulum) model [110]. In this model, the robot is seen as a point mass with a massless leg underneath it; the leg can contract and extend linearly and exert force in a elastic manner, hence the name. This section will cover the mathematical model of the SLIP dynamics and control strategies to achieve continuous robotic jumping and locomotion [129].

6.1.1 The SLIP model

When robot jumps, it inevitably has a stance phase (when leg is touching the ground) and a flight phase (when robot is in mid-air); robot in a SLIP context is no exception. when the robot is locomoting through jumping, it transitions between the two phases. The transition from flight to stance is called a touch-down and that from stance to flight is called take-off.

Fig. 6.1 shows the SLIP dynamics during the stance phase. The robot centre of mass (CoM) travels at the velocity of v_{td} ("td" stands for touch-down) with a angle of ϕ_{td} relative to the upright position. Assume the leg orientation is collinear to the

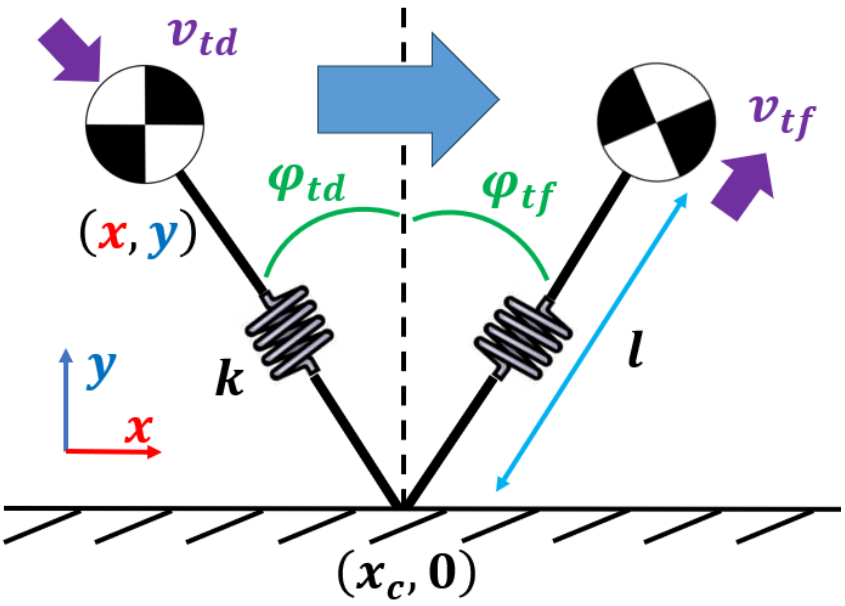

Figure 6.1: The SLIP model during stance phase. v_{td} is the touch-down velocity and v_{tf} is the take-off velocity. k is the spring constant of the leg whose length is represented by l.

direction of v_{td}, the leg makes contact with the ground at point $(x_c, 0)$ ("c" stands for contact) with attach angle ϕ_{td}. The CoM then moves forward as the leg spring first compresses and expands. Eventually, the robot takes off at the velocity v_{tf} with leg orientation ϕ_{tf}.

Assume at the moment of touch-down, the position of the CoM is (x, y), have the equations:

$$\begin{aligned} y - l_0 \cos\phi &= 0 \\ x + l_0 \sin\phi &= x_c \end{aligned} \tag{6.1}$$

where l_0 is the resting length of the leg. The force exerted by the leg spring (F) is calculated from:

$$F = k(l - l_0)$$

where k is the spring constant, l and l_0 are the current and resting lengths of the leg. Take-off happens when the ground reaction force of the robot drops to zero. In this case, the ground reaction force is equal to leg spring force F, thus the robot takes off when $l = l_0$. We can have the relation:

$$l = \sqrt{(x - x_c)^2 + (y - 0)^2} \tag{6.2}$$

where x and y are now the instant position of the CoM. Then, we can begin to obtain

the equations of motion (EoM) using Lagrangian dynamics:

$$\frac{d}{dt}(\frac{\partial L}{\partial \dot{\boldsymbol{q}}_{\boldsymbol{j}}}) - \frac{\partial L}{\partial \boldsymbol{q}_{\boldsymbol{j}}} = \boldsymbol{Q}_{\boldsymbol{i}}. \tag{6.3}$$

where $\dot{q_j}$, q_j and Q_j are the velocity, position and external forces in the vector form. The Lagrangian is $L = T - V$ where T is the kinetic energy and V is the potential energy. They can be expressed as:

$$\begin{aligned} T &= \frac{1}{2}mv^2 = \frac{m}{2}(\dot{x}^2 + \dot{y}^2) \\ V &= mgy + \frac{1}{2}k(l - l_0)^2 \end{aligned} \tag{6.4}$$

where m is the mass of the robot, g is gravity, $\dot{x}$ and $\dot{y}$ are the horizontal and vertical components of the velocity v. Since l can be further expanded using (6.2), V can be alse written as:

$$V = mgy + \frac{1}{2}k(\sqrt{(x - x_c)^2 + y^2} - l_0)^2. \tag{6.5}$$

It is assumed that there is no external forces or energy lost, thus $Q_i = 0$. By plugging (6.4) and (6.5) into (6.3), we get the EoMs of the system:

$$\begin{aligned} m\ddot{x} &= k(\sqrt{(x - x_c)^2 + y^2} - l_0)\frac{(x - x_c)}{l} \\ m\ddot{y} &= k(\sqrt{(x - x_c)^2 + y^2} - l_0)\frac{y}{l} - mg \end{aligned} \tag{6.6}$$

during the stance phase. As for the flight phase, the robot is simply in free fall. Thus the flight EoMs are $m\ddot{x} = 0, m\ddot{y} = g$.

In this classic SLIP model, as long as the direction of v_{td} is collinear with the leg orientation, the stance dynamics is symmetrical about $(x_c, 0)$, meaning:

$$\begin{aligned} \phi_{tf} &= -\phi_{td} \\ \dot{x}_{tf} &= \dot{x}_{td} \\ \dot{y}_{tf} &= -\dot{y}_{td} \end{aligned} \tag{6.7}$$

and if we make sure the leg attack angle during touch-down equals to that of the last jump, the horizontal take-off velocity of every jump thus the speed of locomotion theoretically remains constant. However, the assumption about leg orientation is not always true; when this condition is not met, the stance dynamics becomes asymmetrical. This will be discussed in detail in the next section.

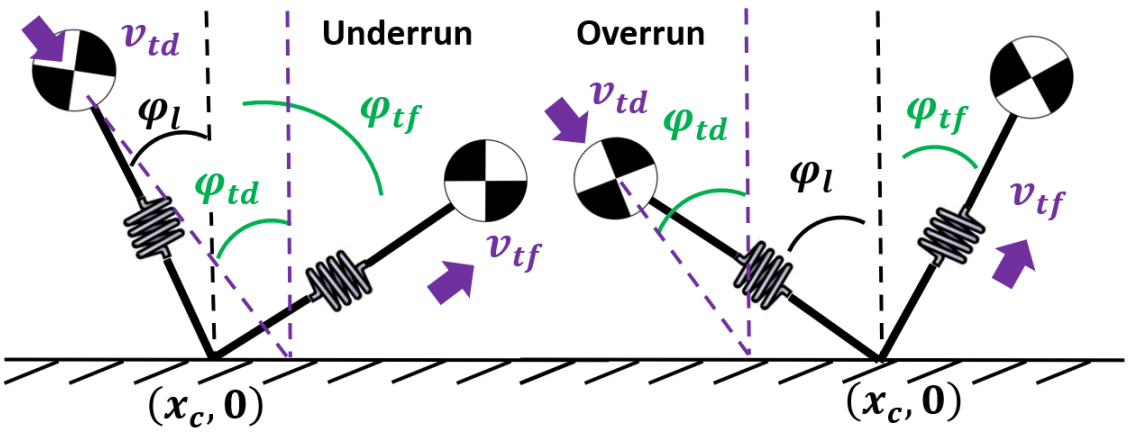

Figure 6.2: This is a demonstration of what the foot placement affect the take-off angle.

6.1.2 Foot placement control

We have established the basic robot jumping dynamics according to the SLIP model, the logical next step is to figure out how to manipulate the speed and height of the jumps. Fig. 6.2 proposes an alternative scenario to the standard SLIP model in which the foot (contact point between the leg and the ground) is placed behind or in front of the original symmetry point. This is due to a mismatch between the direction of touch-down velocity ϕ_{td} and the leg orientation ϕ_l. The symmetrical nature of the stance phase dynamics is only maintained by the condition $\phi_{td} = \phi_l$. The direct result of the mismatch is that the take-off velocity and its angle differs from the touch-down one. When the foot is place behind the symmetry point, it is called underrun; when it is in front of the symmetry point, it is called overrun. An underrun causes ϕ_{tf} to be larger than ϕ_{td} and an overrun leads to the opposite; more specifically, underrun causes $\dot{x}_{tf} > \dot{x}_{td}$ and overrun leads to $\dot{x}_{tf} < \dot{x}_{td}$. Therefore, foot placement can enable the robot to accelerate or decelerate.

This idea is used in the Raibert's controller in which the control loops for height and speed are separate and leg orientation during touch-down is manipulated to control the horizontal velocity of take-off thus the locomotion speed [104]. The Raibert's controller utilises a simplified version of the SLIP model which introduces the oscillation period T_p as a constant. Since robot mass m and leg spring constant k are known, the robot during stance phase can indeed be seen as a spring-mass system whose period can be calculated as:

$$T_p = 2\pi\sqrt{\frac{m}{k}}. \tag{6.8}$$

Raibert then made an assumption stating the time interval from touch-down to take-

off is roughly half of the oscillation period T_p:

$$\Delta T_p = \pi\sqrt{\frac{m}{k}} \tag{6.9}$$

where ΔT_p is the stance duration. From here, an equation can be written based on the horizontal distance travelled by the CoM during stance:

$$2l\sin\phi_{td} = \dot{x}_{td}\Delta T_p \tag{6.10}$$

assuming symmetrical behaviour. This means the touch-down angle can be expressed as a function of the horizontal velocity:

$$\begin{aligned}\phi_{td} &= \sin^{-1}(\frac{\dot{x}_{td}\Delta T_p}{2l}) \\ &= \sin^{-1}(\frac{\dot{x}_{td}\pi}{2l}\sqrt{\frac{m}{k}}).\end{aligned} \tag{6.11}$$

As mentioned before, the locomotion speed control can be achieve by manipulating the leg orientation during touch-down, thus the controller can be written as:

$$\phi_{l,i} = \phi_{td,i} + \phi_{correction} \tag{6.12}$$

where i is the "jump index"; here it simply means the current jump. Plugging in (6.11) we get:

$$\phi_{l,i} = \sin^{-1}(\frac{\dot{x}_{td}\pi}{2l}\sqrt{\frac{m}{k}}) + K(\dot{x}_{des} - \dot{x}_{td}) \tag{6.13}$$

where $\dot{x}_{des}$ is the desired horizontal velocity and K is the control gain.

6.2 Simulation study

In this section, a comparative simulation study involving a planar monopedal jumping robot is introduced. There will be cross comparisons between the performances of C-SEA, SEA, AeroTail, and RWs as the jumping and balancing mechanisms respectively. The main purpose of the simulation study is to demonstrate the compatibility and functionality of a jumping robot that combines the aforementioned jumpers and balancers that were introduced as separate devices in the previous chapters. At the same time, the simulation also serves as the validation and visualisation for the advantages of AeroTail and C-SEA leg over their conventional counterparts.

Simulation Environment selection

The integrated simulation environment is implemented in PyBullet, a real-time rigid-body physics engine with native URDF support. Compared to block-diagram-based multi-domain environments such as Simulink/Simscape Multibody, a URDF-described articulated rigid-body framework enables more direct specification of inertial properties, joint constraints, and actuator structure in a format closely aligned with robotic system descriptions. The separation between physical and visual representations, together with script-based parameter control, facilitates rapid design iteration, transparent debugging, and efficient modification of mass distribution and joint configuration. PyBullet further provides stable contact handling and collision resolution, which are essential for modelling impulsive ground contact during jumping.

However, PyBullet does not include native aerodynamic or fluid-dynamics modelling. As a result, aerodynamic effects are represented through equivalent torque terms rather than direct flow simulation. While this abstraction is sufficient for evaluating rotational stabilisation trends, it does not capture full fluid–structure interaction or translational aerodynamic effects. Higher-fidelity alternatives, such as CFD–rigid-body co-simulation using ANSYS Fluent or OpenFOAM, fluid–structure interaction modelling in COMSOL Multiphysics, or robotics simulators extended with aerodynamic plugins (e.g., Gazebo or MuJoCo with external aerodynamic modelling), could be explored in future work to more accurately capture coupled aero-mechanical behaviour.

6.2.1 Assumptions regarding aerodynamics

It should be noted that the integrated PyBullet model does not explicitly simulate fluid dynamics. Since PyBullet does not provide native aerodynamic modelling, the effect of the AeroTail is represented using an equivalent aerodynamic torque $\tau(\omega_t)$ applied about the body pivot, expressed as a function of the tail angular velocity. This formulation captures the dominant rotational drag-induced moment used for stabilisation, while avoiding computationally expensive flow simulation. Forward translational aerodynamic effects on the robot body and tail are not explicitly included in the model. As a result, the simulation focuses on rotational stabilisation and reorientation dynamics and provides an approximate representation of the aerodynamic contribution rather than a full fluid–structure interaction model.

Effects of forward translation

When forward body translation is considered, the aerodynamic torque can be intuitively approximated using a blended velocity term of the form $\tau \approx \frac{1}{2}\rho\, C_d(Re)\, A\, (\omega r \pm$

$V_{\text{forward}})^2 r$, which suggests that forward velocity effectively augments or reduces the local relative airspeed depending on the direction of motion. While this indicative expression is useful for conceptual reasoning, the actual aerodynamic interaction is more complex. In practice, when the drag-inducing (DI) frontal area faces the direction of body translation, a drag force acts on the tail centre, whereas when the tail is parallel to the translational direction, the frontal exposure is minimal. As the tail rotates, this produces a periodic, orientation-dependent force component acting on the centre of mass, whose magnitude scales with the forward velocity.

This behaviour introduces a potential DI design trade-off: minimising frontal area reduces unwanted translational drag forces and associated oscillatory disturbances, while maximising aerodynamic torque favours larger effective area and moment arm. Similarly, although increased effective relative velocity may imply higher torque at a given angular speed, implementing a tail-position-dependent controller gain would be impractical at the high rotational speeds typically used. Instead, control strategies should aim to ensure robustness against the velocity-induced oscillatory disturbance rather than attempting real-time gain modulation.The coupled influence of forward body speed and the corresponding mitigation strategies represent a non-trivial, multi-parameter problem and constitute a research topic in their own right. A comprehensive treatment of these effects is therefore beyond the scope of the present simulation study and is identified as part of future work.

6.2.2 Robot model integration

The integrated jumper-balancer robot consists of a robot body, a leg link underneath it connected by a prismatic joint and a balancer link on its side connected by a revolute joint. This can be easily expressed by a kinematic tree in the URDF file. The first step of preparing for the simulation is transferring usable simulation setups from MATLAB to Pybullet. Unlike MATLAB, Pybullet has its own physics engine, which makes the CVT gearbox modelling difficult since the built-in tools for mechanical system design are not powerful enough to generate realistic results. Thus, a method called "severed robot" is introduced to tackle this issue. We modeled the robot into two "bodies" (kinematic trees): one for the internal system and the other for the external one. The internal system modelling is done using a software block bypassing Pybullet's built-in physics engine, while the external system calculations are done using the physics engine-based functions. For the AeroTail, a major challenge facing the robot modelling needs to be solved as well, namely, Pybullet cannot simulate fluid dynamics. The solution is that we see the aerodynamic effect as a single equivalent torque acting on the mid-point of the tail (also on the CoM of the robot) and the

equivalent torque is a function of the tail's angular velocity. Additionally, since the default simulation setting for Pybullet is a 3D GUI and we are simulating a planar jumping robot, the robot's motion needs to be restricted into the 2D plane. This is done by using dummy links and extra joints between the robot body and the "world" link, which confines the robot to a 3 DoF plane.

6.2.3 Controller

Following the introduction to the SLIP dynamic model and the SLIP model-based controller, we have designed our own jumping speed controller that is suitable for our robot model. One critical different between the SLIP model and realistic robotic jumping is that a robot cannot be actuated by only springs, it requires constant energy input to maintain continuous jumping. In our case, the leg spring can be seen as the elastic element in a SEA powertrain and the full dynamic model of the leg mechanism is different from and significantly more complex than the basic SLIP model, but it can be simplified. If look at the equation for the Raibert's controller (6.13), the first term on the right hand side (RHS) is a prediction of the touch-down angle estimated from the horizontal velocity; since the only external force during the flight phase is gravity, the touch-down angle should also be the opposite of the last take-off angle:

$$\phi_{td,i} = -\phi_{tf,i-1} \tag{6.14}$$

where $i-1$ simply means the last jump. In this case, equation (6.13) can be simplified to:

$$\phi_{l,i} = -\phi_{tf,i-1} + K_h(\dot{x}_{des} - \dot{x}_{td}) \tag{6.15}$$

where $\phi_{tf,i-1}$ is measured at take-off of every jump. However, this controller only works under this condition: the stance dynamics is indeed symmetrical. This required the robot to be only actuated by a spring assuming no energy loss, which is, as we discussed, unrealistic. Through testing, we found that if the leg is actuated by a SEA or C-SEA, the robot always experiences a deceleration after each jump even if the condition $\phi_l = \phi_{td}$ is fulfilled. Therefore, the stance dynamics is not symmetrical about the foot contact point. To compensate for this, the ideal touch-angle should be a little larger than $\phi_{tf,i-1}$ to create a underrun. Now the controller's expression can be written as:

$$\phi_{l,i} = -\phi_{tf,i-1} \cdot \sigma_\phi + K_h(\dot{x}_{des} - \dot{x}_{td}) \tag{6.16}$$

where σ_ϕ is called the symmetry factor which "manually" make the stance dynamics symmetrical. In this case, the relation

$$\phi_{tf,i} = -\phi_{td,i} \tag{6.17}$$

holds true and the horizontal velocity is theoretically maintained; then, any error can be fixed by the second term thus achieving jumping speed control. To derive the analytical answer for σ_ϕ would be impractical due to the complexity of the forcing pattern. Instead, the value can be obtained by testing. When the forcing pattern stays constant, a single σ_ϕ can make relation (6.17) true for all initial tilt angle.

6.2.4 Simulation setup

The simulation will see robots with different configurations (combinations of different mechanisms as the leg and the balancer) complete the same task. The task is locomotion by jumping with constant horizontal velocity towards the same direction for 20 seconds. The time duration 20s is chosen because it is long enough for most systems in this scenario to stabilise but too long to avoid redundant data. The internal mechanism and robot parameters remain unchanged for the simulation, only the leg and balancer differ. Like previous chapters, the robot body weighs 100g with a 10g leg and its full extension is 0.2m. The motor model and CVT parameter are identical to the values in **Chapter 5**. There are 4 combinations: "SEA-RW", "CSEA-RW", "SEA-Aero", and "CSEA-Aero"; and for RW there are two mass tiers: 10g and 20g (assuming the inertia is proportional to mass). The performances of each combination is recorded and compared in 3 comparative studies to fully demonstrate the advantages of drawbacks of every mechanisms individually and when they are used in combination.

- Study 1: When both robots use RW as the balancer, their performances from using the SEA and C-SEA as the leg mechanism are compared.
- Study 2: When both robots use traditional SEA as the leg mechanism, their performances from using the RW and AeroTail as the balancer are compared.
- Study 3: A through comparison between a robot combining SEA and RW and a robot integrating C-SEA and AeroTail is conducted. This study also includes a discussion of the specific advantages of using the C-SEA and AeroTail in combination over individually in a jumping locomotion scenario.

The 2-tier system is introduced for the RW because of their inertial nature making their mass values significantly affect the performance of the robot. In this case, it is

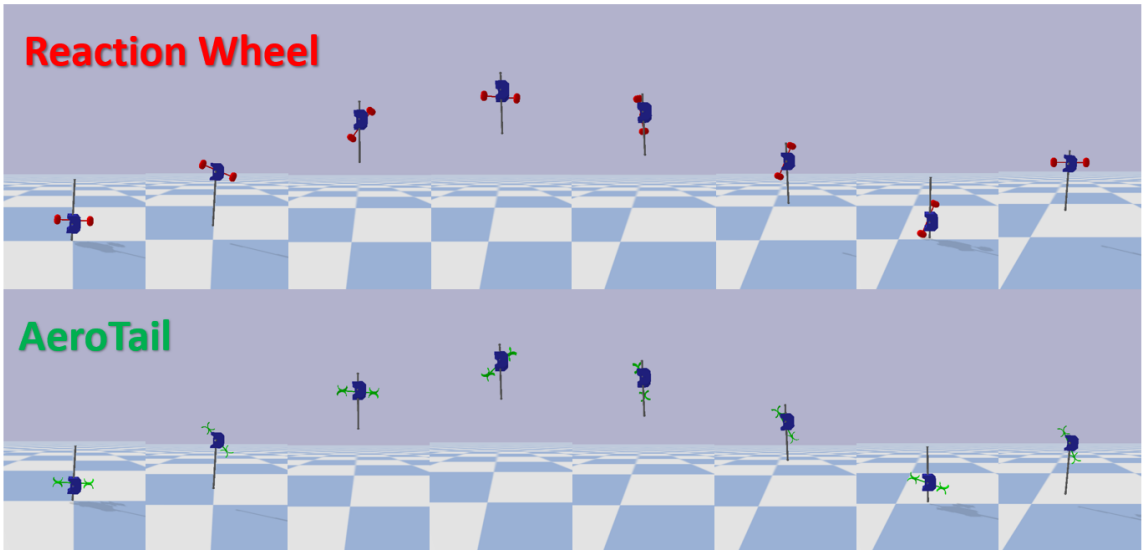

Figure 6.3: This figure include screenshots from the full robot simulations. They show the robot starting with the first jump, completing a flight phase, landing, and completing a stance phase to the second jump. The RW is shown in red and the AeroTail is shown in green.

scientifically meaningful to compare their performances. In the past robot designs, the RW is usually between 10% to 20% of the body mass [112] [19]. Therefore, for a 100g robot, we took a upper and lower bound for the value. For every combination, the motor pre-retraction, σ_ϕ, and K_h that gives stable performances are obtained by trials. The simulation results are demonstrated in the next section.

6.2.5 Simulation results

In this section, the results from each of the 3 studies are illustrated. Fig. 6.3 show screenshots of the simulation in which robots equipped with RW and AeroTail completing a single jump (flight plus stance phase).

Study 1

In study 1, we compare the SEA and C-SEA leg mechanism with the choice of RW balancer as the controller variable thus no AeroTail is examined. However, we do have 2 mass tiers for the RW and they will be compared in this study. First of all, a straightforward comparison between the ground reaction forces (GRF) experienced by the SEA and C-SEA robots are shown in Fig. 6.4. Comparisons are made within their own mass tiers. We can easily see the difference peak ground reaction forces when CVT is included. In a single jump, the shape of the GRF curve for the SEA leg is "shape" and has a high peak value while that of the C-SEA is more evened out forming a little "plateau" at the peak. The average peak GRF can be found in Table

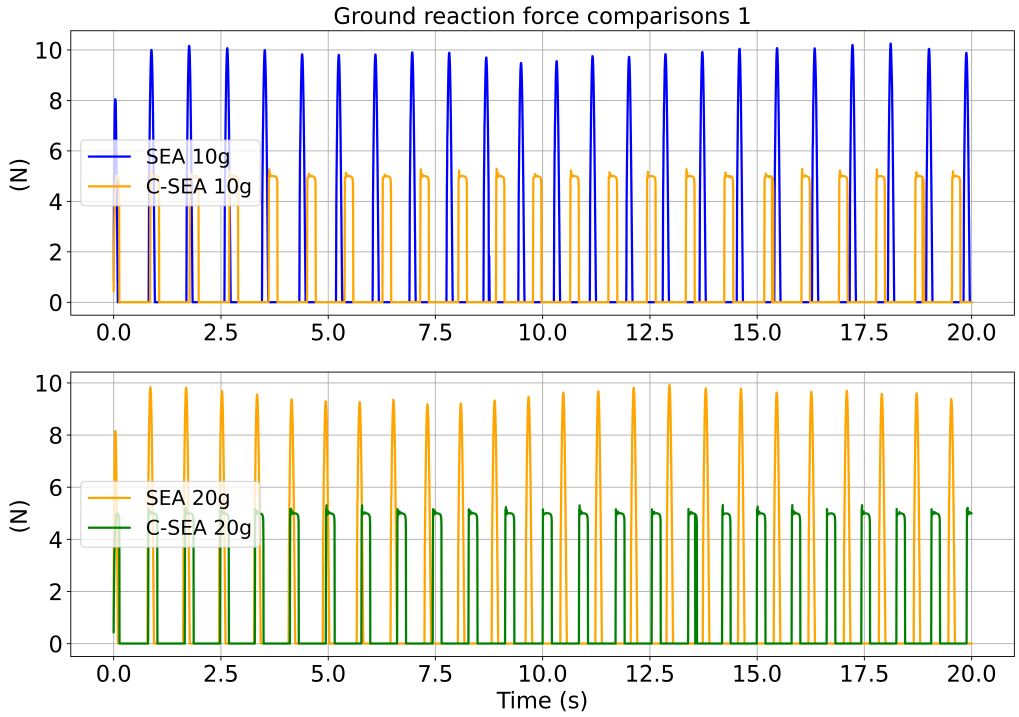

Figure 6.4: Ground reaction force comparisons between SEA and C-SEA leg mechanisms from the 10g tier are shown in top plot and those from the 20g tier are shown in the bottom plot.

6.2. For the 10g tier, SEA have a average peak GRF of 9.514N, C-SEA has 5.156N which roughly halves the former value. The same observation can be made for 20g tier.

The jumping heights for some of the configurations are shown in Fig. 6.5. The height reached by the C-SEA during the run time roughly matches that of the SEA which is slightly advantageous towards the end. In the previous chapter, we have established that the C-SEA can reach higher vertical jumps with fully charged leg than SEA. This observation still holds true here since in the first jump, the height reached by C-SEA is still better. However, this advantage does not carry over to continuous jumping. The reason is likely the imperfection (used to avoid mathematical invalidity) in the pitch curve of the NC gear set, which induces a small energy loss. That being said, the average apex height for C-SEA is 0.776m, only 4.1% smaller than the 0.809m of the SEA. This sacrifice is worthwhile for the 45.8% reduction of the peak GRF. As expected, robot with the same leg mechanism jumps higher when equipped with the 10g RW since the overall mass of the robot is lower. For C-SEA, the average apex is 0.677 for the 20g tier, 16.3% lower than the 10g tier.

The next metric to compare is the energy consumption. When the robots use the same motor with same voltage input, a lighter robot naturally achieves a better take-off velocity and thus higher jumps. Another pro for a lighter robot is that less energy

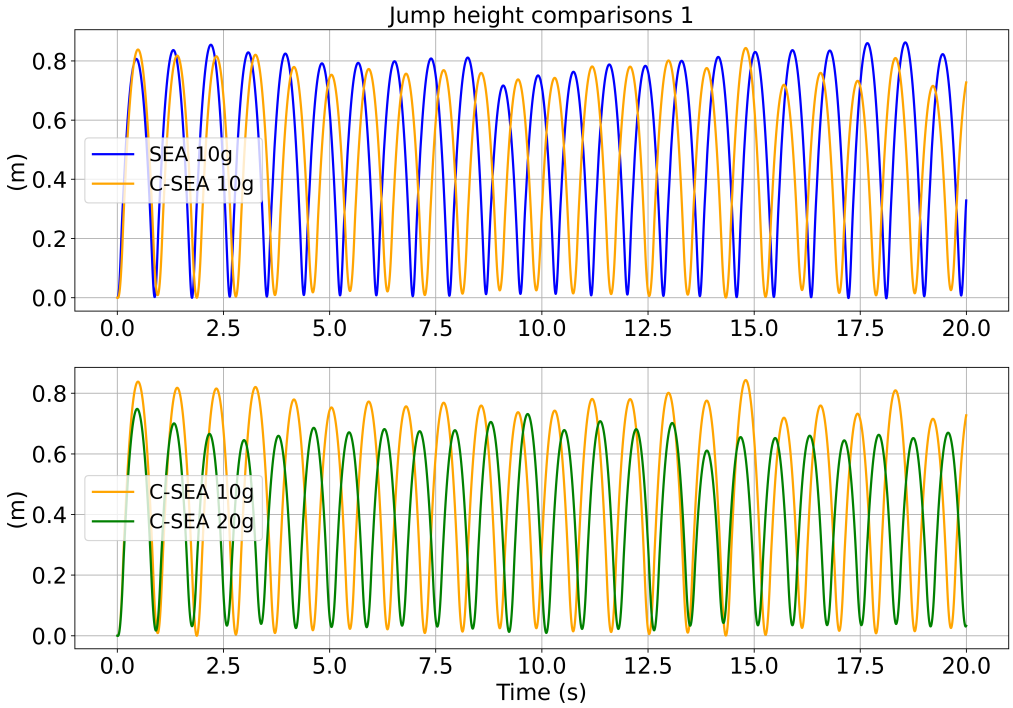

Figure 6.5: The top plot compares the jump height of robots with different leg mechanism but from the same mass tier. The bottom plot compares the two mass tiers but both use C-SEA legs.

is required to reach the same jump height. One source for this weight reduction is the RW which required inertia to function. In this part of the study, we examine the effects of this attempted mass reduction by reducing the weight of the RW. Fig. 6.6 demonstrates the mechanical power output from the leg and balancer motors. The total energy consumed can be calculated from the area under the plots. For the leg mechanism, the 10g tier costs 6.763J of energy during the run time, which is expectedly lower than the 6.860J for the 20g tier. However, the energy consumption for the balancer rises from 0.403J to 0.608J, a 50.9% increment. This is due to the fact that lighter RWs experience higher acceleration when providing the same correcting torque, giving them a higher angular velocity during the run time. In this case, the overall energy consumed by the 20g tier robot is 7.263J, outperforming the 7.371J of the 10g tier even though the latter has smaller mass.

Study 2

Study 2 introduces comparisons between the RW and AeroTail as individual devices in a jumping locomotion scenario. Therefore, the leg mechanism is the controlled variable and only SEA are used. The first observation we made is that the AeroTail requires less motor effort for the same task. An average torque input of only 1.578 $\times$

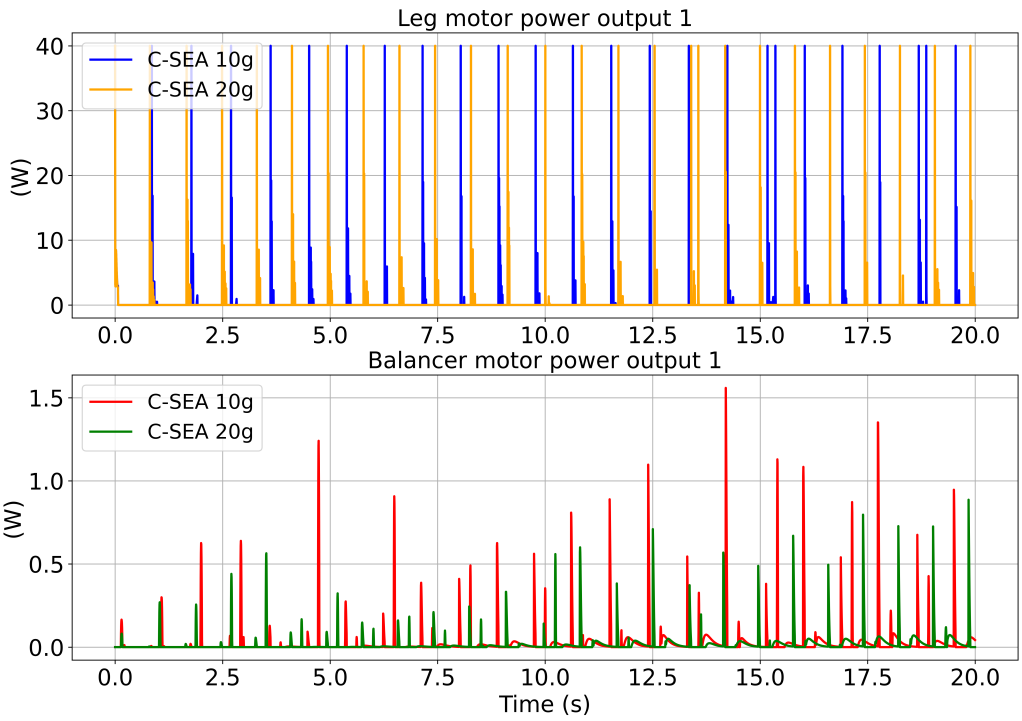

Figure 6.6: The power output comparison between the mass tiers for leg motor and balancer motor are shown in the top and bottom plots respectively. Only the C-SEA is used in this figure.

Table 6.1: The average balancer torque input comparison

Robot Config.	SEA & RW10g	SEA & RW20g	SEA & AeroTail
Balancer effort (Nm)	1.728×10^{-3}	1.699×10^{-3}	1.578×10^{-3}

10^{-3}Nm is observed for the AeroTail compared to the 1.728×10^{-3}Nm and 1.699×10^{-3}Nm for the RWs (10g tier and 20g tier respectively).

The power output of the motors are compared in 6.7. Again, from the power plot we can calculate the total energy consumption of the motors during run time. We found that the AeroTail consumes more energy (0.967J for AeroTail and 0.950J for the 10g RW) yet the leg motor on the robot with the AeroTail has lower energy consumption then the RW (5.739J for AeroTail and 6.117J for the 10g RW). The extra energy required for the AeroTail is from the acceleration process before reaching the target angular velocity since the AeroTail's torque generation depends on its speed unlike the instantaneous impulse of the RWs. In previous chapters, we have established that the AeroTail can be energy efficient when the correction angle is large or constant torque needs to be maintained; because in that case, having a dependent angular velocity mean lower average speed thus less energy requirement. This advantage does not carry over to the continuous jumping robot scenario. That

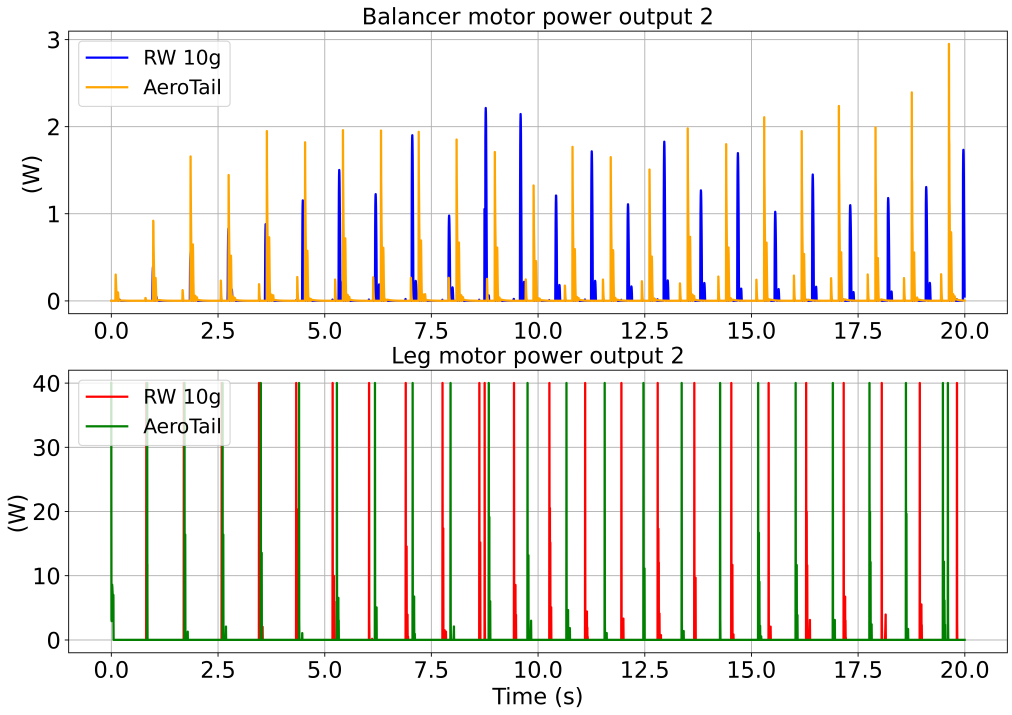

Figure 6.7: The power output comparison between the AeroTail robot and RW 10g robot for balancer motor and leg motor are shown in the top and bottom plots respectively.

being said, the lightweight AeroTails reduces the overall mass compared to the RW and the leg motor energy consumption decreases. This leads to the overall energy consumed by the AeroTail robot being 6.706J, outperforming the 7.07J of RW by 5.4%.

As we have mentioned that the AeroTail takes time to accelerate to the target speed in order to generate correction torque, the delay in AeroTail's response could theoretically compromise the performance stability. However, this is not true in the robot jumping locomotion scenario and we have found a straightforward to quantify the stability of locomotion. Because of the nature of serial-elastic jumping, the take-off angle and thus horizontal velocity of the robot can differ a lot if the touch-down angle is off due to the balancer not converging in time. Therefore, an underperforming balancer could lead to the horizontal velocity varying significantly from one jump to another. In Table 6.3, we calculated the standard deviations(σ) of the horizontal velocity for all robot configurations. We found that the AeroTail robot actually has a smaller $\sigma = 0.084$ than its RW counterparts who have 0.114 (for 10g tier) and 0.137 (for 20g tier). This proves that the AeroTail's response delay is negligible for the task. It is more than capable of re-orient the robot body in time of the touch-down and is a complete viable replacement for the RW in this scenario in terms of stability.

Table 6.2: Simulation results: averages and sums of the plotted values.

Robot Config.	GRF (N)	Apex Height (m)	Leg energy (J)	Balancer energy (J)
SEA & RW10g	9.514	0.809	6.117	0.950
SEA & RW20g	9.504	0.712	6.507	0.629
C-SEA & RW10g	5.156	0.776	6.763	0.608
C-SEA & RW20g	5.185	0.677	6.860	0.403
SEA & AeroTail	9.795	0.864	5.739	0.967
C-SEA & AeroTail	5.114	0.860	5.703	1.017

Table 6.3: Stability: average velocity and standard deviation.

Robot Config.	Horizontal velocity (m/s)	Standard Deviation (σ)
SEA & RW10g	0.606	0.114
SEA & RW20g	0.555	0.137
C-SEA & RW10g	0.634	0.247
C-SEA & RW20g	0.620	0.172
SEA & AeroTail	0.550	0.084
C-SEA & AeroTail	0.606	0.205

Study 3

In the final study, we compare Robot-A with SEA and RW (20g tier) to Robot-B with C-SEA and AeroTail in term of all relevant metrics mentioned before to examine the general advantages of using the C-SEA and AeroTail in combination. In Fig. 6.8, the plots for ground reaction force, jump height, leg motor and balancer motor power output are shown. As expected, the average peak GRF of Robot-B is 5.114N, halving the 9.504N of Robot-A. The average apex height for Robot-B is 0.860m, which outperforms the 0.712m for Robot-A. Even though the C-SEA has a slight height disadvantage during repetitive jumping, the robot being overall lighter helps to improve the jump height. For energy consumption, having the AeroTail increases the balancer's own consumed from 0.629J to 1.017J but also manages to cut down the leg motor consumption from 6.507J to 5.703J. Overall, the energy consumed by Robot-B is 6.72J, which outperforms the 7.136J of Robot-A by 6.2%. Further ablation that compare the performance of all other jumper-balancer combinations can be found in Section A.2 in Appendix.A.

The results in study 3 reveals the advantages of using AeroTail and C-SEA in combination that are not clear in previous studies. For example, the reduced mass due to the lightweight nature of the AeroTail overwrites the jump height disadvantage of the C-SEA. Furthermore, when the robot's overall energy consumption is in question, the extra energy consumed by the AeroTail alone can be overlooked. To summarise, the Robot-B that is equipped with C-SEA and AeroTail have significant advantages

in terms of jump height, ground reaction forces and energy consumption.

6.2.6 Monte-Carlo sensitivity study

Setup

A light Monte Carlo analysis ($N \approx 200$ per case) was conducted to assess parametric sensitivity of the closed-loop hopping system under bounded uncertainty. Three perturbation scenarios were considered:

1. **All parameters scaled:** aerodynamic coefficients (C_d, air density ρ, DI area A) and controller gains (K_p, K_d, K_h) simultaneously scaled by $\pm 10\%$. Note that K_p and K_d are the gains for body angle re-orientation and K_h is the velocity gain in (6.16).
2. **Aerodynamic-only scaling:** C_d, ρ, and A scaled by $\pm 10\%$ while controller gains remained nominal.
3. **Controller-only scaling:** K_p, K_d, and K_h scaled by $\pm 10\%$ while aerodynamic parameters remained nominal.

For each trial, simulation was executed for a fixed horizon and classified as successful if these following conditions are met during run time.

- The robot does not tip over or fall to the ground.
- The jumping is continuous and does not terminate prematurely.
- Only forward translation occurs with no backward jumping or hovering.

This Monte-Carlo study uses the (C-SEA & AeroTail) combination and it has two outputs: the success rate according to the criteria above, and $\bar{\sigma}$, which is the standard deviation of jumping velocity taken average across all the samples.

Results

Table 6.4: Monte Carlo results under $\pm 10\%$ parameter scaling.

Scaling Scenario	Success Rate (%)	$\bar{\sigma}$(m/s)
All parameters scaled	78.5	0.229
Aerodynamic only	86.0	0.240
Controller gains only	84.5	0.238

The results for $\pm 10\%$ scaling are summarised in Table 6.4. Several observations can be made. First, success rates remain above 75% in all cases, indicating that the closed-loop system retains a substantial practical region of attraction under moderate parametric variation. This confirms that the controller achieves reliable task execution in the neighbourhood of the nominal design point.

Second, aerodynamic-only and controller-only perturbations yield comparable performance, with only modest changes in $\bar{\sigma}$. This suggests that neither aerodynamic uncertainty nor gain variation alone dominates the closed-loop behaviour at the $\pm 10\%$ level. Instead, performance depends on the coupling between aerodynamic drag torque magnitude and feedback gain selection.

Third, simultaneous scaling of both aerodynamic parameters and controller gains results in a slightly reduced success rate compared to individual perturbations. This reflects the non-linear interaction inherent in the hybrid flight–impact dynamics: scaling gains modifies the effort of attitude regulation, while scaling aerodynamic parameters alters flight-phase damping and torque generation. The combined effect shifts the closed-loop limit cycle and reduces the effective basin of attraction relative to the isolated perturbations.

Importantly, the controller was tuned for nominal task execution, namely, sustained forward hopping with attitude regulation, rather than worst-case robust stability. The Monte Carlo analysis therefore characterises sensitivity rather than guaranteeing global parametric robustness. The observed reduction in success rate with increasing uncertainty is consistent with a non-linear underactuated hybrid system possessing a finite region of attraction rather than global stability margins. Enhancing robustness through gain scheduling, adaptive estimation of aerodynamic coefficients, or structured robust control synthesis remains an avenue for future work.

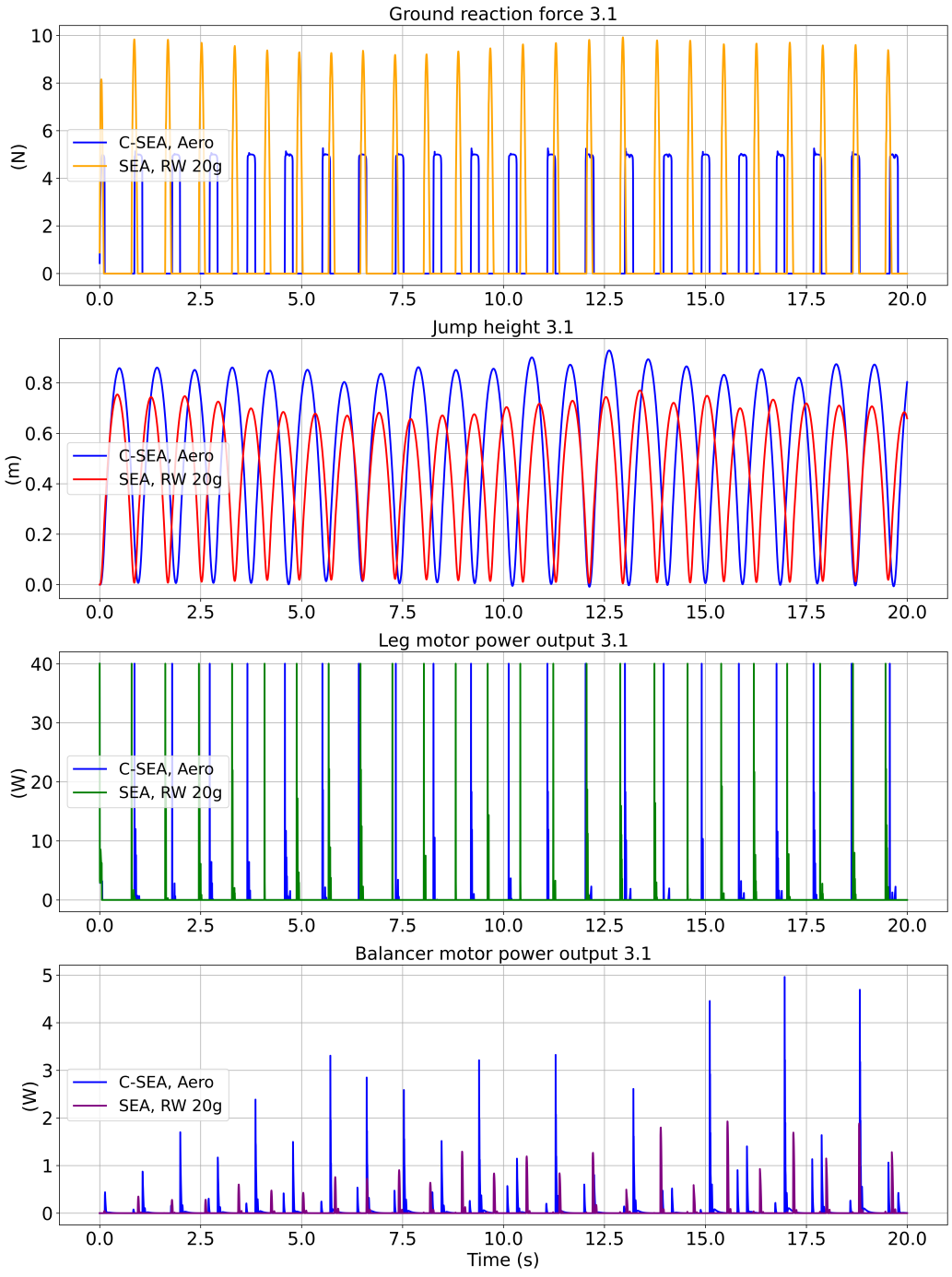

Figure 6.8: The ground reaction forces, jump heights, leg motor and balancer motor power outputs are compared in this figure between Robot-A and Robot-B. Note that Robot-A is with SEA and RW 20g and Robot-B is with C-SEA and AeroTail.

Chapter 7

Conclusion

7.1 Summary of the project

This PhD project answers the question "How can the aerodynamic drag-inducing tails and mechanical advantage-varying knee joints of mammals inspire improvement in the agility and precision of jumping robots?" by designing a bioinspire agile jumper robot that features a C-SEA leg and an AeroTail balancer. In order to design such robot, extensive literature review is conducted on topics including bioinspired legged robots, jumping robots and robotic balancing to fully explore the ideas and to gain insights. Then, the theoretical AeroTail and C-SEA leg are conceptualised based on the inspirations from natural organisms as well as research gaps in related areas of study. The contributions and results of this project are summarised in this section.

Key Validated Outcomes

The main quantitative outcomes validated through modelling, simulation, and experimental studies in this thesis are summarised as follows:

- The proposed aerodynamic drag-based balancing mechanism (AeroTail) achieves stabilisation performance comparable to reaction-wheel-based approaches while reducing the peak required balancing torque by approximately 33.2%.
- Optimisation of the drag-inducing components demonstrates that the aerodynamic torque generated by the AeroTail can be increased by up to approximately 20.8% through appropriate geometric configuration and connection design.
- The continuously variable transmission enhanced series elastic actuator (C-SEA) enables substantial reduction in peak ground reaction force during jumping compared to a conventional series elastic actuator, while maintaining comparable jump height and overall jumping performance.

- When the jumping and balancing mechanisms are integrated, the resulting robotic system achieves stable jumping behaviour with an overall reduction in system energy consumption of approximately 6.2%, without compromising stability or jumping height.

AeroTail balancer

We formulated a simplistic mathematical model based on the inverted pendulum and control methods suitable for the AeroTail and did computational simulations and comparative studies to quantify and visualise the advantages of the AeroTail mechanism over traditional RW based tails. The lightweight nature of the AeroTail allows it to maintain a low increase in peak motor torque output as the robot body mass increases, achieving a 33.2% reduction compared to RW. Additionally, AeroTail does not even require mass and inertia to function, whereas RW tail experiences dramatically high energy consumption with a low tail-to-body mass ratio.

Drag-inducer optimization study

To design the drag-inducing devices on the AeroTail, we conducted a specialised CFD simulation study on a selection of shapes to explore how specific geometric features influence aerodynamic drag. This study reveals that among the evaluated shapes, DIs with slender frontal surfaces, arch-like profiles and closed ends generally yield higher drag coefficients. Moreover, with the current frame structure, maximising frontal area is the most reliable approach to optimise drag force. The findings from this study lead to an optimisation framework to identify the optimal frame design that maximises aerodynamic drag while adhering to predefined constraints such as weight and dimensional limits. The findings are then validated by experiments, and the DI prototypes are tested in practical scenarios. The experimental results confirms that most torque is generated by DI with a semi-cylindrical film with the optimised orientation outperforming the original by 20.8%.

C-SEA leg mechanism

A CVT enhanced SEA leg is designed and manufactured to be jumping mechanism of the robot. The theoretical innovation in this study consists of mathematical models for the hopping robot powertrain, including the CVT gearbox and a simplified model for an electric motor powered prismatic actuator suitable for iterative simulation. Comparative studies are done to examine the performances of both C-SEA and SEA in various scenarios. The results indicate that the C-SEA manages to reduce the peak ground reaction force by approximately 50% compared to the regular SEA. Moreover,

C-SEA demonstrates superior performance in most cases with higher m_2 and k_m when actuated by a motor with linear behaviour. The leg mechanism prototype utilises a rack-and-pinion transmission to transfer rotation to linear motion, a torsion spring enabled elastic element, and a non-circular gear based CVT element.

Integrated planar jumping robot

The integrated robot featuring a C-SEA jumping mechanism and an AeroTail balancing mechanism is put to test in the form a simulation study using the software PyBullet. A SLIP based dynamics model is used to describe the jumping locomotion of this robot and appropriate control strategy is implemented so the simulated robot can achieve constant speed jumping locomotion. The simulation results verifies that the AeroTail and C-SEA performances largely coincide with the observations and conclusion from previous chapters in which they are studies individually. At the same time, new findings have been made proving when the C-SEA and AeroTail are used in combination, they manage to overcome each other's limitations. For example, the overall robot energy consumption for Robot-B in **Chapter 6** is cut down by 6.2% even though the AeroTail itself consumes more energy.

7.2 Further works

There are several future research works planned that are not within the scope of this PhD project but are the logical next steps to advance the research.

Jumping mechanism experiment

Even though the jumper prototype has been constructed, experiments are yet to be done to verify the findings in the simulation. The main obstacle at the moment is the motor control system not being able to deliver the required behaviour. When this obstacle is lifted, various tasks can be done on the experiment platform to not only validate the simulation studies but also to demonstrate the functionality of the C-SEA jumping mechanism.

Fully functional AeroTail balancer

The experiment results regarding the AeroTail ID design are obtained from a very controlled laboratory environment that does not entirely reflect the working condition of a jumping robot. Various modifications are still available to be made for the balancer, such as material and motor choice. Furthermore, bi-directional torque-generating capability is required for the AeroTail to be actually used on a jumping

robot. Therefore, research works are planned to advance the AeroTail into a fully functional balancer that are able to achieve robot body re-orientation in a jumping locomotion scenario.

Full robot experiment

Chapter 6 introduced a strategy of integrating the C-SEA and the AeroTail into a jumping robot as well as simulation study to show functionality and its advantages over more conventional designs. In order to validate the simulated results, designing and building a real-life integrated jumping robot and putting it to the test is inevitable. In this case, a more advanced control strategy is needed for the task. This robot could be planar at the early stages but expending it into a 3D jumper that is capable of controlled locomotion and obstacle bypassing is also a possibility.

Bibliography

[1] X. Mo, W. Ge, M. Miraglia, F. Inglese, D. Zhao, C. Stefanini, and D. Romano, "Jumping locomotion strategies: from animals to bioinspired robots," *Applied Sciences*, vol. 10, no. 23, p. 8607, 2020.

[2] M. P. McGuigan, E. Yoo, D. V. Lee, and A. A. Biewener, "Dynamics of goat distal hind limb muscle–tendon function in response to locomotor grade," *Journal of Experimental Biology*, vol. 212, no. 13, pp. 2092–2104, 2009.

[3] S. Burgess, "A review of linkage mechanisms in animal joints and related bioinspired designs," *Bioinspiration & Biomimetics*, vol. 16, no. 4, p. 041001, 2021.

[4] A. Patel and E. Boje, "On the conical motion of a two-degree-of-freedom tail inspired by the cheetah," *IEEE Transactions on Robotics*, vol. 31, no. 6, pp. 1555–1560, 2015.

[5] M. Burrows, "Jumping from the surface of water by the long-legged fly hydrophorus (diptera, dolichopodidae)," *Journal of Experimental Biology*, vol. 216, no. 11, pp. 1973–1981, 2013.

[6] A. M. Shih, L. Mendelson, and A. H. Techet, "Archer fish jumping prey capture: kinematics and hydrodynamics," *Journal of Experimental Biology*, vol. 220, no. 8, pp. 1411–1422, 2017.

[7] F. I. Sheikh, "Towards fast running: Open-loop speed and direction control of a single-legged hopper," in *2013 IEEE/RSJ International Conference on Intelligent Robots and Systems*, pp. 5114–5120, IEEE, 2013.

[8] A. Sayyad, B. Seth, and P. Seshu, "Single-legged hopping robotics research—a review," *Robotica*, vol. 25, no. 5, pp. 587–613, 2007.

[9] V. Zaitsev, O. Gvirsman, U. B. Hanan, A. Weiss, A. Ayali, and G. Kosa, "A locust-inspired miniature jumping robot," *Bioinspiration & biomimetics*, vol. 10, no. 6, p. 066012, 2015.

[10] M. A. Woodward and M. Sitti, "Design of a miniature integrated multi-modal jumping and gliding robot," in *2011 IEEE/RSJ International Conference on Intelligent Robots and Systems*, pp. 556–561, IEEE, 2011.

[11] M. A. Woodward and M. Sitti, "Multimo-bat: A biologically inspired integrated jumping–gliding robot," *The International Journal of Robotics Research*, vol. 33, no. 12, pp. 1511–1529, 2014.

[12] G.-P. Jung, C. S. Casarez, S.-P. Jung, R. S. Fearing, and K.-J. Cho, "An integrated jumping-crawling robot using height-adjustable jumping module," in *2016 IEEE International Conference on Robotics and Automation (ICRA)*, pp. 4680–4685, IEEE, 2016.

[13] J. Burdick and P. Fiorini, "Minimalist jumping robots for celestial exploration," *The International Journal of Robotics Research*, vol. 22, no. 7-8, pp. 653–674, 2003.

[14] R. Armour, K. Paskins, A. Bowyer, J. Vincent, and W. Megill, "Jumping robots: a biomimetic solution to locomotion across rough terrain," *Bioinspiration & biomimetics*, vol. 2, no. 3, p. S65, 2007.

[15] A. L. Brill, A. De, A. M. Johnson, and D. E. Koditschek, "Tail-assisted rigid and compliant legged leaping," in *2015 IEEE/RSJ International Conference on Intelligent Robots and Systems (IROS)*, pp. 6304–6311, IEEE, 2015.

[16] H.-W. Park, P. M. Wensing, S. Kim, *et al.*, "Online planning for autonomous running jumps over obstacles in high-speed quadrupeds," 2015.

[17] C. Gehring, S. Coros, M. Hutter, and R. Siegwart, "An optimization approach to controlling jump maneuvers for a quadrupedal robot," *Dyn. Walk*, 2015.

[18] G. Kenneally, A. De, and D. E. Koditschek, "Design principles for a family of direct-drive legged robots," *IEEE Robotics and Automation Letters*, vol. 1, no. 2, pp. 900–907, 2016.

[19] D. W. Haldane, M. M. Plecnik, J. K. Yim, and R. S. Fearing, "Robotic vertical jumping agility via series-elastic power modulation," *Science Robotics*, vol. 1, no. 1, p. eaag2048, 2016.

[20] P. Aerts, "Vertical jumping in galago senegalensis: the quest for an obligate mechanical power amplifier," *Philosophical Transactions of the Royal Society of London. Series B: Biological Sciences*, vol. 353, no. 1375, pp. 1607–1620, 1998.

[21] T. H. Harty, *The role of the vertebral column during jumping in quadrupedal mammals*. Oregon State University, 2010.

[22] H. C. Astley, E. Abbott, E. Azizi, R. Marsh, and T. Roberts, "Chasing maximal performance: a cautionary tale from the celebrated jumping frogs of calaveras county," *Journal of Experimental Biology*, vol. 216, no. 21, pp. 3947–3953, 2013.

[23] R. L. Marsh and H. B. John-Alder, "Jumping performance of hylid frogs measured with high-speed cine film.," *The Journal of experimental biology*, vol. 188, no. 1, pp. 131–141, 1994.

[24] R. Zufferey, A. O. Ancel, A. Farinha, R. Siddall, S. F. Armanini, M. Nasr, R. Brahmal, G. Kennedy, and M. Kovac, "Consecutive aquatic jump-gliding with water-reactive fuel," *Science Robotics*, vol. 4, no. 34, p. eaax7330, 2019.

[25] M. Kovač, O. Fauria, J.-C. Zufferey, D. Floreano, *et al.*, "The epfl jumpglider: A hybrid jumping and gliding robot with rigid or folding wings," in *2011 IEEE International Conference on Robotics and Biomimetics*, pp. 1503–1508, IEEE, 2011.

[26] J. Sun and C. Zhou, "Advancing robotic jumping with cvt enhanced sea," in *Annual Conference Towards Autonomous Robotic Systems*, pp. 73–84, Springer, 2024.

[27] J. Sun and C. Zhou, "Optimising aerodynamic drag for enhanced robotic balancing," *Engineering Applications of Computational Fluid Mechanics*, vol. 18, no. 1, p. 2430659, 2024.

[28] J. Sun and C. Zhou, "AeroTail: A bio-inspired aerodynamic tail mechanism for robotic balancing," in *The 28th International Conference on Automation and Computing*, pp. 436–441, 2023.

[29] Y. Wan, J. Sun, C. Peers, J. Humphreys, D. Kanoulas, and C. Zhou, "Performance and usability evaluation scheme for mobile manipulator teleoperation," *IEEE Transactions on Human-Machine Systems*, vol. 53, no. 5, pp. 844–854, 2023.

[30] J. Humphreys, C. Peers, J. Li, Y. Wan, J. Sun, R. Richardson, and C. Zhou, "Teleoperating a legged manipulator through whole-body control," in *Annual Conference Towards Autonomous Robotic Systems*, pp. 63–77, Springer, 2022.

[31] T. Wang, Y. Wan, C. Peers, J. Sun, and C. Zhou, "Vision-based gesture tracking for teleoperating mobile manipulators," in *UKRAS22 Conference "Robotics*

for Unconstrained Environments" Proceedings, pp. 52–53, EPSRC UK-Robotics and Autonomous Systems (UK-RAS) Network, 2022.

[32] C. Peers, J. Humphreys, Y. Wan, J. Li, J. Sun, R. Richardson, and C. Zhou, "Trigger-assisted ambidextrous control framework for teleoperation of two legged manipulators," in *Annual Conference Towards Autonomous Robotic Systems*, pp. 50–62, Springer, 2022.

[33] M. M. Plecnik, D. W. Haldane, J. K. Yim, and R. S. Fearing, "Design exploration and kinematic tuning of a power modulating jumping monopod," *Journal of Mechanisms and Robotics*, vol. 9, no. 1, p. 011009, 2017.

[34] A. Jusufi, D. I. Goldman, S. Revzen, and R. J. Full, "Active tails enhance arboreal acrobatics in geckos," *Proceedings of the National Academy of Sciences*, vol. 105, no. 11, pp. 4215–4219, 2008.

[35] M. J. van den Broek, *Fast Self-Stable Planar Bipedal Running*. PhD thesis, TU Delft, 2019.

[36] T. Apgar, P. Clary, K. Green, A. Fern, and J. W. Hurst, "Fast online trajectory optimization for the bipedal robot cassie.," in *Robotics: Science and Systems*, vol. 101, p. 14, 2018.

[37] A. M. Abate, "Mechanical design for robot locomotion," 2018.

[38] S. Sanchez and P. A. Bhounsule, "A differential drive rimless wheel that can move straight and turn," in *2020 IEEE/ASME International Conference on Advanced Intelligent Mechatronics (AIM)*, pp. 514–519, IEEE, 2020.

[39] J. B. Jeans and D. Hong, "Impass: Intelligent mobility platform with active spoke system," in *2009 IEEE International Conference on Robotics and Automation*, pp. 1605–1606, IEEE, 2009.

[40] N. Paine and L. Sentis, "A new prismatic series elastic actuator with compact size and high performance," in *2012 IEEE International Conference on Robotics and Biomimetics (ROBIO)*, pp. 1759–1766, IEEE, 2012.

[41] P. A. Bhounsule, E. Ameperosa, S. Miller, K. Seay, and R. Ulep, "Dead-beat control of walking for a torso-actuated rimless wheel using an event-based, discrete, linear controller," in *International Design Engineering Technical Conferences and Computers and Information in Engineering Conference*, vol. 50152, p. V05AT07A042, American Society of Mechanical Engineers, 2016.

[42] F. Asano and Z.-W. Luo, "Asymptotically stable biped gait generation based on stability principle of rimless wheel," *Robotica*, vol. 27, no. 6, pp. 949–958, 2009.

[43] F. Asano, "Stability principle underlying passive dynamic walking of rimless wheel," in *2012 IEEE International Conference on Control Applications*, pp. 1039–1044, IEEE, 2012.

[44] K. Wang, D. Marsh, R. P. Saputra, D. Chappell, Z. Jiang, A. Raut, B. Kon, and P. Kormushev, "Design and control of slider: an ultra-lightweight, knee-less, low-cost bipedal walking robot," in *2020 IEEE/RSJ International Conference on Intelligent Robots and Systems (IROS)*, pp. 3488–3495, IEEE, 2020.

[45] K. Wang, H. Fei, and P. Kormushev, "Fast online optimization for terrain-blind bipedal robot walking with a decoupled actuated slip model," *Frontiers in Robotics and AI*, vol. 9, 2022.

[46] M. H. Raibert, H. B. Brown Jr, and M. Chepponis, "Experiments in balance with a 3d one-legged hopping machine," *The International Journal of Robotics Research*, vol. 3, no. 2, pp. 75–92, 1984.

[47] H. Rad, P. Gregorio, and M. Buehler, "Design, modeling and control of a hopping robot," in *Proceedings of 1993 IEEE/RSJ International Conference on Intelligent Robots and Systems (IROS'93)*, vol. 3, pp. 1778–1785, IEEE, 1993.

[48] T. E. Wei, G. M. Nelson, R. D. Quinn, H. Verma, and S. L. Garverick, "Design of a 5-cm monopod hopping robot," in *Proceedings 2000 ICRA. Millennium Conference. IEEE International Conference on Robotics and Automation. Symposia Proceedings (Cat. No. 00CH37065)*, vol. 3, pp. 2828–2833, IEEE, 2000.

[49] D. W. Haldane, M. Plecnik, J. K. Yim, and R. S. Fearing, "A power modulating leg mechanism for monopedal hopping," in *2016 IEEE/RSJ International Conference on Intelligent Robots and Systems (IROS)*, pp. 4757–4764, IEEE, 2016.

[50] M. M. Plecnik and J. M. McCarthy, "Design of stephenson linkages that guide a point along a specified trajectory," *Mechanism and Machine Theory*, vol. 96, pp. 38–51, 2016.

[51] M. M. Plecnik and J. Michael McCarthy, "Computational design of stephenson ii six-bar function generators for 11 accuracy points," *Journal of Mechanisms and Robotics*, vol. 8, no. 1, 2016.

[52] M. M. Plecnik and J. M. McCarthy, "Kinematic synthesis of stephenson iii six-bar function generators," *Mechanism and Machine Theory*, vol. 97, pp. 112–126, 2016.

[53] K.-L. Ting and X. Dou, "Classification and branch identification of stephenson six-bar chains," *Mechanism and Machine Theory*, vol. 31, no. 3, pp. 283–295, 1996.

[54] C. Knabe, B. Lee, and D. Hong, "An inverted straight line mechanism for augmenting joint range of motion in a humanoid robot," in *International Design Engineering Technical Conferences and Computers and Information in Engineering Conference*, vol. 46377, p. V05BT08A015, American Society of Mechanical Engineers, 2014.

[55] B. Lee, C. Knabe, V. Orekhov, and D. Hong, "Design of a human-like range of motion hip joint for humanoid robots," in *International Design Engineering Technical Conferences and Computers and Information in Engineering Conference*, vol. 46377, p. V05BT08A018, American Society of Mechanical Engineers, 2014.

[56] S. Lu, D. Zlatanov, X. Ding, and R. Molfino, "A new family of deployable mechanisms based on the hoekens linkage," *Mechanism and Machine Theory*, vol. 73, pp. 130–153, 2014.

[57] A. Rodriguez and M. T. Mason, "Effector form design for 1dof planar actuation," in *2013 IEEE International Conference on Robotics and Automation*, pp. 349–356, IEEE, 2013.

[58] V. Orekhov, D. Lahr, B. Lee, and D. Hong, "Configurable compliance for series elastic actuators," in *International Design Engineering Technical Conferences and Computers and Information in Engineering Conference*, vol. 55942, p. V06BT07A021, American Society of Mechanical Engineers, 2013.

[59] D. F. Lahr, H. Yi, and D. W. Hong, "Biologically inspired design of a parallel actuated humanoid robot," *Advanced Robotics*, vol. 30, no. 2, pp. 109–118, 2016.

[60] M. Grimmer, M. Eslamy, S. Gliech, and A. Seyfarth, "A comparison of parallel- and series elastic elements in an actuator for mimicking human ankle joint in walking and running," in *IEEE International Conference on Robotics and Automation*, pp. 2463–2470, 2012.

[61] W. Roozing, Z. Ren, and N. G. Tsagarakis, "An efficient leg with series–parallel and biarticular compliant actuation: design optimization, modeling, and control

of the eleg," *The International Journal of Robotics Research*, vol. 40, no. 1, pp. 37–54, 2021.

[62] W. Roozing, Z. Ren, and N. G. Tsagarakis, "Design of a novel 3-dof leg with series and parallel compliant actuation for energy efficient articulated robots," in *2018 IEEE International Conference on Robotics and Automation (ICRA)*, pp. 6068–6075, IEEE, 2018.

[63] F. Li, W. Liu, X. Fu, G. Bonsignori, U. Scarfogliero, C. Stefanini, and P. Dario, "Jumping like an insect: Design and dynamic optimization of a jumping mini robot based on bio-mimetic inspiration," *Mechatronics*, vol. 22, no. 2, pp. 167–176, 2012.

[64] M. Noh, S.-W. Kim, S. An, J.-S. Koh, and K.-J. Cho, "Flea-inspired catapult mechanism for miniature jumping robots," *IEEE transactions on robotics*, vol. 28, no. 5, pp. 1007–1018, 2012.

[65] A. Degani, A. W. Long, S. Feng, H. B. Brown, R. D. Gregg, H. Choset, M. T. Mason, and K. M. Lynch, "Design and open-loop control of the parkourbot, a dynamic climbing robot," *IEEE Transactions on Robotics*, vol. 30, no. 3, pp. 705–718, 2014.

[66] E. W. Hawkes, C. Xiao, R.-A. Peloquin, C. Keeley, M. R. Begley, M. T. Pope, and G. Niemeyer, "Engineered jumpers overcome biological limits via work multiplication," *Nature*, vol. 604, no. 7907, pp. 657–661, 2022.

[67] H. Wang, Y. Luan, D. Oetomo, and Z. Wang, "Design, analysis and experimental evaluation of a gas-fuel-powered actuator for robotic hoppers," *IEEE/ASME Transactions on Mechatronics*, vol. 20, no. 5, pp. 2264–2275, 2014.

[68] N. Csomay-Shanklin, V. D. Dorobantu, and A. D. Ames, "Nonlinear model predictive control of a 3D hopping robot: Leveraging lie group integrators for dynamically stable behaviors," in *IEEE International Conference on Robotics and Automation*, pp. 12106–12112, 2023.

[69] W. D. Shin, W. Stewart, M. A. Estrada, A. J. Ijspeert, and D. Floreano, "Elastic-actuation mechanism for repetitive hopping based on power modulation and cyclic trajectory generation," *IEEE Transactions on Robotics*, vol. 39, no. 1, pp. 558–571, 2022.

[70] P. Beckerle, T. Verstraten, G. Mathijssen, R. Furnémont, B. Vanderborght, and D. Lefeber, "Series and parallel elastic actuation: Influence of operating

positions on design and control," *IEEE/ASME Transactions on Mechatronics*, vol. 22, no. 1, pp. 521–529, 2016.

[71] J. Kim, F. C. Park, and Y. Park, "Design, analysis and control of a wheeled mobile robot with a nonholonomic spherical CVT," *The International Journal of Robotics Research*, vol. 21, no. 5-6, pp. 409–426, 2002.

[72] A. S. Kernbaum, M. Kitchell, and M. Crittenden, "An ultra-compact infinitely variable transmission for robotics," in *IEEE International Conference on Robotics and Automation*, pp. 1800–1807, 2017.

[73] K. Matsushita, S. Shikanai, and H. Yokoi, "Development of Drum CVT for a wire-driven robot hand," in *IEEE/RSJ International Conference on Intelligent Robots and Systems*, pp. 2251–2256, 2009.

[74] A. A. Nobaveh, J. L. Herder, and G. Radaelli, "A compliant continuously variable transmission (cvt)," *Mechanism and Machine Theory*, vol. 184, p. 105281, 2023.

[75] L. Mooney and H. Herr, "Continuously-variable series-elastic actuator," in *IEEE International Conference on Rehabilitation Robotics*, pp. 1–6, 2013.

[76] D. Carré and P. Bertrand, "Analysis of hubble space telescope reaction wheel lubricant," *Journal of Spacecraft and Rockets*, vol. 36, no. 1, pp. 109–113, 1999.

[77] Z. Ismail and R. Varatharajoo, "A study of reaction wheel configurations for a 3-axis satellite attitude control," *Advances in Space Research*, vol. 45, no. 6, pp. 750–759, 2010.

[78] W. Bialke and E. Hansell, "A newly discovered branch of the fault tree explaining systemic reaction wheel failures and anomalies," in *European Space Mechanisms and Tribology Symposium*, pp. 20–22, 2017.

[79] J. Jin, S. Ko, and C.-K. Ryoo, "Fault tolerant control for satellites with four reaction wheels," *Control Engineering Practice*, vol. 16, no. 10, pp. 1250–1258, 2008.

[80] J. Meyer, N. Delson, and R. A. de Callafon, "Design, modeling and stabilization of a moment exchange based inverted pendulum," *International Federation of Automatic Control*, vol. 42, no. 10, pp. 462–467, 2009.

[81] M. Bartuccelli, G. Gentile, and K. Georgiou, "On the stability of the upside–down pendulum with damping," *The Royal Society of London. Series A: Mathematical, Physical and Engineering Sciences*, vol. 458, no. 2018, pp. 255–269, 2002.

[82] P. Reist and R. Tedrake, "Simulation-based lqr-trees with input and state constraints," in *IEEE International Conference on Robotics and Automation*, pp. 5504–5510, 2010.

[83] R. Featherstone, "A simple model of balancing in the plane and a simple preview balance controller," *The International Journal of Robotics Research*, vol. 36, no. 13-14, pp. 1489–1507, 2017.

[84] M. Hofer, M. Muehlebach, and R. D'Andrea, "The one-wheel cubli: A 3d inverted pendulum that can balance with a single reaction wheel," *Mechatronics*, vol. 91, p. 102965, 2023.

[85] D. W. Haldane, J. K. Yim, and R. S. Fearing, "Repetitive extreme-acceleration (14-g) spatial jumping with salto-1p," in *IEEE/RSJ International Conference on Intelligent Robots and Systems*, pp. 3345–3351, 2017.

[86] K. Kim, P. Spieler, E.-S. Lupu, A. Ramezani, and S.-J. Chung, "A bipedal walking robot that can fly, slackline, and skateboard," *Science Robotics*, vol. 6, no. 59, p. eabf8136, 2021.

[87] C. Huang, Y. Liu, K. Wang, and B. Bai, "Land–air–wall cross-domain robot based on gecko landing bionic behavior: System design, modeling, and experiment," *Applied Sciences*, vol. 12, no. 8, p. 3988, 2022.

[88] S. Shield, R. Jericevich, A. Patel, and A. Jusufi, "Tails, flails, and sails: How appendages improve terrestrial maneuverability by improving stability," *Integrative and Comparative Biology*, vol. 61, no. 2, pp. 506–520, 2021.

[89] J. W. Young, B. A. Chadwell, N. T. Dunham, A. McNamara, T. Phelps, T. Hieronymus, and L. J. Shapiro, "The stabilizing function of the tail during arboreal quadrupedalism," *Integrative and Comparative Biology*, vol. 61, no. 2, pp. 491–505, 2021.

[90] M. Schwaner, S. Hsieh, I. Braasch, S. Bradley, C. Campos, C. Collins, C. M. Donatelli, F. Fish, O. Fitch, B. Flammang, *et al.*, "Future tail tales: A forward-looking, integrative perspective on tail research," *Integrative and Comparative Biology*, vol. 61, no. 2, pp. 521–537, 2021.

[91] R. Briggs, J. Lee, M. Haberland, and S. Kim, "Tails in biomimetic design: Analysis, simulation, and experiment," in *IEEE/RSJ International Conference on Intelligent Robots and Systems*, pp. 1473–1480, 2012.

[92] R. Siddall, V. Ibanez, G. Byrnes, R. J. Full, and A. Jusufi, "Mechanisms for mid-air reorientation using tail rotation in gliding geckos," *Integrative and Comparative Biology*, vol. 61, no. 2, pp. 478–490, 2021.

[93] A. Patel, E. Boje, C. Fisher, L. Louis, and E. Lane, "Quasi-steady state aerodynamics of the cheetah tail," *Biology Open*, vol. 5, no. 8, pp. 1072–1076, 2016.

[94] C. Fisher, "State estimation of a cheetah spine and tail using an inertial sensor network," Master's thesis, University of Cape Town, 2015.

[95] T. Fukushima, R. Siddall, F. Schwab, S. L. Toussaint, G. Byrnes, J. A. Nyakatura, and A. Jusufi, "Inertial tail effects during righting of squirrels in unexpected falls: from behavior to robotics," *Integrative and Comparative Biology*, vol. 61, no. 2, pp. 589–602, 2021.

[96] S. F. Hoerner, "Practical information on aerodynamic drag and hydrodynamic resistance," *Fluid dynamic drag. Horner fluid dynamics, CA*, 1965.

[97] J. Norby, J. Y. Li, C. Selby, A. Patel, and A. M. Johnson, "Enabling dynamic behaviors with aerodynamic drag in lightweight tails," *IEEE Transactions on Robotics*, vol. 37, no. 4, pp. 1144–1153, 2021.

[98] E.-S. Aziz, C. Chassapis, S. Esche, S. Dai, S. Xu, and R. Jia, "Online wind tunnel laboratory," in *Annual Conference & Exposition*, pp. 13–949, 2008.

[99] A. Roostaee and M. Vaezi, "Developing a standard platform to predict the drag coefficient of irregular shape particles," *Powder Technology*, vol. 395, pp. 314–337, 2022.

[100] B. Abolpour, R. Hekmatkhah, and R. Shamsoddini, "A novel approach for obtaining optimum shape design with the minimum drag coefficient," *Structural and Multidisciplinary Optimization*, vol. 65, no. 11, p. 306, 2022.

[101] E. E. Michaelides and Z. Feng, "Drag coefficients of non-spherical and irregularly shaped particles," *Journal of Fluids Engineering*, vol. 145, no. 6, p. 060801, 2023.

[102] R. Blickhan, "The spring-mass model for running and hopping," *Journal of biomechanics*, vol. 22, no. 11-12, pp. 1217–1227, 1989.

[103] H. Geyer, A. Seyfarth, and R. Blickhan, "Compliant leg behaviour explains basic dynamics of walking and running," *Proceedings of the Royal Society B: Biological Sciences*, vol. 273, no. 1603, pp. 2861–2867, 2006.

[104] W. J. Schwind and D. E. Koditschek, "Control of forward velocity for a simplified planar hopping robot," in *Proceedings of 1995 IEEE International Conference on Robotics and Automation*, vol. 1, pp. 691–696, IEEE, 1995.

[105] I. Poulakakis and J. W. Grizzle, "Formal embedding of the spring loaded inverted pendulum in an asymmetric hopper," in *2007 European Control Conference (ECC)*, pp. 3159–3166, IEEE, 2007.

[106] I. Poulakakis and J. W. Grizzle, "The spring loaded inverted pendulum as the hybrid zero dynamics of an asymmetric hopper," *IEEE Transactions on Automatic Control*, vol. 54, no. 8, pp. 1779–1793, 2009.

[107] J. K. Yim and R. S. Fearing, "Precision jumping limits from flight-phase control in salto-1p," in *2018 IEEE/RSJ international conference on intelligent robots and systems (IROS)*, pp. 2229–2236, IEEE, 2018.

[108] S. M. Hoseinifard and M. Sadedel, "Standing balance of single-legged hopping robot model using reinforcement learning approach in the presence of external disturbances," *Scientific Reports*, vol. 14, no. 1, p. 32036, 2024.

[109] X. Xiong and A. D. Ames, "Sequential motion planning for bipedal somersault via flywheel slip and momentum transmission with task space control," in *2020 IEEE/RSJ International Conference on Intelligent Robots and Systems (IROS)*, pp. 3510–3517, IEEE, 2020.

[110] H. Hamzaçebi and Ö. Morgül, "Enlarging the region of stability using the torque-enhanced active slip model," in *2015 International Conference on Advanced Robotics (ICAR)*, pp. 345–350, IEEE, 2015.

[111] B. Bokser and Z. Manchester, "Rex hopper: Design and control of a monopod hopper with reaction wheels,"

[112] E. R. Ambrose, *Creating ARCHER: A 3D hopping robot with flywheels for attitude control*. California Institute of Technology, 2022.

[113] Z. Shen and J. Seipel, "A piecewise-linear approximation of the canonical spring-loaded inverted pendulum model of legged locomotion," *Journal of Computational and Nonlinear Dynamics*, vol. 11, no. 1, 2016.

[114] A. U. Kilic and D. J. Braun, "A novel approximation for the spring loaded inverted pendulum model of locomotion," in *2023 IEEE/RSJ International Conference on Intelligent Robots and Systems (IROS)*, pp. 4315–4321, IEEE, 2023.

[115] B. Han, H. Yi, Z. Xu, X. Yang, and X. Luo, "3d-slip model based dynamic stability strategy for legged robots with impact disturbance rejection," *Scientific Reports*, vol. 12, no. 1, p. 5892, 2022.

[116] W.-C. Lu and P.-C. Lin, "The generalized spring-loaded inverted pendulum model for analysis of various planar reduced-order models and for optimal robot leg design," *Bioinspiration & Biomimetics*, vol. 19, no. 2, p. 026017, 2024.

[117] H. Chen, B. Wang, Z. Hong, C. Shen, P. M. Wensing, and W. Zhang, "Underactuated motion planning and control for jumping with wheeled-bipedal robots," *IEEE Robotics and Automation Letters*, vol. 6, no. 2, pp. 747–754, 2020.

[118] F. M. White, *Fluid mechanics*. 1966.

[119] B. R. Munson, D. F. Young, and T. H. Okiishi, "Fundamentals of fluid mechanics," *Oceanographic Literature Review*, vol. 10, no. 42, p. 831, 1995.

[120] M. G. Mohammed, A. F. Messerman, B. D. Mayhan, and K. M. Trauth, "Theory and practice of the hydrodynamic redesign of artificial hellbender habitat," *Herpetological Review*, vol. 47, no. 4, pp. 586–591, 2016.

[121] B. Ponitz, M. Triep, and C. Brücker, "Aerodynamics of the cupped wings during peregrine falcon's diving flight," *Open Journal of Fluid Dynamics*, vol. 4, no. 4, 2014.

[122] S. Khosravi and D. W. Zingg, "Aerostructural perspective on winglets," *Journal of Aircraft*, vol. 54, no. 3, pp. 1121–1138, 2017.

[123] A. Amini, M. Reclari, T. Sano, M. Iino, and M. Farhat, "Suppressing tip vortex cavitation by winglets," *Experiments in Fluids*, vol. 60, pp. 1–15, 2019.

[124] X.-b. Lai, H.-s. Wang, and H.-s. Liu, "Research on duct flow field optimisation of a robot vacuum cleaner," *International Journal of Advanced Robotic Systems*, vol. 8, no. 5, p. 65, 2011.

[125] Z. Guodong, G. Peiyuan, and M. Lili, "The kinematics modeling and parameter optimization of six-wheel lunar exploration robot," *International Journal of Advanced Robotic Systems*, vol. 15, no. 3, p. 1729881418770005, 2018.

[126] J. Zhao, J. Xu, B. Gao, N. Xi, F. J. Cintron, M. W. Mutka, and L. Xiao, "Msu jumper: A single-motor-actuated miniature steerable jumping robot," *IEEE Transactions on Robotics*, vol. 29, no. 3, pp. 602–614, 2013.

[127] J. Pentzer and S. Brennan, "Investigation of the effect of continuously variable transmissions on ground robot powertrain efficiency," in *American Control Conference*, pp. 4245–4250, 2012.

[128] F. Benitez, J. Madrigal, and J. Del Castillo, "Infinitely variable transmission of racheting drive type based on one-way clutches," *Journal of Mechanical Design*, vol. 126, no. 4, pp. 673–682, 2004.

[129] O. Arslan, U. Saranli, and O. Morgul, "An approximate stance map of the spring mass hopper with gravity correction for nonsymmetric locomotions," in *2009 IEEE International Conference on Robotics and Automation*, pp. 2388–2393, IEEE, 2009.

Appendix A

Supplementary figures

A.1 The mechanical design of the jumper prototype: detailed figures

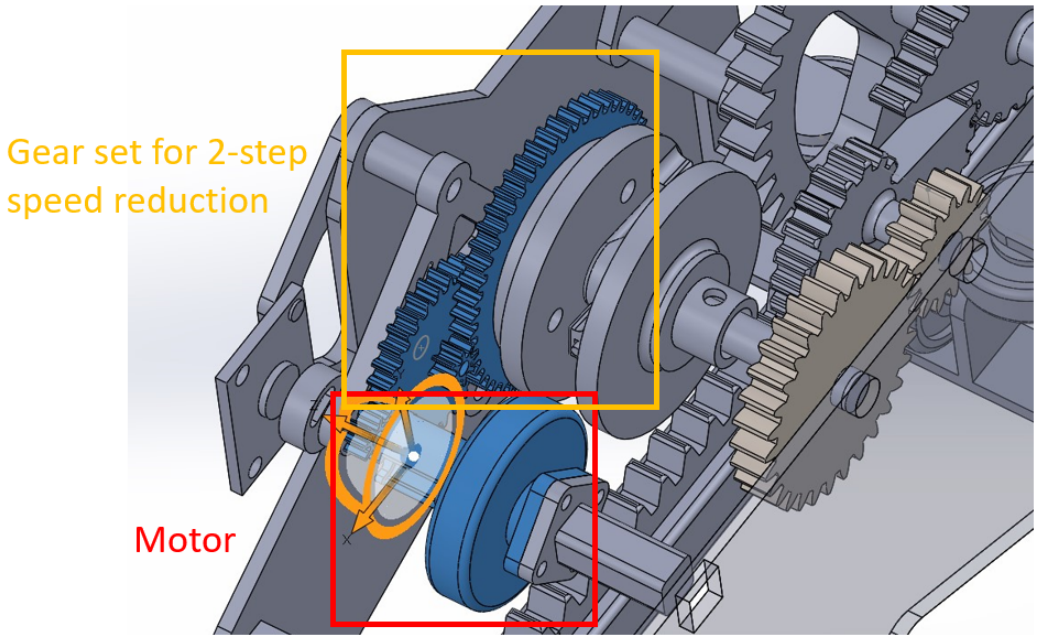

Figure A.1: The motor and the reduction gearbox.

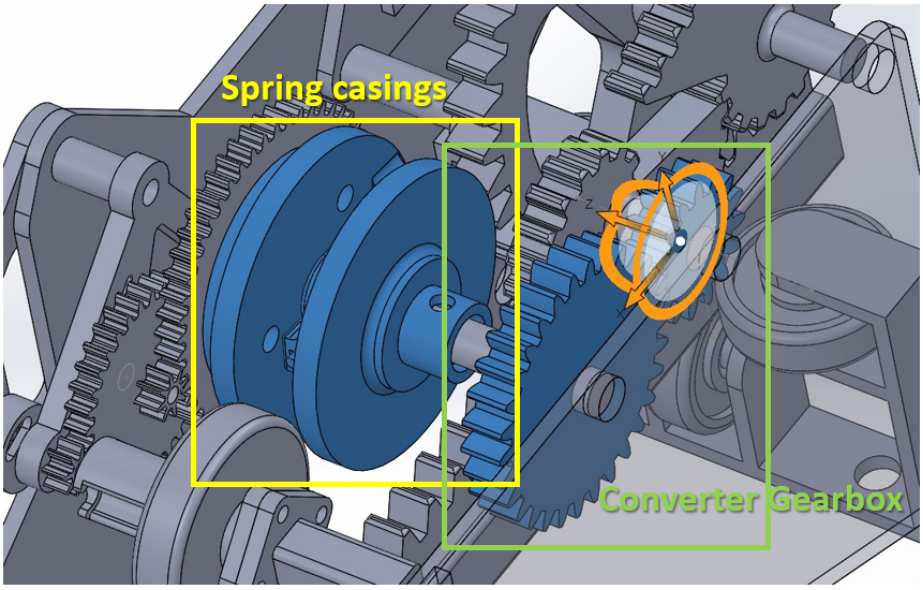

Figure A.2: The spring casing (spring not shown) and the converter gearbox transmitting torque and rotation between the spring and the CVT gearset.

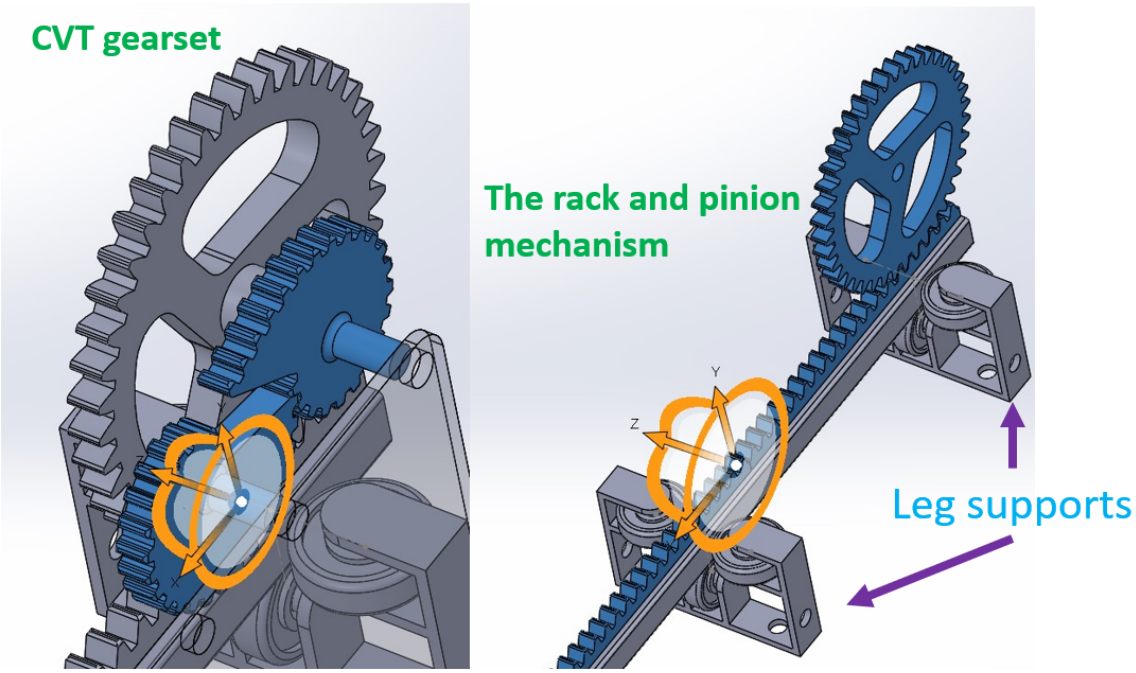

Figure A.3: The CVT gearset and the rack-and-pinion mechanism. Rack is fixed on the leg.

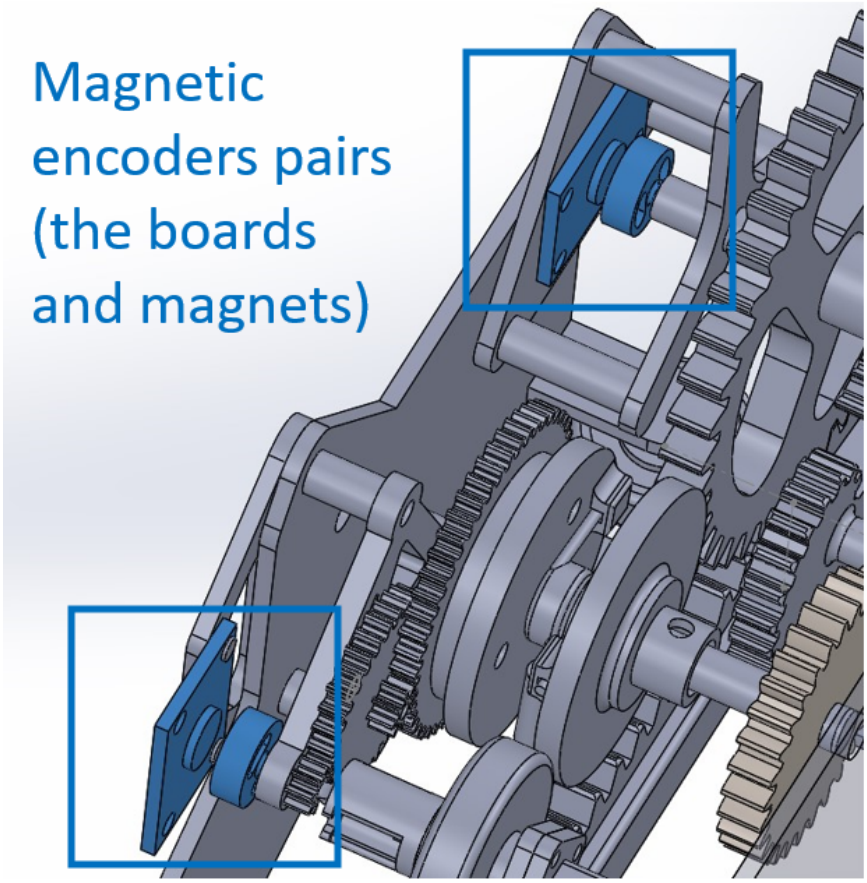

Figure A.4: The mounting positions for the magnetic encoders. They are used to measure the rotation angle and velocity of the motor and the pinion.

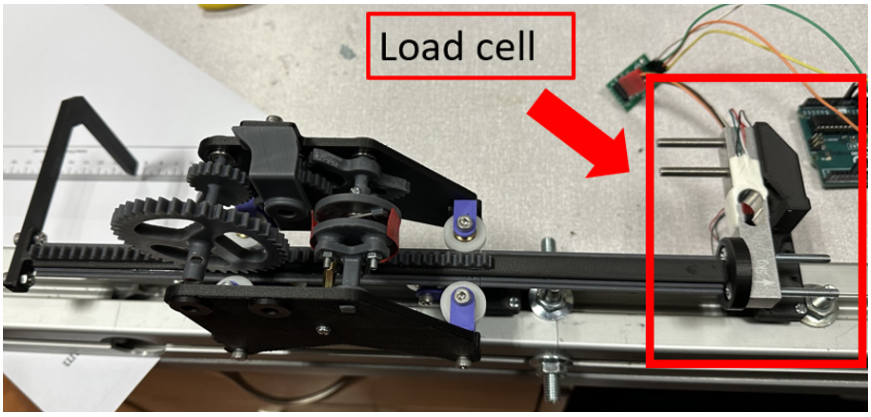

Figure A.5: The Ver.1 jumper undergoing a force testing using a load cell. A simple printer ruler is being used for to measure the distance.

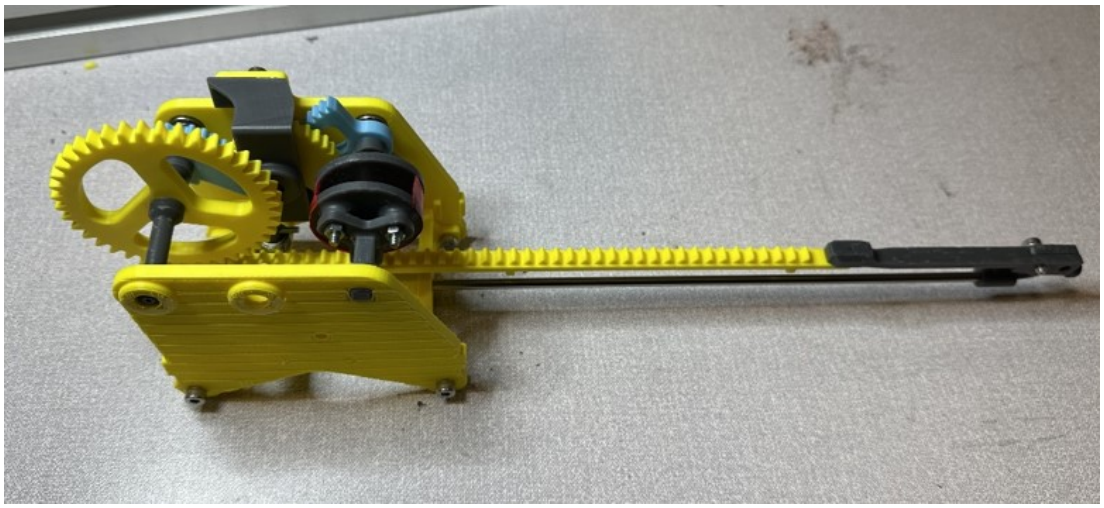

Figure A.6: The Ver.2 of the jumper prototype

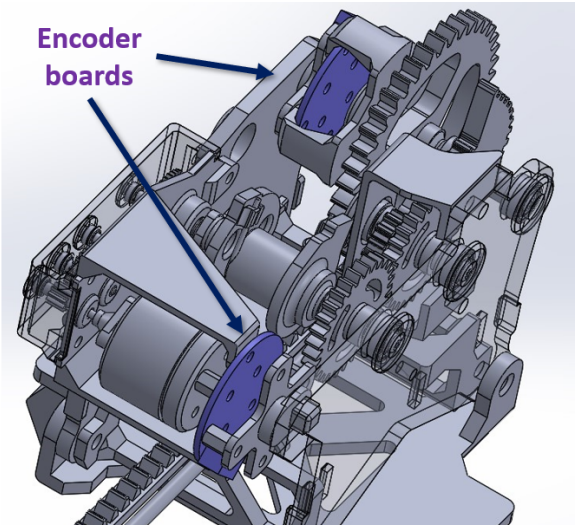

Figure A.7: The positions of the encoder boards. The magnets (not shown) are connected to the shafts of motor and pinion.

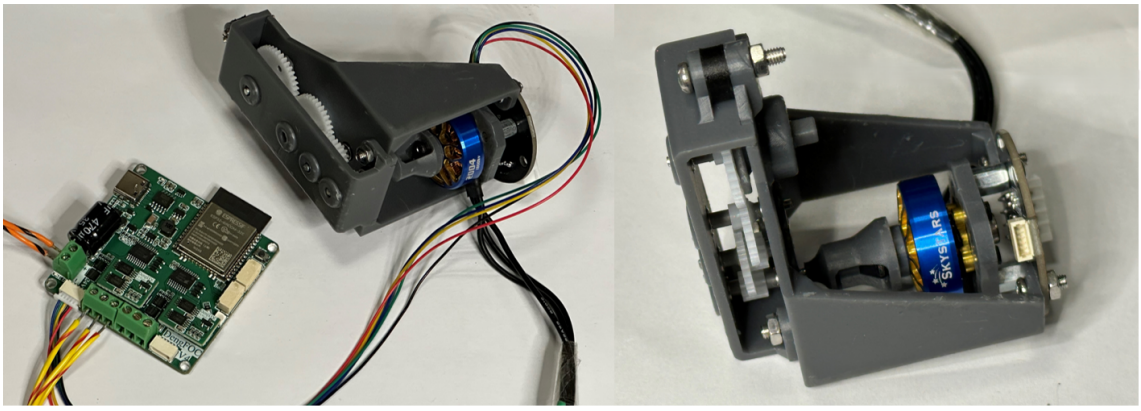

Figure A.8: The manufactured reduction gearbox-motor module. The picture on the left is the gearbox module with the motor drive board and the right one is the module by itself.

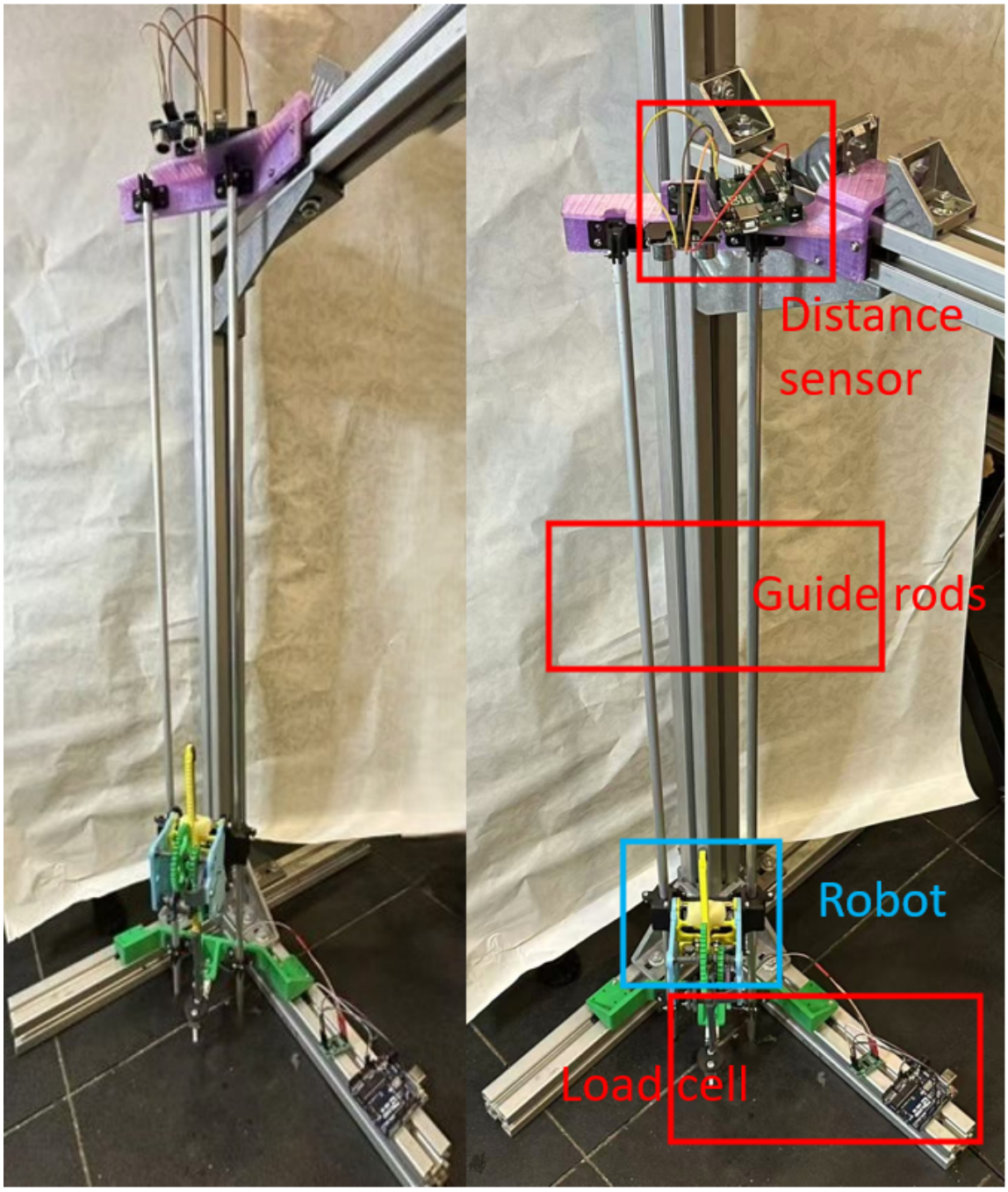

Figure A.9: The experiment platform has an overall structure shown in the figure.

A.2 Full Robot Simulation additional figures

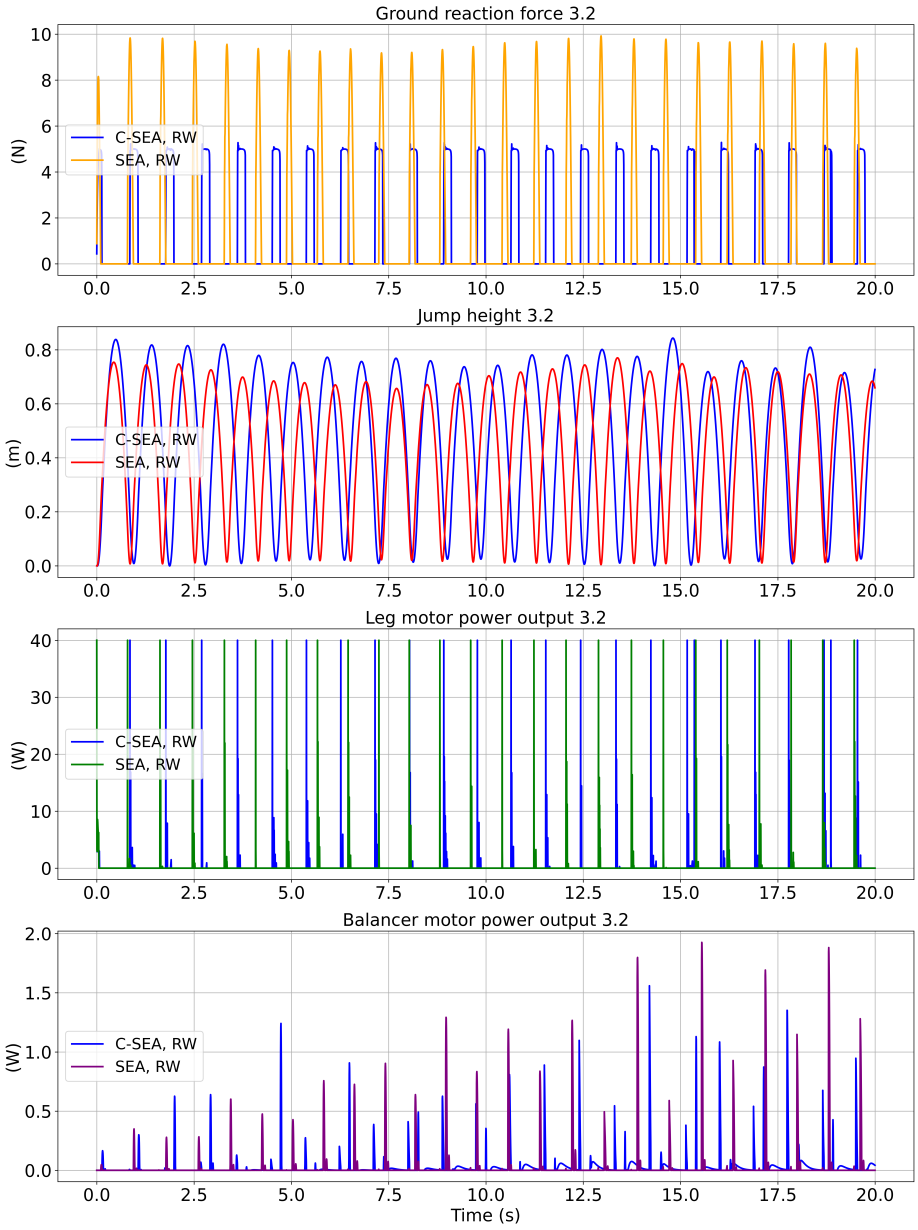

Figure A.10: The ground reaction forces, jump heights, leg motor and balancer motor power outputs are compared in this figure between Robot-A and Robot-B. Note that Robot-A is with C-SEA and RW and Robot-B is with SEA and RW.

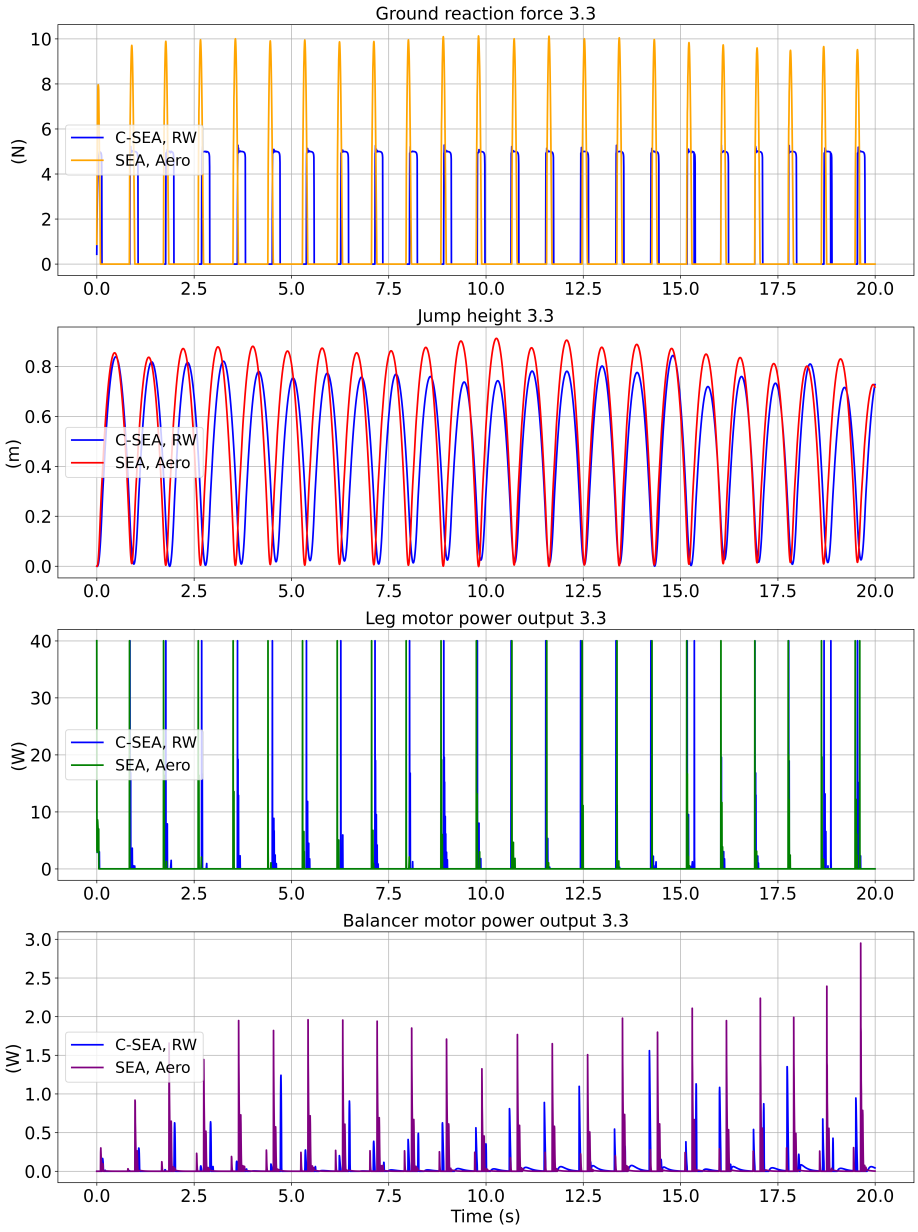

Figure A.11: The ground reaction forces, jump heights, leg motor and balancer motor power outputs are compared in this figure between Robot-A and Robot-B. Note that Robot-A is with C-SEA and RW and Robot-B is with SEA and AeroTail.

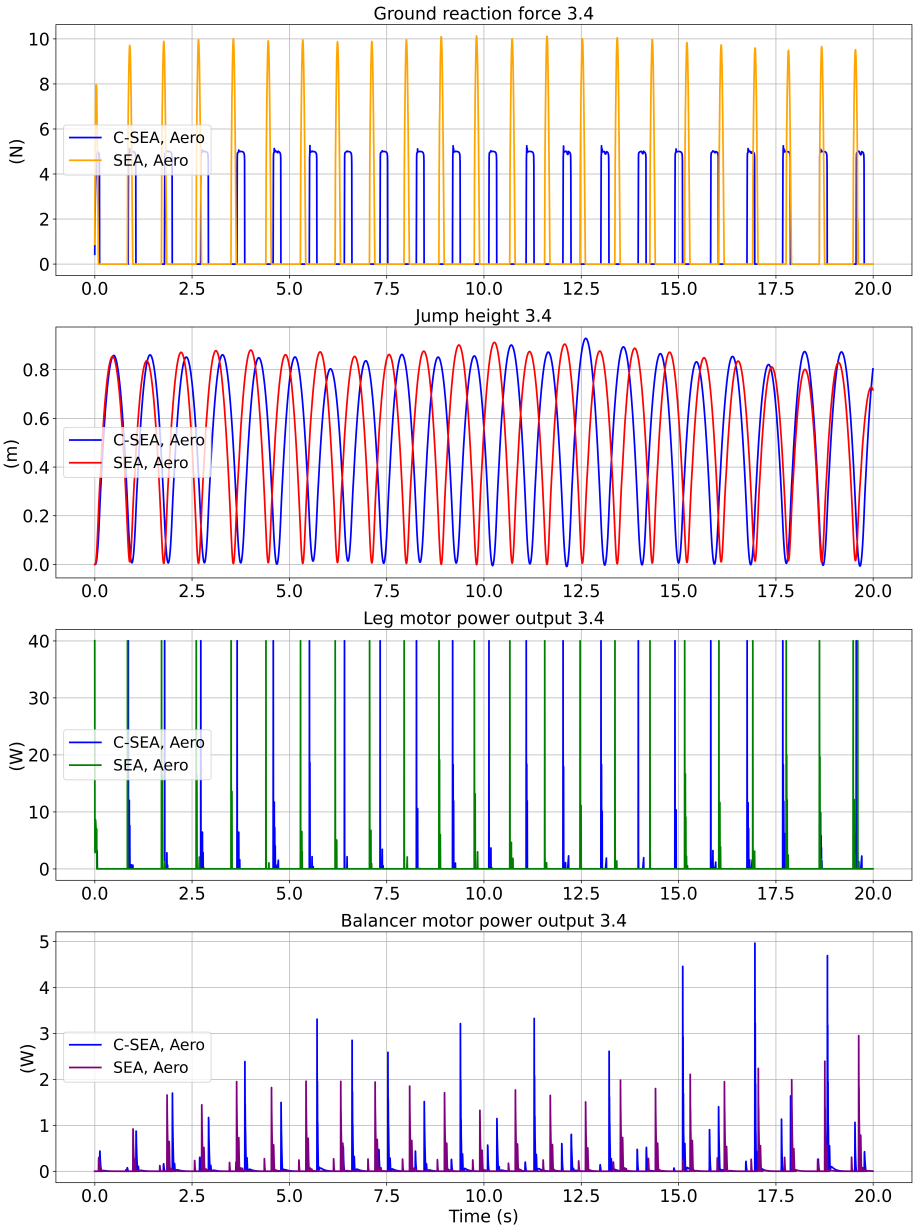

Figure A.12: The ground reaction forces, jump heights, leg motor and balancer motor power outputs are compared in this figure between Robot-A and Robot-B. Note that Robot-A is with C-SEA and AeroTail and Robot-B is with SEA and AeroTail.

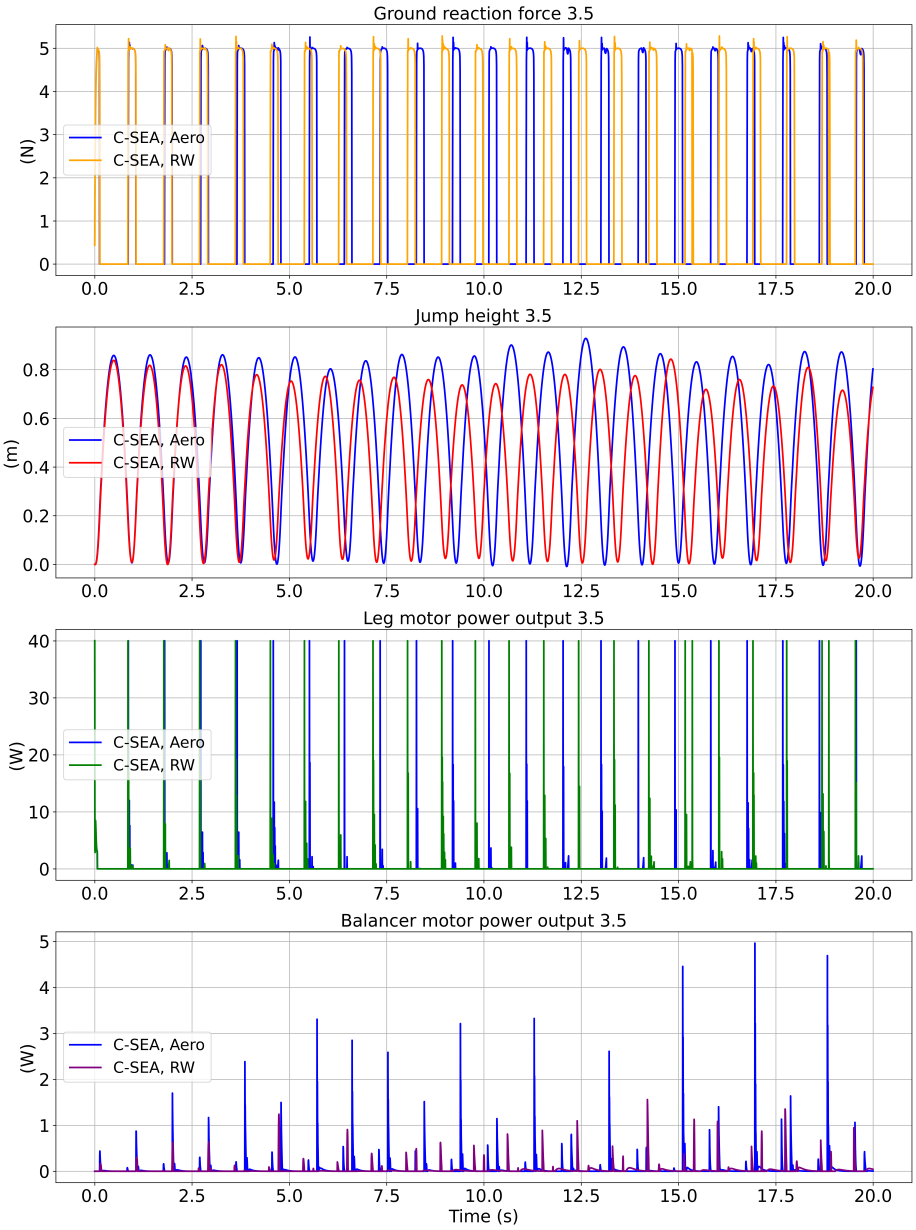

Figure A.13: The ground reaction forces, jump heights, leg motor and balancer motor power outputs are compared in this figure between Robot-A and Robot-B. Note that Robot-A is with C-SEA and AeroTail and Robot-B is with C-SEA and RW.

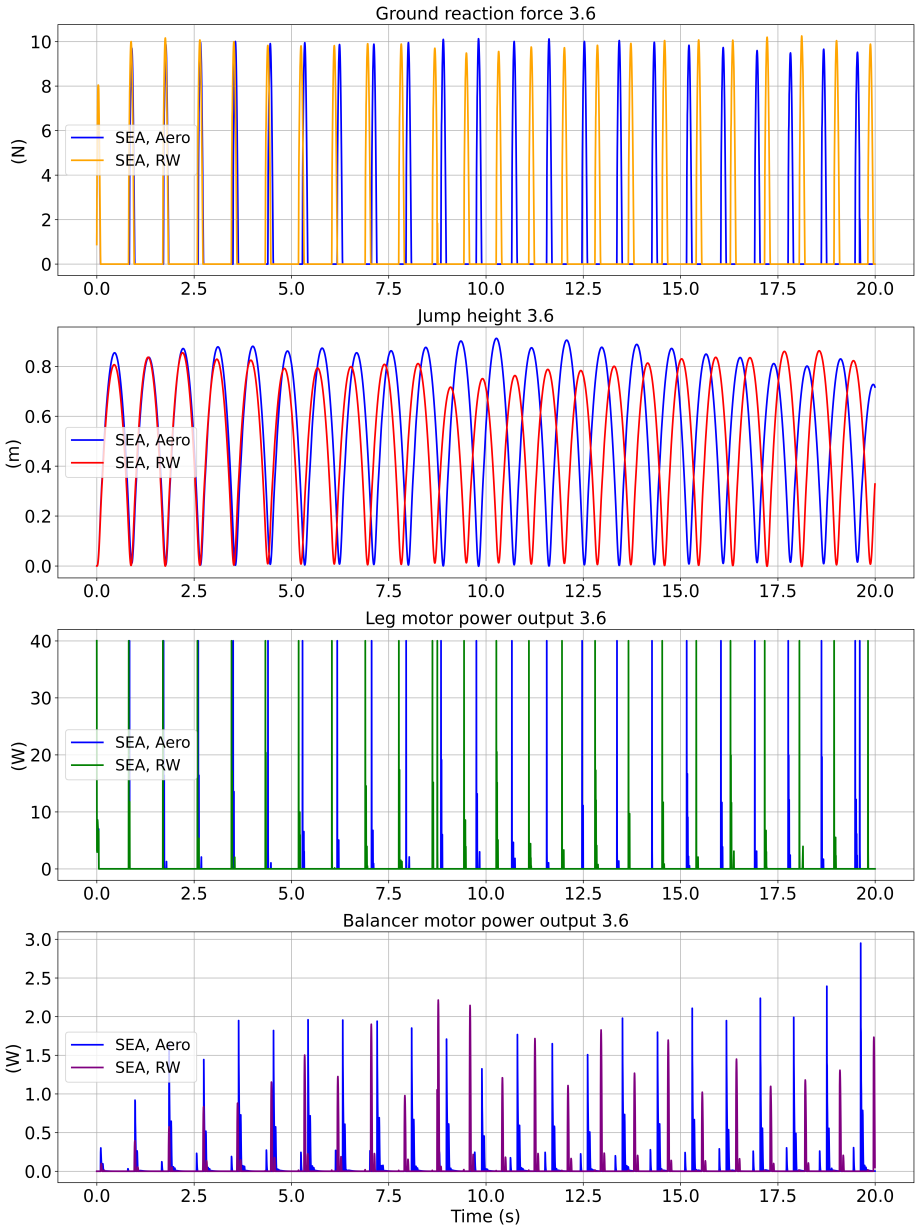

Figure A.14: The ground reaction forces, jump heights, leg motor and balancer motor power outputs are compared in this figure between Robot-A and Robot-B. Note that Robot-A is with SEA and AeroTail and Robot-B is with SEA and RW.